**Springer Theses**
Recognizing Outstanding Ph.D. Research

Lin Li

# Manipulation of Near Field Propagation and Far Field Radiation of Surface Plasmon Polariton

Springer

## Springer Theses

Recognizing Outstanding Ph.D. Research

## Aims and Scope

The series "Springer Theses" brings together a selection of the very best Ph.D. theses from around the world and across the physical sciences. Nominated and endorsed by two recognized specialists, each published volume has been selected for its scientific excellence and the high impact of its contents for the pertinent field of research. For greater accessibility to non-specialists, the published versions include an extended introduction, as well as a foreword by the student's supervisor explaining the special relevance of the work for the field. As a whole, the series will provide a valuable resource both for newcomers to the research fields described, and for other scientists seeking detailed background information on special questions. Finally, it provides an accredited documentation of the valuable contributions made by today's younger generation of scientists.

## Theses are accepted into the series by invited nomination only and must fulfill all of the following criteria

- They must be written in good English.
- The topic should fall within the confines of Chemistry, Physics, Earth Sciences, Engineering and related interdisciplinary fields such as Materials, Nanoscience, Chemical Engineering, Complex Systems and Biophysics.
- The work reported in the thesis must represent a significant scientific advance.
- If the thesis includes previously published material, permission to reproduce this must be gained from the respective copyright holder.
- They must have been examined and passed during the 12 months prior to nomination.
- Each thesis should include a foreword by the supervisor outlining the significance of its content.
- The theses should have a clearly defined structure including an introduction accessible to scientists not expert in that particular field.

More information about this series at http://www.springer.com/series/8790

Lin Li

# Manipulation of Near Field Propagation and Far Field Radiation of Surface Plasmon Polariton

Doctoral thesis accepted by
Nanjing University, Nanjing, China

Springer

*Author*
Dr. Lin Li
School of Physics
Nanjing University
Nanjing
China

*Supervisors*
Prof. Shining Zhu
National Laboratory of Solid State Microstructures, College of Engineering and Applied Sciences, School of Physics
Nanjing University
Nanjing
China

Prof. Tao Li
National Laboratory of Solid State Microstructures, College of Engineering and Applied Sciences, School of Physics
Nanjing University
Nanjing
China

ISSN 2190-5053 ISSN 2190-5061 (electronic)
Springer Theses
ISBN 978-981-10-4662-9 ISBN 978-981-10-4663-6 (eBook)
DOI 10.1007/978-981-10-4663-6

Library of Congress Control Number: 2017939095



Printed on acid-free paper

This Springer imprint is published by Springer Nature
The registered company is Springer Nature Singapore Pte Ltd.
The registered company address is: 152 Beach Road, #21-01/04 Gateway East, Singapore 189721, Singapore

# Supervisor's Foreword

I am very pleased to introduce this Ph.D. Thesis by Dr. Lin Li, who was a graduate student under the supervision of Prof. Shining Zhu and me, and completed his Ph.D. in May 2014. His research topic is to study the surface plasmon polariton (SPP) manipulations on the near-field beam engineering and far-field radiation.

Being in a rapid progress in this nanotech era, optics has stepped into the micro/nano regime. Plasmonics is an important direction in nano-photonics, attributing to the special electromagnetic mode on a metal surface with squeezed optical wavelength and enhanced field intensity. Lin successfully developed a new strategy to manipulate the SPP propagations (wave-front, beam shape, intensity, etc.) totally in a planar dimension of metal surface. It is so-called "non-perfectly matched Bragg diffraction", which is partially borrowed from the Bragg reflection for a general wave. Based on this new method, he performed detailed micro/nano sample designs and fabrications, set up optical settings, carried out the leakage radiation microscopy investigations, and successfully realized a series of interesting plasmonic beams experimentally, such as nondiffracting Airy beams, self-collimated beams, broadband focusing beams. I credit the major contribution of Dr. Lin Li in these significant works, which surely enhances the people's capability in steering the SPP near field.

Nevertheless, Lin further extended the method to manipulate the SPP far-field radiations. By designing proper scattering nanostructures on a metal surface, the in-plane propagating SPPs will be scattered out-of-plane with a preferred form in beam shape and polarization. As examples, Lin demonstrated spatial Airy beams and multiple polarized focusing beams. These results would possibly benefit the plasmonic holography and future display technology.

In recognition of these accomplishments, Lin won "Wang Daheng Optics Award" in 2013 and "Excellent Doctoral Dissertation of Jiangsu Province" in 2015, and a number of awards from Nanjing University.

In summary, this Ph.D. Thesis by Lin Li is outstanding, and is a worthy addition to the Springer Thesis Series.

Nanjing Prof. Tao Li
January 2017

# Acknowledgements

The best science is neither conceived nor performed in isolation. Because of this truth, it is my great pleasure to thank everyone who helped me in my past six years' research journey. It is because of you, the journey became so exciting, fruitful and meaningful.

First and foremost, I would like to sincerely thank my supervisor, Prof. Shining Zhu, for providing me the opportunity to work in an outstanding group. His sound advice, careful guidance, and generous support are invaluable to me during the whole process of conducting my research and writing this dissertation. I am impressed by his vision and confidence. He often proposes ambitious ideas that may appear suspicious to most people at first. During my time in his group, I had the privilege to witness these ideas ultimately realized in ground-breaking experiments. I could not have asked for a better advisor to learn how to do creative research.

I would also like to thank my co-supervisor, Prof. Tao Li, for his kind constant encouragement, support and patient guidance throughout my research. He has helped me to select the proper research topic at the beginning, encouraged me to open my mind, and broadened my research horizon. His contagious enthusiasm and open mind policy for his students greatly helped in my study. In addition, Tao is also a great brother to us, making our life more healthy and exciting.

I would specially like to thank all my colleagues in DSL, who are Prof. Yongyuan Zhu, Prof. Hui Liu, Prof. Ping Xu, Prof. Xiaopeng Hu, Gang Zhao, Xinjie Lv, Peng Lv, Xiaoning Zhao, Qianjin Wang, Shudi Pan, Yalin Yin, Yanxiao Gong, Zhihong Zhu, Xiaoqiang Yu, Junfeng Wang, Hongxia Li, Jingxiao Cao, Zhen Qi, Zhenda Xie, Lina Zhao, Ye Yuan, Jun Lu, Cheng Li, Jianshi Zhao, Hanyang Leng, Yajian Zheng, Sujun Yun, Changdong Chen, Jin Shi, Yi Wang, Hua Jin, Yin Yang, Liangliang Lu, Shiyao Mu, Cong Zhu, Xuhao Hong, Malin Zhong, Shifeng Li, Lei Wang, Yanfei Bai, Qingqing Chen, Chong Sheng, Xiangwen Luo, Ruoyu Guo, Lei Chen, Fei Gao, Juanjuan Yang, Yulin Wang, Qiang Wang, Huibin Lin, Jiong Zou, Fan Zhong, Shushu Wang, Yuxin Li, Panpan Ju, Xudong Jiang, Yichen Liu, Qijin Mo, for their helpful discussions, the great memories together and sincere friendship.

Last but not least, I am deeply grateful to my dear parents, my wife for their constant encouragement, selfless support and endless love. Their love and support helped me get past all the worries and hard time throughout this study.

Nanjing Lin Li
March 2014

# Contents

# Chapter 1
# Introduction

Surface Plasmon Photonics is a rising research field. Due to the development of nanofabrication techniques in the last two decades, it becomes one of the hottest research fields of optics in the 21st century [1, 2]. Surface Plasmon Polaritons (SPPs) or plasmonics are the collective oscillation of the free electrons at the surface of metals. Plasmonics are localized to metal/dielectric interface with highly enhanced the local field, which will largely enhance the light matter interaction and provide us a new way to manipulate the optical information in the nanometer scale. Plasmonics are extensively studied in a lot of areas due to its unique advantage, such as Surface-Enhanced Raman Scattering (SERS) [3–5], extraordinary optical transmission (EOT) [1, 6], medical [7], sensing [8], negative refractive index materials [9, 10], nonlinear frequency conversion [11], solar cell [12], light-matter interaction [13], nano-laser [14], quantum optics [15, 16], and so on.

In these research fields, the research to realize plasmonic chips with subwavelength feature size becomes one of the most attractive fields [1, 17–20]. The development of human society is always associated with rising information hunger, the faster and powerful transfer and processing ability, which drives people to develop the science and technology. In the past half century, we experienced the great development of the electronic industry. The devices have been getting smaller, faster and more efficient. However, the electronic devices meet some fundamental problems when further shrinking the size. The RC delay, which is one of the most important problems, prevents the faster transfer and processing. Meanwhile, photonic devices have great potential to process information fast and to have infinite information capacities, which provide an alternative way to deal with the information. As a result, the photonic devices are wished to replace some of the electronic devices, especially in some key processing parts. Unfortunately, however, limited by the optical diffraction limitation, the feature size of the optical devices ($\sim \mu m$) is much larger than that of electronic devices ($\sim 10$ nm), which seriously obstacles the very large scale integrated photonic devices. In addition, the interconnection between the electronic devices and the photonic devices can hardly be achieved due to the significant size mismatch. It is quite urgent and important to



L. Li, *Manipulation of Near Field Propagation and Far Field Radiation of Surface Plasmon Polariton*, Springer Theses,
DOI 10.1007/978-981-10-4663-6_1

find a new technology to break the optical diffraction limit and realize photonic devices with high density and to interconnect the two different devices. Plasmonics is a wonderful carrier to combine the advantages of the high speed of photonics devices and the high integration of the electronic devices, providing a promising way to solve the problem [1, 21]. Meanwhile, plasmonics will greatly enhance the light matter interaction because the great field enhancement in nanometer scale, as well as the advantage in the high optical density of states and the dispersion, which make it play a very important role in research. Figure 1.1 shows the features of plasmonics [22], in which the importance of the plasmonic devices is also shown. Base on the background of plasmonics, this dissertation will study the basic modulations of plasmonic devices.

In order to realize plasmonic devices, the source, the modulation and the detection are the three major problems. In terms of the source, it is a great challenge to couple light to plasmonics since the momentum mismatch between the wave vectors of plasmonics and the light in free space. However, several coupling schemes were proposed and demonstrated to couple the light in free space, from fiber or even from the integrated semiconductor LED to propagating plasmonics. The coupling efficiency could get as high as about $70 \sim 80\%$ for some SPP waveguides [19, 23, 24]. In the aspect of detection, plasmonics can be coupled into organic photon diodes [25], metal/semiconductor/metal [26], or integrated silicon based photon detectors [27] to get detected. Since both plasmonics and traditional silicon based dielectric devices have merits and demerits, it is more practical to combine the advantages, so that to realize some key parts in super small size with plasmonics, and integrated with traditional SOI waveguides and electronic parts [28]. In addition, it can make good use of the current silicon industry. The key

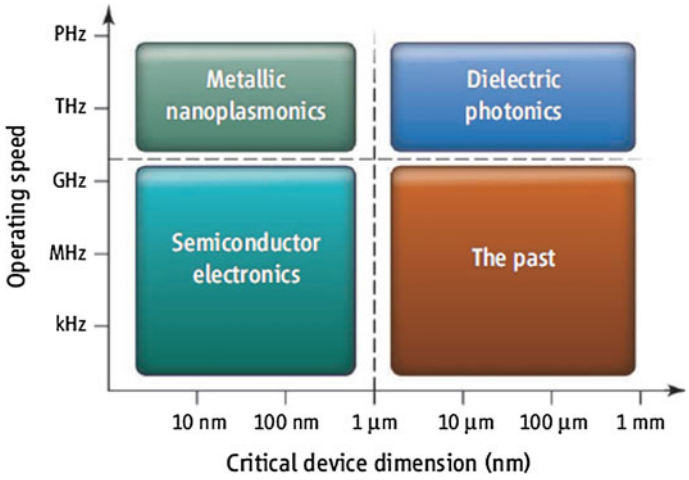


**Fig. 1.1** The feature size and processing speed of electronics, photonics and plasmonic devices. Figure adapted with permission from Ref. [22], AAAS

problem is the coupling between the plasmonic modes and the modes of silicon waveguides. The coupling efficiency can go as high as about 80%.

Although plasmonics show an attractive prospect in subwavelength manipulation and photonic integration, the ohmic loss is an obstacle for real applications. A lot of methods have been proposed to solve this problem, such as making use of the low loss or hybrid SPP modes, introducing gain materials or nonlinear effects to compensate the loss, and so on. On the other hand, as a special two dimensional (2D) electromagnetic mode, SPP has some unique properties in the field distribution, propagation, coupling effects, and so on. As a result, there are rich fundamental problems on the 2D SPP propagation modulation to study. We can only further explore the applications in optical information processing, sensing, optoelectrical effects, and so on, after a clear understanding of these questions. Therefore, this dissertation will mainly focus on the research of SPP propagation and the modulation.

Phase modulation is a powerful way to modulate the optical field. Every progress of phase modulation method will highly improve the modulation abilities on optical field, such as the binary optics [29], phased arrays [30], metasurfaces [31], and so on. In the field of plasmonics, some phase modulation methods were realized based on the coupling process [32–34]. However, the phase modulation with coupling process is not practical for 2D photonic integration. The practical way should achieve the modulation inside the waveguide, that is to realize in-plane field modulation. As a result, it will have great importance to explore new phase modulation methods for in-plane plasmonics modulation and to realize various field modulations with it.

One of the important applications of the plasmonics phase modulation is to achieve special beams. It is gathering a lot of research enthusiasm nowadays to study the special beam steering, especially the non-diffraction beams [35–37]. These non-diffraction beams provide the possibilities to confine the optical intensity in a certain collimated or curved trajectory in free space. It is analogous to the confined optical field with the waveguide in the two dimensional photonic integration. However, because there is no extra structure to confine the field, it is of great possibility to reduce the losses. It is more important for plasmonics since the confinement will induce much higher loss for plasmonics [18]. We also study these non-diffraction beams in plasmonics with the in-plane phase modulation method.

Meanwhile, it is possible to modulate the far-field radiation with plasmonic structures compactly since the highly localized plasmonic field [38–40]. The modulation can be achieved with micrometer sized plasmonic structures, which is a great advantage comparing to the traditional macro optical components, such as lenses, spatial light modulator (SLM) and so on. In addition, it is also possible to modulate the emission of quantum dots, fluorescence, and so on. Furthermore, there are some special applications with plasmonics in the optical orbital momentum beams [41], spin orbital coupling [42], polarization control [43], since the special properties of plasmonics. As a result, it is worth to pay attention to the applications with plasmonics in the optical field and the information modulation.

This dissertation is concerned with my research work on plasmonics based optical modulation. It is organized as follows.

This chapter is the brief introduction of the research background.

In Chap. 2 we first introduce the basics of SPP. The basic features, the phenomena, as well as the preliminary propagation modulation of SPP are demonstrated experimentally.

In Chap. 3 a non-perfectly-matched Bragg diffraction principle is proposed and experimentally verified. Based on this principle, we propose a new phase modulation method, with which any arbitrary phase distribution can be realized. A non-diffraction, self-accelerating plasmonic Airy beam is realized with this phase modulation method.

In Chap. 4 we further discuss the phase modulation method and the applications with the in-plane phase modulation, realizing broad band SPP focusing and demultiplexing, collimated SPP beams with controllable intensity distribution, as well as a non-monotonic SPP beam.

In Chap. 5 we experimentally study the modulation of the far-field radiation with plasmonic structures. By extending the in-plane phase modulation method to the modulation in 3D free space, the beam with optical orbital angular momentum with an integrated radius phase modulation is realized. In addition, we propose a polarization reconfiguration method with the alternative scattering properties of the transverse and longitudinal SPP modes, and experimentally verify this scheme and realize polarization controlled beams (such as directional beaming, Airy beam, focusing, etc.) based on this method, indicating its exciting applications in information technology.

Chapter 6 is the summary and the outlooks.

## References

1. Barnes WL, Dereux A, Ebbesen TW (2003) Surface plasmon subwavelength optics. Nature 424:824–830
2. Surface plasmon resurrection. Nat Photonics 6:707–707 (2012)
3. Fleischm M, Hendra PJ, Aj Mcquilla (1974) Raman-spectra of pyridine adsorbed at a silver electrode. Chem Phys Lett 26:163–166
4. Jeanmaire DL, Vanduyne RP (1977) Surface raman spectroelectrochemistry. 1. Heterocyclic, aromatic, and aliphatic-amines adsorbed on anodized silver electrode. J Electroanal Chem 84:1–20
5. 任斌, 田中群 (2004) 表面增强拉曼光谱的研究进展
6. Ebbesen TW, Lezec H, Ghaemi H, Thio T, Wolff P (1998) Extraordinary optical transmission through sub-wavelength hole arrays. Nature 391:667–669
7. Hirsch LR, Stafford RJ, Bankson JA, Sershen SR, Rivera B, Price RE, Hazle JD, Halas NJ, West JL (2003) Nanoshell-mediated near-infrared thermal therapy of tumors under magnetic resonance guidance. Proc Natl Acad Sci USA 100:13549–13554
8. Nylander C, Liedberg B, Lind T (1982) Gas-detection by means of surface-plasmon resonance. Sens Actuator 3:79–88
9. Seddon N, Bearpark T (2003) Observation of the inverse Doppler effect. Science 302:1537–1540

10. Pendry JB, Schurig D, Smith DR (2006) Controlling electromagnetic fields. Science 312:1780–1782
11. Kim S, Jin J, Kim Y-J, Park I-Y, Kim Y, Kim S-W (2008) High-harmonic generation by resonant plasmon field enhancement. Nature 453:757–760
12. Atwater HA, Polman A (2010) Plasmonics for improved photovoltaic devices. Nat Mater 9:205–213
13. Akimov AV, Mukherjee A, Yu CL, Chang DE, Zibrov AS, Hemmer PR, Park H, Lukin MD (2007) Generation of single optical plasmons in metallic nanowires coupled to quantum dots. Nature 450:402–406
14. Berini P, De Leon I (2012) Surface plasmon-polariton amplifiers and lasers. Nat Photonics 6:16–24
15. Jacob Z, Shalaev VM (2011) Plasmonics goes quantum. Science 334:463–464
16. Tame MS, McEnery KR, Ozdemir SK, Lee J, Maier SA, Kim MS (2013) Quantum plasmonics. Nat Phys 9:329–340
17. Zia R, Schuller JA, Chandran A, Brongersma ML (2006) Plasmonics: the next chip-scale technology. Mater Today 9:20–27
18. Gramotnev DK, Bozhevolnyi SI (2010) Plasmonics beyond the diffraction limit. Nat Photonics 4:83–91
19. Bozhevolnyi SI (2009) Plasmonic nanoguides and circuits. Distributed by World Scientific Publishing, Singapore
20. Ebbesen TW, Genet C, Bozhevolnyi SI (2008) Surface-plasmon circuitry. Phys Today 61:44
21. Zayats AV, Smolyaninov II (2003) Near-field photonics: surface plasmon polaritons and localized surface plasmons. J Opt A-Pure Appl Opt 5:S16–S50
22. Brongersma ML, Shalaev VM (2010) The Case for Plasmonics. Science 328:440–441
23. Raether H (1988) Surface-plasmons on smooth and rough surfaces and on gratings. Springer Tr Mod Phys 111:1–133
24. 王振林 (2009) 表面等离激元研究新进展. 物理学进展 29:287–324
25. Ditlbacher H, Aussenegg FR,Krenn JR, Lamprecht B, Jakopic G, Leising G (2006) Organic diodes as monolithically integrated surface plasmon polariton detectors. Appl Phys Lett 89
26. Neutens P, Van Dorpe P, De Vlaminck I, Lagae L, Borghs G (2009) Electrical detection of confined gap plasmons in metal-insulator-metal waveguides. Nat Photonics 3:283–286
27. Falk AL, Koppens FHL, Yu CL, Kang K, Snapp ND, Akimov AV, Jo MH, Lukin MD, Park H (2009) Near-field electrical detection of optical plasmons and single-plasmon sources. Nat Phys 5:475–479
28. Briggs RM, Grandidier J, Burgos SP, Feigenbaum E, Atwater HA (2010) Efficient coupling between dielectric-loaded plasmonic and silicon photonic waveguides. Nano Lett 10: 4851–4857
29. Veldkamp WB, Mchugh TJ (1992) Binary Optics. Sci Am 266:92–97
30. Mailloux RJ (2005) Phased array antenna handbook, 2nd edn. Artech House, Norwood
31. Yu NF, Genevet P, Kats MA, Aieta F, Tetienne JP, Capasso F, Gaburro Z (2011) Light propagation with phase discontinuities: generalized laws of reflection and refraction. Science 334:333–337
32. Zhao CL, Zhang JS (2010) Plasmonic demultiplexer and guiding. Acs NANO 4:6433–6438
33. Minovich A, Klein AE, Janunts N, Pertsch T, Neshev DN, Kivshar YS (2011) Generation and near-field imaging of airy surface plasmons. Phys Rev Lett 107:116802
34. Laluet J-Y, Devaux E, Genet C, Ebbesen TW, Weeber J-C, Dereux A (2007) Optimization of surface plasmons launching from subwavelength hole arrays: modelling and experiments. Opt Express 15:3488–3495
35. Durnin J (1987) Exact-solutions for nondiffracting beams. 1. The scalar theory. J Opt Soc Am A 4:651–654
36. Siviloglou GA, Broky J, Dogariu A, Christodoulides DN (2007) Observation of accelerating airy beams. Phys Rev Lett 99:213901

37. Froehly L, Courvoisier F, Mathis A, Jacquot M, Furfaro L, Giust R, Lacourt PA, Dudley JM (2011) Arbitrary accelerating micron-scale caustic beams in two and three dimensions. Opt Express 19:16455–16465
38. Jun YC, Huang KCY, Brongersma ML (2011) Plasmonic beaming and active control over fluorescent emission. Nat Commun 2
39. Aouani H, Mahboub O, Bonod N, Devaux E, Popov E, Rigneault H, Ebbesen TW, Wenger J (2011) Bright unidirectional fluorescence emission of molecules in a nanoaperture with plasmonic corrugations. Nano Lett 11:637–644
40. Yu NF, Wang QJ, Capasso F (2012) Beam engineering of quantum cascade lasers. Laser Photonics Rev 6:24–46
41. Gorodetski Y, Drezet A, Genet C, Ebbesen TW (2013) Generating far-field orbital angular momenta from near-field optical chirality. Phys Rev Lett 110:203906
42. Yin XB, Ye ZL, Rho J, Wang Y, Zhang X (2013) Photonic spin hall effect at metasurfaces. Science 339:1405–1407
43. Huang LL, Chen XZ, Muhlenbernd H, Zhang H, Chen SM, Bai BF, Tan QF, Jin GF, Cheah KW, Qiu CW, Li JS, Zentgraf T, Zhang S (2013) Three-dimensional optical holography using a plasmonic metasurface. Nat Commun 4

# Chapter 2
# Experimental Basics of Surface Plasmon Polaritons

Surface plasmon polaritons (SPPs) are propagating excitations that arise from the coupling of light with collective oscillations of the electrons at the surface of a metal. SPPs are highly localized to the interface of the metal/dielectric [1, 2], so that the intensity is greatly enhanced at the 2-dimentional (2D) interface. The enhancement makes the SPPs very sensitive to the condition of the interface and it has gathered great research interests in several fields, such as surface-enhanced Raman scattering (SERS), nonlinear optics, fluorescence enhancement, and so on. On the other hand, as a natural 2D system, SPP is a promising candidate for the all optical integrated circuits [2, 3]. It is well known that photon is better than electron as an information carrier, while photon is not as good as electron in integration. SPP is a promising carrier to make photonic devices more integrated, so that it becomes a very hot research topic in photonics.

However, the dispersion of SPP lies to the right side of the light cone. The wavevector of SPP is larger than that of light, which prevents the direct coupling between SPP and the light in free space. The problem was solved with the development of nanofabrication technology. As a result, more and more research on SPP was carried out, on both theoretical and experimental sides, which provided people better understanding of SPP. A series of remarkable progresses have been achieved on the modulation of SPP propagation, which will be very good references for the future all-optical integration.

In this chapter, we will first introduce the basic physics of SPPs. It will followed by the introduction of the excitation and the observation of SPPs in experiment. We will specially discuss leakage radiation microscopy (LRM), which is a very popular observation method for SPPs and it is also used in our research. With these experiment preparations, we will then introduce some preliminary in-plane manipulation of the SPPs with the Bragg's principle, such as Bragg mirrors, MZ-interferometers, and so on.



L. Li, *Manipulation of Near Field Propagation and Far Field Radiation of Surface Plasmon Polariton*, Springer Theses,
DOI 10.1007/978-981-10-4663-6_2

## 2.1 Introduction of Surface Plasmon Polaritons

SPPs are a collective electrons density waves at the surface of a metal, which are intrinsically two dimensional excitation. The electromagnetic field of SPPs decays exponentially with the distance from the dielectric/metal interface, so that SPPs are localized to the surface. Figure 2.1 is the scheme of SPPs, which shows the oscillating nature of the surface charge density and the associated fields. The penetration depths of the field into the dielectric and the metal are around 100 and 10 nm [1] in the visible range, respectively.

SPPs were first observed by Wood in 1902; he found unexplained features in optical reflection measurements on metallic gratings, which is called Wood's anomaly [1, 4]. Fano attributed the anomaly to the excitation of a surface mode in 1936 [5, 6]. Later on, Stern and Frerell proposed that the surface mode is related to the coupling between electromagnetic field and the surface plasmon [7]. They introduced the dispersion of the surface mode for the first time. This surface electromagnetic mode is SPPs.

The dispersion of SPPs can be derived from the Maxwell equations for dielectric/metal interface. As shown in Fig. 2.2, there is no boundary orthogonal to

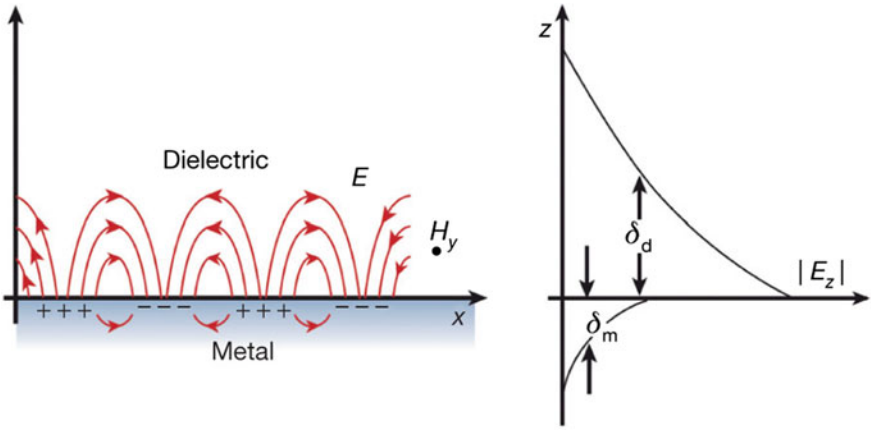


**Fig. 2.1** The scheme of SPP. The right panel is the penetration depth of SPP into the dielectric and metal. Figure adapted with permission from Ref. [2], Macmillan Publishers Ltd.


**Fig. 2.2** Infinite metal/dielectric interface

*Ex*, which is conserved across the boundary. While the case for the normal component *Ez* is different, and *Dz* should be continuous. For the TM (transverse magnetic) mode at the interface, we have

$$H_y^d(z) = A_2 e^{i\beta x} e^{-k_2 z} \tag{2.1}$$

$$H_y^m(z) = A_1 e^{i\beta x} e^{k_1 z} \tag{2.2}$$

The electric field can be derived from Maxwell equations as:

$$E_x^d(z) = iA_2 \frac{1}{\omega\varepsilon_0\varepsilon_2} k_2 e^{i\beta x} e^{-k_2 z} \tag{2.3}$$

$$E_z^d(z) = -A_1 \frac{\beta}{\omega\varepsilon_0\varepsilon_2} e^{i\beta x} e^{-k_2 z} \tag{2.4}$$

$$E_x^m(z) = -iA_1 \frac{1}{\omega\varepsilon_0\varepsilon_1} k_1 e^{i\beta x} e^{-k_1 z} \tag{2.5}$$

$$E_z^m(z) = -A_1 \frac{\beta}{\omega\varepsilon_0\varepsilon_1} e^{i\beta x} e^{-k_1 z} \tag{2.6}$$

In which $\varepsilon_{1,2}$ are the corresponding permittivities of the metal and dielectric, $\beta$ is the wave vector of SPP mode. The relationship between the normal components of the wavevectors and the dielectric constants in the two media is restricted by the boundary conditions as

$$\frac{k_2}{k_1} = -\frac{\varepsilon_2}{\varepsilon_1} \tag{2.7}$$

while

$$k_1^2 = \beta^2 - k_0^2\varepsilon_1, \quad k_2^2 = \beta^2 - k_0^2\varepsilon_2 \tag{2.8}$$

By solving the equations 2.7 and 2.8, we have

$$\beta = k_0 \sqrt{\frac{\varepsilon_1\varepsilon_2}{\varepsilon_1 + \varepsilon_2}} \tag{2.9}$$

which is the dispersion of SPPs.

While for the transverse electric (TE) mode, there is no normal solution with similar derivation. It means there is no surface electromagnetic mode with TE polarized light incident. It is because TE polarized light only have the electric component in *y* direction and it cannot create polaritons at the interface.

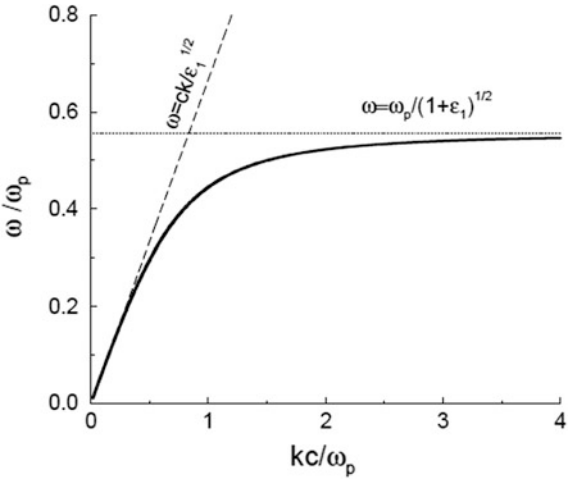


**Fig. 2.3** The dispersion of SPPs at the interface of Ag/air (*solid black curve*). The *black dash line* is the light cone

Generally, the relative permittivities of metals follow Drude or Drude-Lorenz dispersion models in the visible range which we are interested in:

$$\varepsilon_m(\omega) = 1 - \frac{\omega_p^2}{\omega(\omega + i\gamma)} \tag{2.10}$$

in which $\omega_p$ is the plasma frequency and $\gamma = 1/\tau$ is the scattering rate which is used to account for dissipation (through scattering) of the electron motion. $\omega_p$ of silver is $1.37 \times 1016\ s^{-1}$. It is much larger than that of visible light, so that the relative permittivity has a large negative real part [8]. In this case, the wavevector of SPPs ($k_{SPPs}$) is usually larger than that of corresponding frequency in free space ($k_0$). As shown in Fig. 2.3, the dispersion of SPPs lies completely at the right-side of the dispersion of light in free space, which means that we cannot couple light to SPPs directly because of the momentum mismatch [9]. It also represents the non-radiative or bound nature of the SPPs.

The decaying fields of the SPPs in the dielectric and the metal follow the equations of 2.3–2.6, which showing the exponential decay. $L_m$ and $L_d$ are the penetration depth of the SPPs in the metal and dielectric respectively, which defined by $L_m = 1/2k_1$ and $L_d = 1/2k_2$ where the electric fields fall to $1/e$ to that of the interface. In terms of Eq. 2.8, the penetration depth $L_m$ of SPP into the metal is

$$L_m = 1/2k_1 \approx \lambda/4\pi\sqrt{|\varepsilon_1|}$$

While the penetration depth $L_d$ of SPP into the dielectric is given by

$$L_d = 1/2k_2 = \lambda\sqrt{|\varepsilon_1|}/4\pi\varepsilon_2$$

The penetration depth of $L_m$ and $L_d$ are about 12 and 213 nm at the wavelength of 633 nm in free space. $L_m$ is much smaller than the corresponding wavelength in free space, which is one of the reasons the SPPs is taken as a two dimensional mode. Meanwhile, the electromagnetic field is highly enhanced around the interface. As a result, SPP gathering plenty of research enthusiasm in optical integration, Raman, and so on.

The SPPs have limited propagation length since there are no ideal metal in the real world. Instead, all of the metals have certain ohmic loss and the relative permittivity is a complex number (2.10). The permittivity can be written in short as $\varepsilon_1 = \varepsilon_{1r} + i\varepsilon_{1i}$, while the corresponding wavevector of SPP is a complex number as $\beta = \beta_r + i\beta_i$ Generally, the absolute value of the real part of the relative permittivity of metal is larger than that of the imaginary part in visible range. The real and imaginary part of the wavevector of SPP can be proximately written as:

$$\beta_r = k_0\sqrt{\frac{\varepsilon_{1r}\varepsilon_2}{\varepsilon_{1r}+\varepsilon_2}}, \quad \beta_i = k_0\left(\frac{\varepsilon_{1r}\varepsilon_2}{\varepsilon_{1r}+\varepsilon_2}\right)^{3/2}\frac{\varepsilon_{1i}}{2\varepsilon_{1r}^2} \tag{2.11}$$

The propagation length of SPP can be obtained from the imaginary part of $\beta$. This propagation length is defined as the distance over which the intensity of the SPPs mode falls to 1/e of its initial value, is given by $\delta_{SPP} = 1/2\ \beta_i$. It is:

$$L_{sp} = \frac{1}{2\beta_i} = \frac{1}{k_0}\left(\frac{\varepsilon_{1r}+\varepsilon_2}{\varepsilon_{1r}\varepsilon_2}\right)^{3/2}\frac{\varepsilon_{1r}^2}{\varepsilon_{1i}} \tag{2.12}$$

The propagation length is about 20 μm when the free space wavelength is 633 nm [8].

Above is a discussion of an example of the basics of SPPs in an infinite dielectric/metal interface. However, the discussion is not limited in this system. It covers a lot of different systems, such as the long range SPP (LRSPP) in a dielectric/metal/dielectric system with a very thin metal layer in the center [10], metal/dielectric/metal (MIM) system [11, 12], channel plasmon polariton (CPP) in the V shaped grooves [13], and even the mode in the metallic nanowires [14]. The related dispersion relation can be obtained by solving Maxwell equation in a corresponding boundary condition, or from a commercial numerical simulation tool.

## 2.2 Surface Plasmon Polaritons Excitation and Observation

Generally, the dispersion curve of SPPs lies on the right-side of that of light in free space, which gives rise to a momentum mismatch (Fig. 2.3). The incident light can't be coupled to the SPPs automatically. Various coupling configurations are proposed to match the momentum of light and SPPs to excite SPPs and measure them, such as using prism coupler, grating, waveguide coupler and fibers, and so on.

### 2.2.1 Optical Excitation of Surface Plasmon Polaritons

Below are the main coupling configurations used to match the momentum mismatch and couple the light to SPP [8, 9]:

**Prism coupling**. This coupling scheme includes Kretschmann geometry [15] and Otto geometry [16] as shown in Fig. 2.4a, b. In Kretschmann geometry, the metal film on a prism is illuminated through the dielectric prism at an angle of incidence greater than the critical angle or the total internal reflection angle (ATR). An evanescent wave is generated and the in plane wavevector is $k_{\parallel} = nk_0 \sin\theta$. n is the refractive index of the dielectric and it is larger than $n_{SPP,}$ which is the effective index of the SPP at the metal/air interface. So that at certain incident angle the in-plane component of the wavevector in the prism coincides with that of the SPP on matal/air interface ($k_{\parallel} = n_{SPP}$), which gives rise to the light tunneling through the metal film and the light is coupled to SPP. In Otto geometry, the metal film is put close to a prism, where the total internal reflection happens. The evanescent wave will tunnel through the air and coupled to SPP at certain angle which is analog to that of Kretschmann geometry. The coupling efficiency can get almost 100% with these two configurations.

**Near field coupling**. SPP can be excited with a subwavelength size tip when put the tip close to the metal surface (Fig. 2.4c). It is possible since all the wavevectors exist in the light from the tip in the near field, in which the wavevector matches the SPP also exists [17]. The SPP excitation condition can be achieved with the defect on the metal surface as well. The mechanism is analog to the coupling with a near field tip. The scattering light in the near field contains the wavevector which matches that of SPP, so that SPP can be exited (Fig. 2.4b) [18].

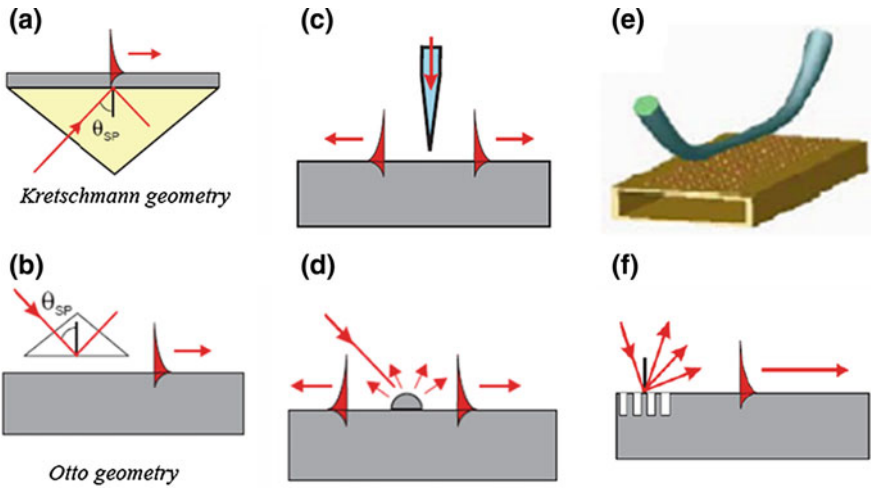


**Fig. 2.4** The excitation of SPP. **a**, **b** Prism coupling. **c**, **d** Near field coupling. **e** Waveguide mode coupling. **f** Grating coupling. Figure adapted with permission from Ref. [9], Elsevier

**Waveguide mode coupling**. There is an evanescent field at the near field of a waveguide. SPP could be excited when a waveguide with a guide mode match the mode of SPP approaching the metal surface. The metal/dielectric interface should be put in the evanescent region of waveguide mode in this coupling configuration. Figure 2.4e is an example of this configuration, where the SPP is excited by approaching a fiber to a metal surface.

**Grating coupling**. A periodic grating will provide certain momentum compensation to an incident light, which could match the mismatch between the momentum of the free space light and that of SPP. That is $\mathbf{G} = \Delta k = k_{SPP} - k_0$, where **G** is the reciprocal vector of the grating. SPP excitation condition can be achieved with the grating coupling (Fig. 2.4f) [19]. We will excite SPP with this way since it is more convenient to control.

### *2.2.2 Observation of Surface Plasmon Polaritons*

The SPP can't be coupled to free space light automatically as well because of the momentum mismatch. A certain way is required to observe the propagation of SPP. There are some popular ways to observe SPP, such as near field scanning optical microscope (NSOM) [20], imaging with fluorescent dye [21], and leakage radiation microscopy (LRM) [22]. NSOM provides a way to directly collect the information near the metal surface where the SPPs exists. It is straight forward and trustable, so that a lot of works are measured in this way. However, due to the high cost, complicated operation, time consuming, limited image area, as well as the limitation in resolving frequencies, it is not widely used. Fluorescent dye is also used to image SPPs. Fluorescent dyes are coated to the surface of metal film and they can be excited by the propagating SPPs, so that the SPPs are recorded by the fluorescent. This method is limited by the blenching of the fluorescent dye. The imaging quality is not good as well. LRM is an alternative way to be used to observe SPPs. The mechanism of LRM is the same as normal microscope so that it is quite simple to be operated. It is convenient to get a Fourier image of SPPs with LRM as well as some flexible modifications for special purpose. In addition, there are no drawbacks of the other two methods and the cost is no high as well. As a result, more and more groups start to make use of LRM system. In this dissertation, we also use LRM system to observe the behavior of SPPs on metal surface.

The principle of LRM was first proposed by Hecht et al. [17, 22, 23] and experimentally verified. It is schematically shown in Fig. 2.5. An incident light is coupled to SPP with certain structures on silver surface. Some of the SPP will leak through the silver film to the interface of silver/SiO2 when the silver film is thin enough (i.e., the thickness of silver film is less than 100 nm). Since the refractive index of $SiO_2$ is larger than that of SPP ($n_{SPP}$) at silver/air, the leakage wave will couple to free space in $SiO_2$ with a certain angle $\theta$, where $nk_0\cos\theta = k_{SPP}$. The light can be collected with an objective with high numerical aperture (NA), where the NA is larger than $n_{SPP}$, so that to get the information of the SPPs. The LRM is not

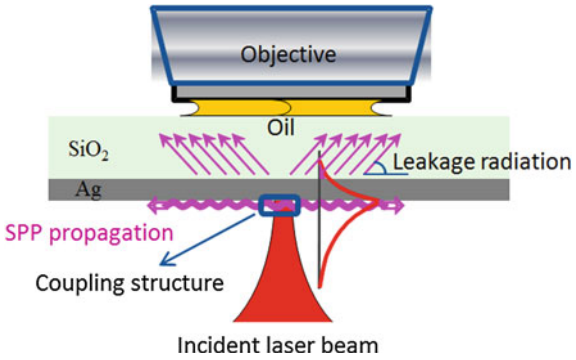


**Fig. 2.5** The scheme of LRM system

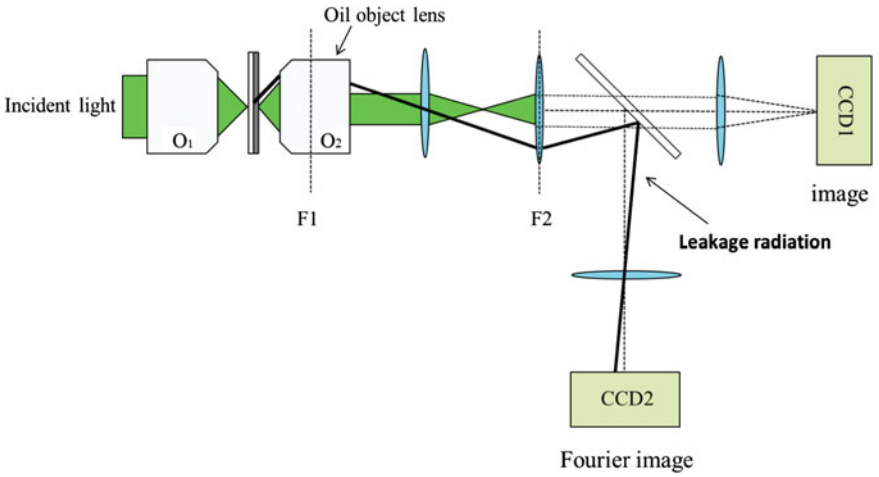


**Fig. 2.6** The experiment setup of LRM system

limited to observe SPPs, but also can be used to observe some waveguide mode which can't be directly observed with normal microscope.

The optical system is shown in Fig. 2.6. An incident light is focused on the structure on the metal surface by an objective lens $O_1$ (50×, NA is 0.55) and is coupled to SPPs. Part of the SPPs will leak through the metal film to the $SiO_2$ side when the SPP propagates along the interface. This part of SPP will be collected with an oil immersion objective lens with high NA ($O_2$, 100×, NA is 1.40) and projected to a charge-coupled-device (CCD) camera (CCD1). Meanwhile, the back focal plane (or the Fourier plane) of the oil immersion objective is also projected to another CCD camera (CCD2) simultaneously. In addition, a beam blocker can be put in the imaging plane or the Fourier plane at the position of F2 to filter the information in the real space or the reciprocal space (k-space) so that to get better contrast for the information we want [24, 25]. We will discuss more about it in the following chapters.

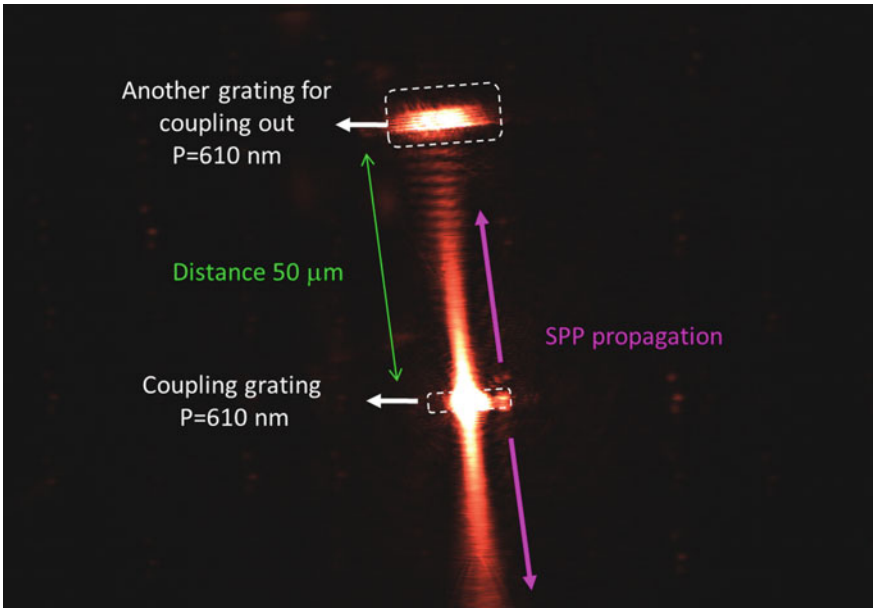


**Fig. 2.7** The typical SPP propagation image measure with LRM system

Figure 2.7 is a typical image of SPP propagation observed by LRM system. The SPP was excited by the light from a He-Ne laser with the wavelength of 633 nm by a periodic grating with the depth of 20 nm. The period of the grating is 610 nm, which is close to the corresponding wavelength of the SPPs. The SPPs propagate to both side of the grating and they are perpendicularly to it. It is clear to see the propagation in 50 μm from the grating on both sides. There is another grating with period of 610 nm and depth of 30 nm at 50 μm away from the in-coupling grating to couple the SPP to light in free space. The intensity of it is much larger than the nearby SPP observed by LRM, which means only little part of SPP can be observed with the LRM. However we can still study the behavior of the SPP with LRM.

Figure 2.8 is the SPP excited with a hexagonal hole array observed with LRM. There are SPPs in six directions because the match condition are achieved in the six directions with the hexagonal lattice. Meanwhile we can also observe the corresponding image in the Fourier plane. There are six sharp arcs, which are the corresponding wavevectors of the SPPs.

### *2.2.3 The SPP Fringes Observed with LRM*

There is a periodic intensity pattern closed to the out-coupling grating in Fig. 2.7, which was not reported with other measurement methods, such as NSOM, but can be observed with LRM usually as shown in Fig. 2.9a. The period of the pattern is

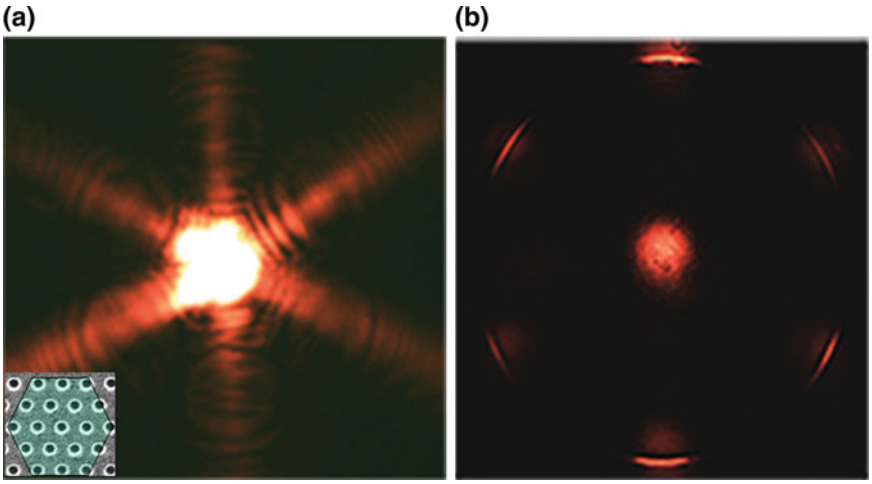


**Fig. 2.8** SPP coupling with hexagonal nanoarray. **a** SPP propagation in real space. **b** Corresponding image in the reciprocal space

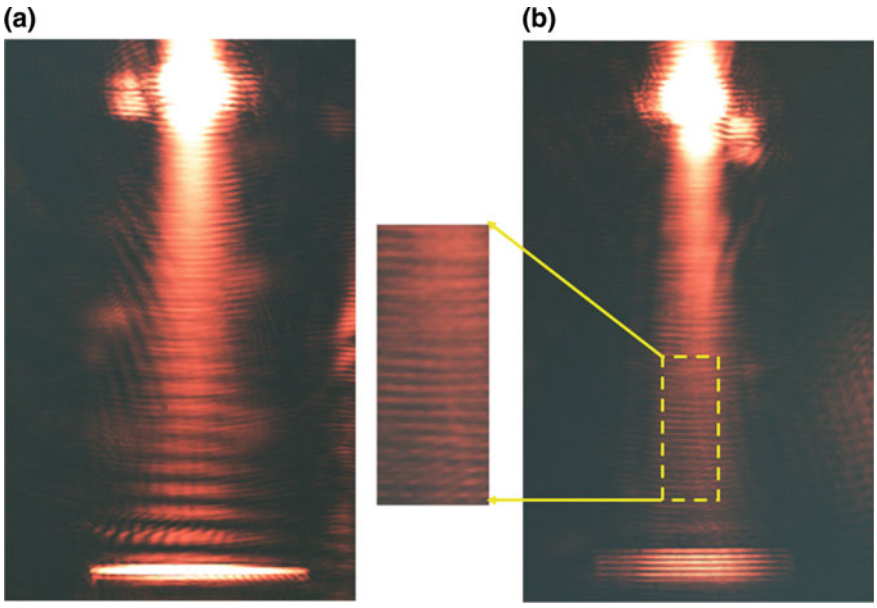


**Fig. 2.9** SPP interference fringes observed with LRM. The out-coupling grating is deep (**a**) and shallow (**b**)

around 2 μm. Actually, when we reduce the depth of the out-coupling grating, a different periodic pattern can be observed as shown in Fig. 2.9b. Is there any relationship between the two fringes? What's the physics behind the phenomenon?

As we all know, an interference will happen when two waves meet with each other and caused a periodic intensity pattern which is called beat pattern. There is beat pattern in optics since light is an electromagnetic wave. In our experiment, we didn't use any other light except the incident laser light with the wavelength of 633 nm. There is no strong nonlinear conversion set up as well, so that the periodic pattern should come from the light with the same frequency but different wavevectors.

We first considered the condition with shallow gratings shown in Fig. 2.9b since there is less disturbing information. Figure 2.10a is the intensity distribution of an arbitrary line along the propagation of the SPPs and a periodic pattern can be roughly observed. A Fourier transformation is performed to get a better analysis. The result is shown in Fig. 2.10b, where a peak is shown and it is related to a period of 305 nm in real space. It means the intensity pattern is periodic and the period is about 305 nm, which is half of the wavelength of SPPs. Two counter propagating SPP can generate an intensity pattern with the period of half wavelength of the SPPs.

SPPs will be reflected when it meets obstacles, such as a slit or grating. The reflectance will be much higher when the period of the grating is an integer multiple of the half wavelength. The reflected SPPs and incident SPPs will propagate toward each other and the intensities are similar near the out-coupling grating. As a result a clear interference pattern with the period of half wavelength can be observed near the grating. However, since SPP will attenuate quickly when it propagates, the intensities of the forward and backward SPP will be quite different, so that the visibility of the interference pattern close to the in-coupling grating is not as good as that close to the out-coupling grating, which agrees well with the result shown in Fig. 2.9. Thus it is clear that the periodic intensity pattern in Fig. 2.9b is caused by the interference of the forward SPP and the backward SPP reflected by the out-coupling grating. A similar work was reported by Drezet et al. [26], which proved above explanation.

A similar analysis can be performed to Fig. 2.9a. The intensity of the SPP along the propagation in Fig. 2.9a is shown in the inset of Fig. 2.11a. There is a fringe

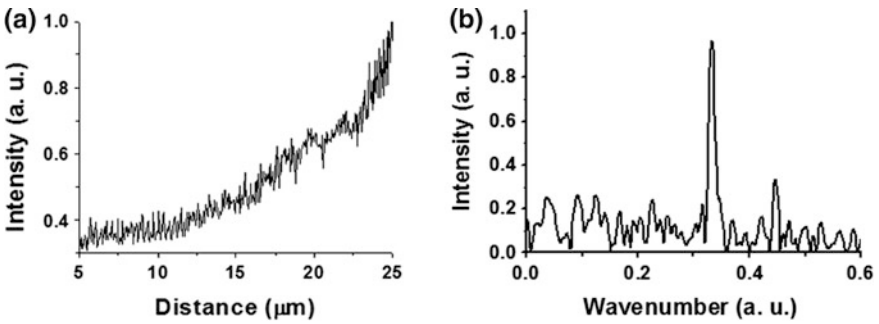


**Fig. 2.10** The first type of the SPP interference fringes. **a** The fringes in the real space. **b** The Fourier transformation result of the fringes

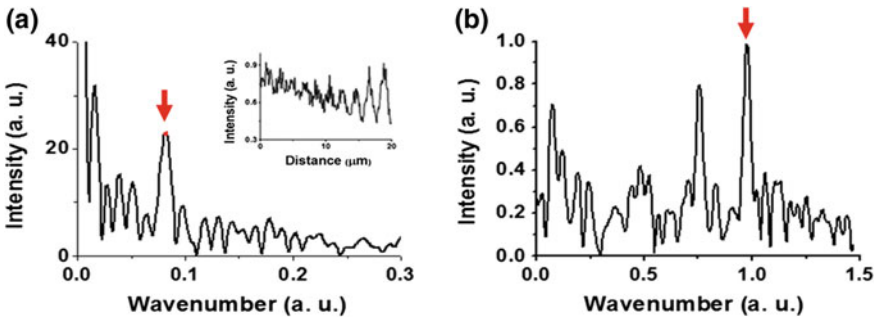


**Fig. 2.11** The Fourier transformation results of the second SPP interference fringes. The results for the fringes with larger periodicity (**a**) and smaller one (**b**). The inset of **a** is the typical interference fringe to be transformed

with smaller periodicity except for the relative larger periodicity mentioned above ($\sim$2 μm). With the similar approach used above, we got several intensity distribution of the SPP along the propagation and performed Fourier transformation to them. Figure 2.11a, b are the typical results with the transformation for the two periodicity, where the red arrows indicate the peaks related to the periodicities. The corresponding period are 1.87 and 0.26 μm. The two periodicities are caused by waves with two different "wavevectors", and one of the wave is SPP. The two periods can be deduced from the principle of beat pattern as:

$$\Lambda_l = \left|\frac{\lambda_{SPP}\cdot\lambda_u}{\lambda_{SPP}-\lambda_u}\right|, \quad \Lambda_s = \frac{\lambda_{SPP}\cdot\lambda_u}{\lambda_{SPP}+\lambda_u} \tag{2.13}$$

where $\lambda_u$ is the wavelength of the unknown wave. Based on the observed data, the unknown wavelength $\lambda_u$ is about 460 nm deduced from Eq. 2.13, which means the beat pattern is caused by the interference between the SPP and a wave with the "wavelength" of 460 nm. However there is no such wave in our system. Where does it come from?

To further analysis the special phenomenon, a modification is made to the LRM system. We can set certain blockers in the optical system to block the information in the real or the reciprocal space (k-space or Fourier space) so that to get a clearer analysis for the images as we discussed before. Figure 2.12 are the images of the real and the corresponding k-space after certain blocking set ups. Figure 2.12a are the images observed without any blocking and Fig. 2.12b–d are the images observed after blocking the intensity of the −1st, 0th and the 1st diffraction orders from the k-space. When the −1st order is blocked, the down going SPP disappears (Fig. 2.12b), while the upper going SPP disappears when the 1st order is blocked. When the 0th order is blocked, the SPP seems not been impacted and we can only observe some reduction of the intensity from the grating. It is clear that the SPPs correlate well with the 1st and the −1st intensity in the k-space and the "beat pattern" is related to the down going SPP.

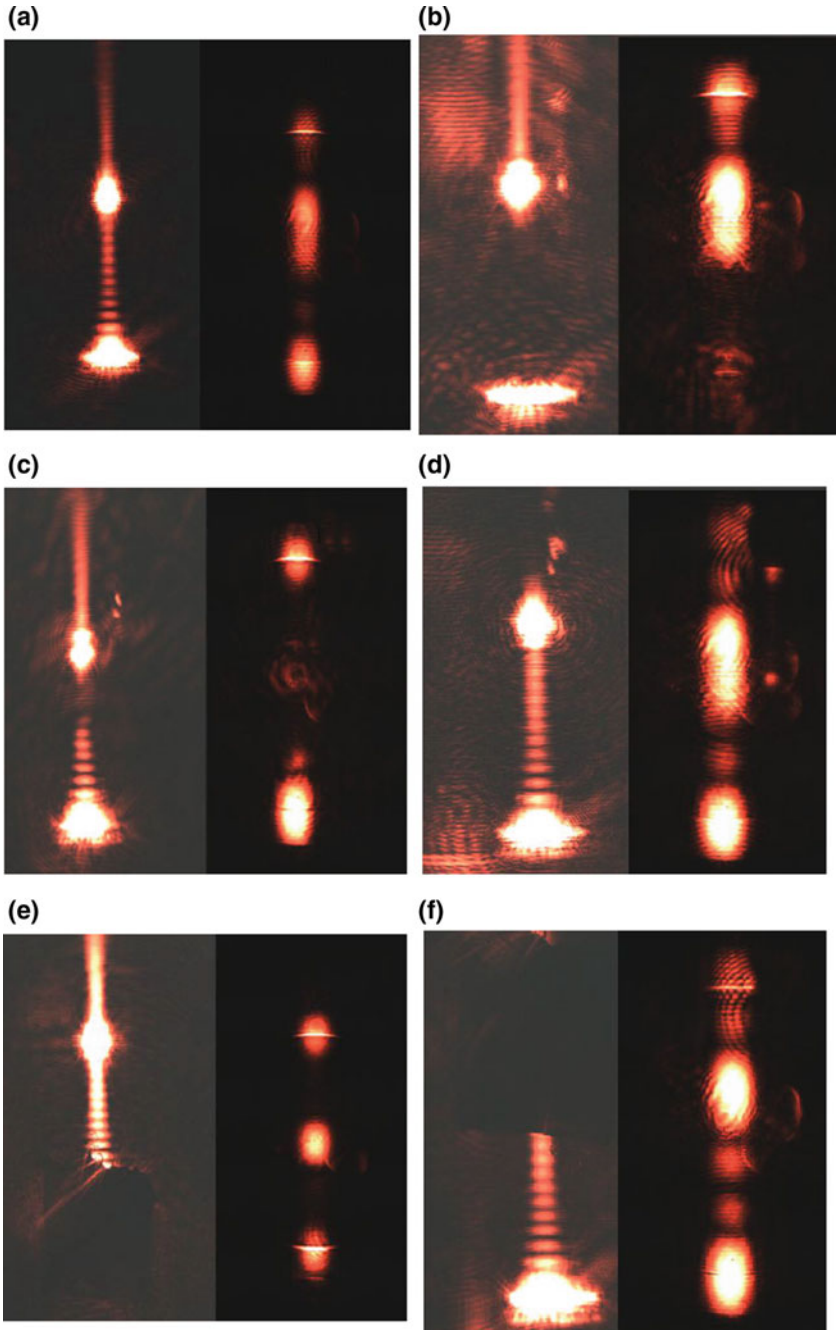


**Fig. 2.12** The results with space filters added in the measurement system

Similarly, we blocked the information in the real space as shown in Fig. 2.12e, f, where the area near the out-coupling grating and the in-coupling grating were blocked respectively. The 0th and the −1st order were changed a lot while the 1st order just has little intensity change in the image of the k-space (Fig. 2.12e) when the area around the out-coupling grating was blocked. The image is analog to the image without out-coupling gratings shown in Fig. 2.8, which means the intensity from the out-coupling grating is mainly around the area in the k-space. When the in-coupling grating was blocked, no significant change in k-space except the intensities. It is concluded that the beat pattern is mainly come from the appearance of the out-coupling grating. The pattern will be weaker when the grating is shallower or even disappear. The pattern is formed by the interference between a wave with the wavelength of around 460 nm and the SPP, and it probably come from the signal around 0th order and the −1st order in the k-space.

On the other hand, the wavevector is $k_u = 2\pi/\lambda_u \approx 1.38k_0$ for the wave, where the ratio 1.38 is quite close to the NA of the oil immersion lens 1.4. As a result, the beat pattern is probably related to the restriction of the numerical aperture of the objective.

To sum up, the out-coupling grating induces a strong background from the 1st to the −1st of the diffraction in the k-space. The background is limited by the numerical aperture of the objective. As a result, except for the direct transmission of the incident laser, there're two components observed in LRM system. One of them is the propagating SPP $S(k_{SPP})$, while the other is the background caused by the out-coupling grating $B(k_u)$. The observed pattern is caused by the interference of the two components. We analyzed the intensity distribution under this assumption. $B(k_u)$ is the intensity of the background which is limited to $-k_0NA < k_u < k_0NA$ by the numerical aperture of objective in k-space. Assume the background intensity is uniform in k-space and

$$B(k_u) = a, \tag{2.14}$$

$a$ is the test intensity of the background,

$$S(k_{SPP}) = \frac{1}{2\pi}\left[\delta(k - k_{SPP}) + \frac{i}{k_{SPP}}\frac{\partial}{\partial k}\delta(k - k_{SPP})\right] \tag{2.15}$$

The intensity of the real space can be deduced from the inverse Fourier transformation to 2.14 and 2.15,

$$FT^{-1}[S(k_{SPP})] = \sqrt{\frac{2}{\pi x}}e^{i(k_{SPP}x - \pi/4)} \tag{2.16}$$

$$FT^{-1}[B(k_u)] = \int_{-k_0NA}^{k_0NA} ae^{ikx}dk = \frac{a}{x}\left(e^{ik_0NAx} - e^{-ik_0NAx}\right) \tag{2.17}$$

The overall intensity distribution is the interference of the two components:

$$I \propto |E(x)|^2 = \left| \sqrt{\frac{2}{\pi x}} e^{i(k_{SPP}x - \pi/4)} + \frac{a}{x}\left(e^{ik_0 NAx} - e^{-ik_0 NAx}\right) \right|^2 \tag{2.18}$$

The intensity pattern from formula 2.18 is a "beat pattern" caused by two wavevector of $k_{SPP}$ and $k_0 NA$. The larger and smaller period are $\Lambda_l = \left|\frac{\lambda_{SPP} \cdot \lambda_{k_0 NA}}{\lambda_{SPP} - \lambda_{k_0 NA}}\right| = 1.747$ and $\Lambda_s = \frac{\lambda_{SPP} \cdot \lambda_{k_0 NA}}{\lambda_{SPP} + \lambda_{k_0 NA}} = 0.26$, which are very close to the previous experimental results, in which $\lambda_{SPP}$ is the wavelength of SPP and $\lambda_{k_0 NA}$ is the effective wavelength determined by the numerical aperture of the objective lens. We tried $a$ with different value and the calculation results are shown in Fig. 2.13, where the periodicities are coincident very well with the above experimental results. The visibility of the interference pattern is weak when $a$ is small and it gets higher when $a$ gets larger, which is the reason that there is no obvious "beat pattern" when there is no out-coupling grating or the grating is shallow.

Furthermore, we observed similar beat pattern by objectives with different NA. Different periodic patterns were observed with different objectives and the results are shown in Table 2.1, together with the theoretical analysis results. The analysis results are coincident well with the experimental ones, which proved the hypothesis above. That is, the strong background comes from the out-coupling grating interfere with propagating SPP and induce the beat pattern observed with LRM system.

In fact, Hohenau et al. also found similar beat pattern phenomenon with LRM system [27]. They had a good explanation for it with the background contribution. However, there was no other structures except the in-coupling hole array structures and the pattern was quite weak. It is known from above analysis that the

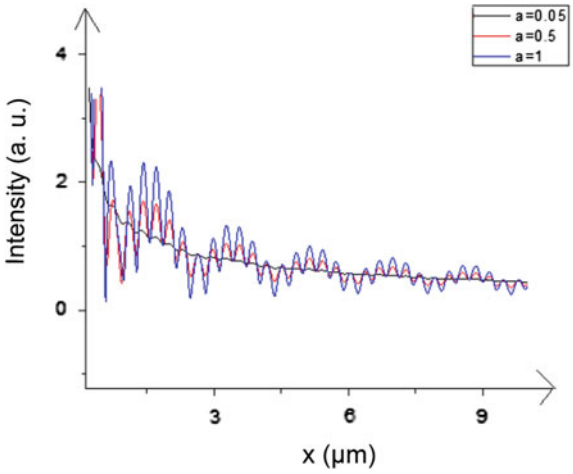


**Fig. 2.13** The beam pattern results under different background intensities

**Table 2.1** The periodicities observed with objectives with different NA

| NA | $\Lambda_s$(理论) (theory) | $\Lambda_s$(实验) (experiment) | $\Lambda_s$ (理论) (theory) | $\Lambda_s$ (实验) (experiment) |
|---|---|---|---|---|
| 1.40 | 0.260 | 0.26 | 1.747 | 1.87 |
| 1.32 | 0.268 | 0.27 | 2.242 | 2.39 |
| 1.25 | 0.277 | 0.28 | 2.982 | 3.19 |

background intensity $a$ is critical to the visibility of the beat pattern. It will be hard to observe the pattern if the background is too weak. In their experiment, the background comes from the scattering caused by the defect in the film, which is very weak. However, there will be plenty of out-coupling light when the out-coupling grating is introduced into the experiment. The grating is far from the imaging center so that one of the diffraction order will contribute to the background, which will induce an obvious beat pattern.

So far we explained and proved the reason for the two kind of fringes observed with LRM system. The phenomenon will exist in LRM system when observe the SPP or other waveguide system. A deep understanding will be helpful for better characterizing the phenomenon with LRM system.

## 2.3 The Propagation Control of SPP

SPPs are localized to a thin layer along metal/dielectric interface ($\sim$10 nm in metal and $\sim$100 nm in air in visible range), so it is a natural 2-dimentional subwavelength system and a promising carrier to the future integration optics. In the past decades, plenty of works in controlling SPP propagation were published and some SPP devices were realized, such as unidirectional coupling [28] and collimated coupling design for SPP [29], SPP focusing [30], demultiplexer [31, 32], Mach-Zehnder interferometer [33], and even the non-diffraction SPP Airy beam [34]. These researches make a deeper understanding to SPP and make SPP well prepared for the future application. In this section, we will discuss the basic control methods of SPP propagation.

### *2.3.1 In-plane Manipulation of SPP*

The manipulation methods in previous researches mentioned above are mainly rely on the coupling process. A typical example is shown in Fig. 2.14, a SPP is launched with a special structure and a phase distribution for the SPP is generated with the structure simultaneously so that a manipulation to the SPP is realized [32]. However, the future integrated photonic chips should be a compact 2-dimensional

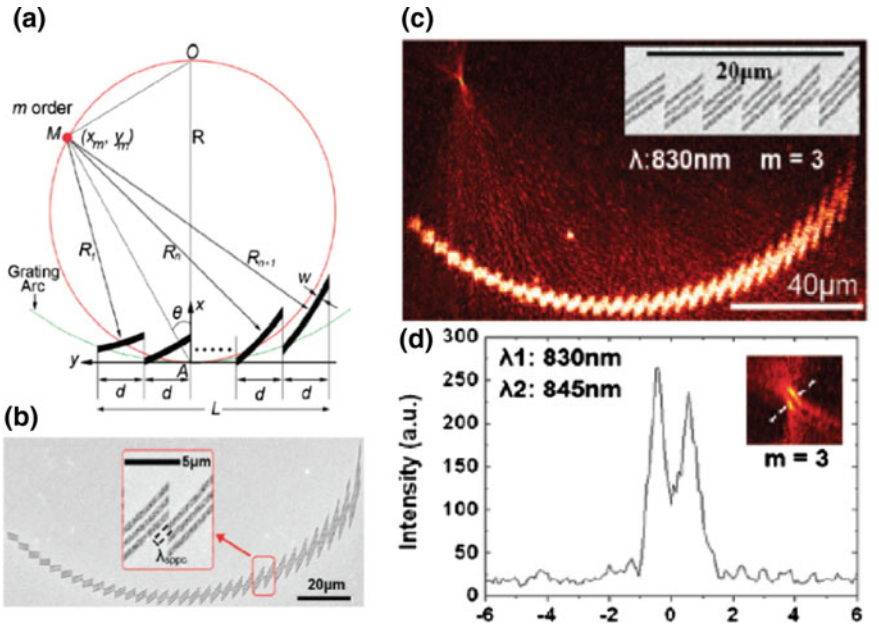


**Fig. 2.14** SPP focusing and demultiplexing realized with coupling process. Figure adapted with permission from Ref. [32], ACS

system as that in the integrated circuit, so that an in-plane manipulation is a more appreciated way rather than the out-plane control for the integrated photonics.

There are several works studied the in-plane SPP manipulation and realized some functions, such as SPP reflection, demultiplexing. The basic principle of in-plane SPP control is from Bragg's law [35]. The scheme is shown in Fig. 2.15, in

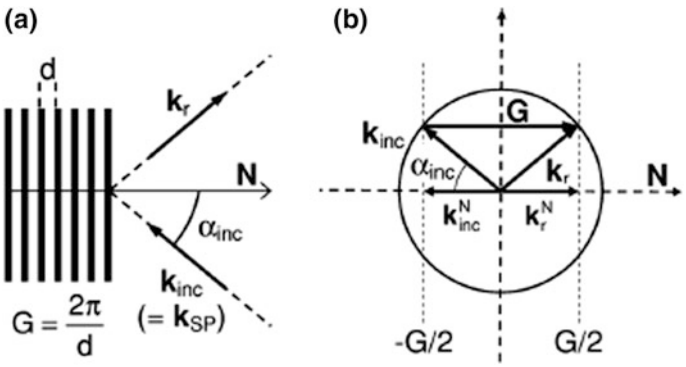


**Fig. 2.15** The principle of Bragg's reflection. Figure adapted with permission from Ref. [35], APS

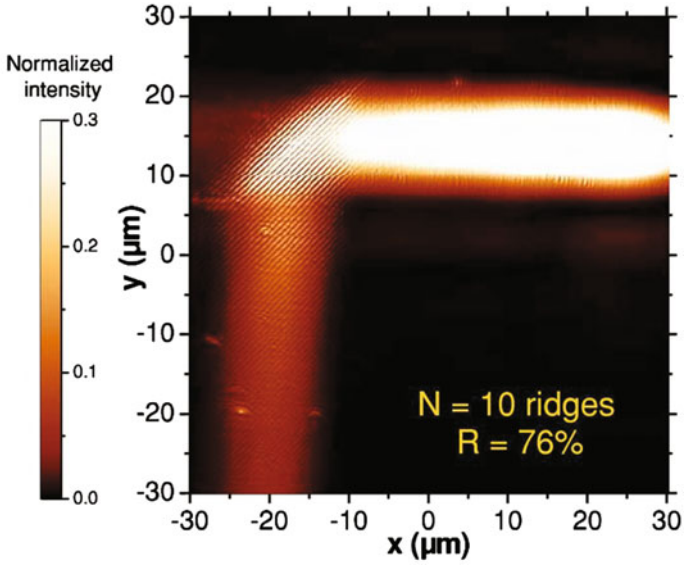


**Fig. 2.16** SPP reflection with Bragg grating observed with SNOM. Figure adapted with permission from Ref. [35], APS

which an incident SPP ($\overrightarrow{k_{inc}}$) is reflected to a new direction by a periodic grating and the wavevector becomes $\overrightarrow{k_r}$. The reciprocal vector $\overrightarrow{G}$ of the grating satisfy the expression of $\overrightarrow{G} = \overrightarrow{k_r} - \overrightarrow{k_{inc}}$, so that to match the momentum difference between the incident and the reflected SPP.

Figure 2.16 is a typical image for SPP reflection by a Bragg grating measured with NSOM. The incident SPPs propagate to the periodic grating from the right side and are reflected to the vertical direction. It is analog to reflect light with a mirror, so that the grating is called Bragg mirror. Figure 2.17 is the demultiplexing result demonstrated by Drezet group with the same principle [31]. A 2-dimensional hole array provide two different reciprocal vector $\overrightarrow{f_1}$ and $\overrightarrow{f_2}$, which match the difference between momentum of the incident SPP and the reflected SPP of 784 nm (red) and 730 nm (blue) accordingly. The SPP was reflected to two different direction by the match condition and realized the demultiplexing function.

With this principle, we realized the in-plane reflection of SPPs and measured the process with LRM system. Figure 2.18 is a typical in-plane reflection of SPP. The left panel is the design scheme of SPP reflection, in which the two dimensional dot array provides two reciprocal vectors with angle of 45° to horizontal direction as in the inset. The two reciprocal vectors match the momentum difference between the incident SPP and the reflected SPPs, in order to reflect the incident SPP to the left and right side to the array. In experiment, the structure was fabricated with FIB (focused ion beam, FEI). The in-coupling structure is grating as we used in previous

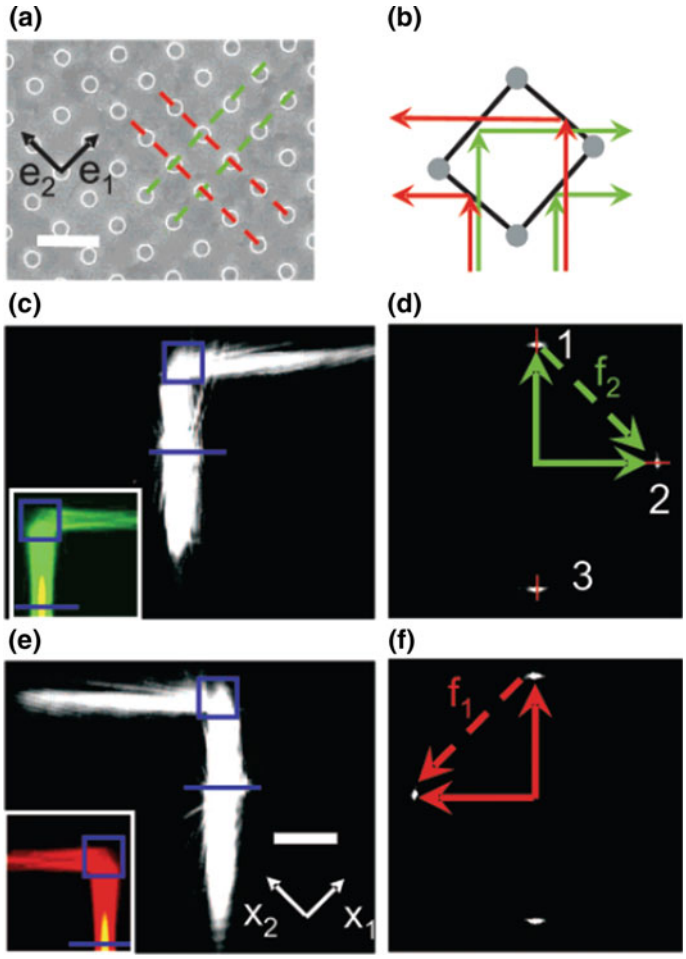


**Fig. 2.17** SPP demultiplexing with Bragg nanoarray. Figure adapted with permission from Ref. [31], ACS

experiment and the nanoarray is composed of nanocaves with diameter of 200 nm and depth of 20 nm. Figure 2.18b is the result observed with LRM system, in which we can see the left and right propagating SPPs which are the reflected part. Meanwhile, there is an up-propagating SPP as well, which is the transmitted SPP through the array. This structure can be taken as a SPP beam splitter, which splits the incident SPP to left, right and upside. The out-coupling gratings can be fabricated in these directions and couple the signals out. The splitting ratio of different component can be tuned by the parameters of the reflection array as well.

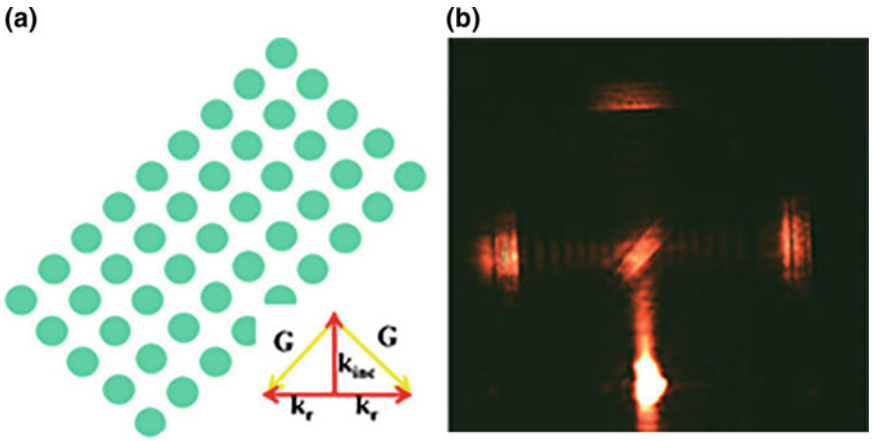


**Fig. 2.18** SPP reflection realized with 2D Bragg nanoarray. **a** The schematic of the refraction nanoarray. **b** SPPs reflection observed with LRM

This flexible in-plane splitter will have great application in the future signal processing, especially in quantum optics [36].

We realized some more complicated manipulation of SPP as well. Figure 2.19 is the experimental result of manipulating of SPP propagation with hexagonal lattice, where we made the reciprocal vector in ΓM direction to match the momentum difference between the incidence and the reflected SPP. Because of the symmetry of the lattice, the match condition of SPPs in six directions will get matched simultaneously (including the forward and reflected backward SPPs), so that to get

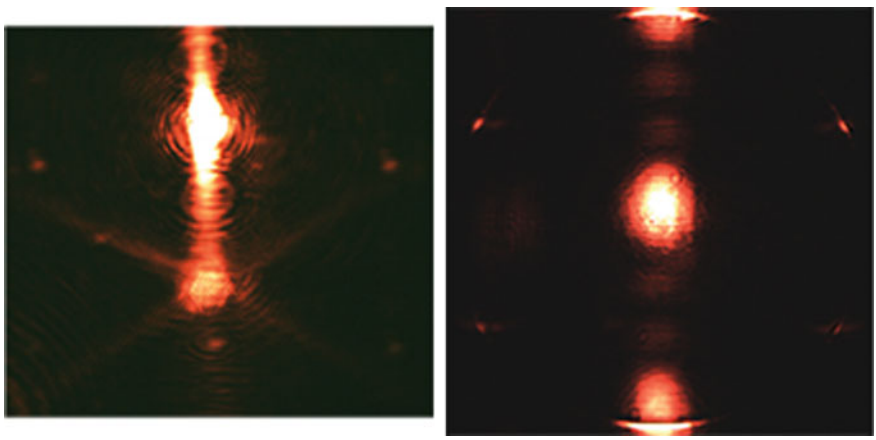

**Fig. 2.19** SPP reflection realized with hexagonal nanoarray in the real space (*left*) and the corresponding k-space (*right*)

reflected SPPs in the six directions. The left picture is the result in the real space, in which we can see SPPs in four different direction except for the forward and backward SPPs. The right picture is the result in the k-space, where we can see four smaller arcs as well as two larger ones, which corresponded to the SPPs in the four directions and the forward and backward SPPs in the left picture. The forward and backward arcs are larger because the SPPs reflected and transmitted by the array are mixed with the original SPPs coupled in by the grating, whose intensity is much stronger. It is clear that the Bragg's law in 2D SPP is not only effected in one direction, but can be effected for multiple directions, as long as the momentum mismatch between the incidence and the reflected SPPs can be compensated.

We completed a serial of design and measurement for SPP and realized some interesting functions as well. Next, we will introduce the measurement of the wavelength of SPP and the realization of SPP Mach-Zehnder (MZ) interferometer.

### *2.3.2 The Measurement of the Wavelength of SPP*

The wavelength of SPP is a critical parameter to design the coupling, manipulating structures. The coupling and reflection efficiency will related to the accuracy of the design wavelength of SPP. However, the wavelength of SPP will be different when the metal film is prepared with different method. A precise measurement for the wavelength will be a very helpful reference for the experiments.

We use the principle of Bragg reflection to measure the wavelength of SPP. Figure 2.20a is the principle scheme of Bragg reflection in the k-space, where the incident SPP is reflected by the help of the reciprocal vector $\mathbf{G_{1,1}}$. It will be easily to get that when the vertical component of $\mathbf{G_{1,1}}$ is equal to the wavevector of the SPP ($k_{SPP}$), the reflected SPP will be in the horizontal direction. The vertical period of the corresponding array will equal the wavelength of SPP. It is clear that the reflected SPP will be a small arc in the k-space from the previous discussion, which will be easily measured precisely.

We need to know the wavevector of incident SPP as the reference in this measurement. However it is not easy to get the wavevector very precisely from the previous result in the k-space. To solve this problem and measure the wavelength more precisely, we designed symmetrical nanoarrays with respect to the in-couple grating to reflect the SPP symmetrically. Then we can measure the angle between the two reflected SPP from the small arcs, without the request for the reference of the incident SPP. The upper and lower arcs will overlap with each other when the two nanoarray have the vertical period with the wavelength of the SPP.

The SEM image of the sample is shown in Fig. 2.20b. The nanoarray in both side of the grating have the same distance from the grating. The period in horizontal

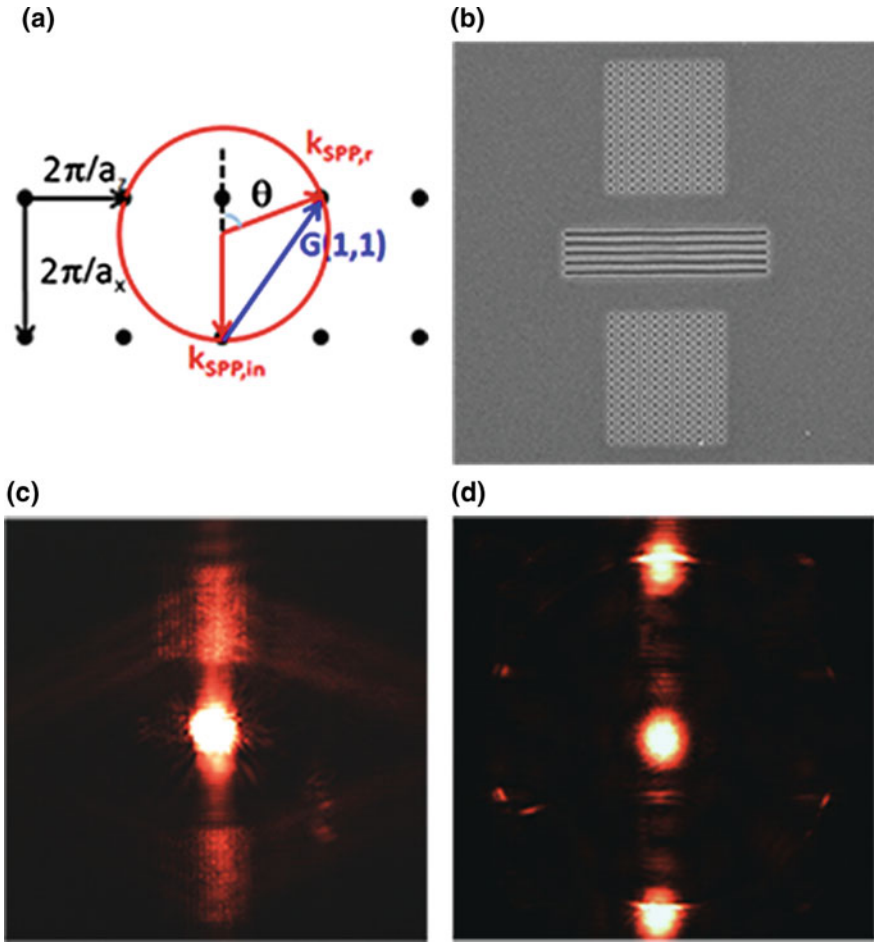


**Fig. 2.20** Measurement of the SPP wavelength with Bragg reflection. **a** The principle scheme of Bragg reflection in k-space. **b** The SEM image of the sample for symmetrical reflection (**c**, **d**). The reflection images observed with LRM in the real space (**c**) and k-space (**d**)

and vertical direction are 700 and 560 nm respectively. Here we still use a He-Ne laser with the wavelength of 632.8 nm as the source of SPP. Figure 2.20c is the result observed by LRM system in the real space, and Fig. 2.20d shows the corresponding result in the k-space, where the four small arcs are shown.

To measure the direction of the reflected SPPs, we connected the center of the arcs in two side separately and measure the angle between the two lines. The angle is twice of the reflected angle. We designed a serial of nanostructures with different vertical period with the step of 10 nm. The arcs of the design with 610 nm have the

best overlap result, which means the wavelength of SPP is close to 610 nm. A more precise wavelength can be deduced by the angles of the serial results. However, the precision is good enough for our experimental research for SPP later and we will use 610 nm as the wavelength of SPP when we use the laser of 633 nm and the film deposited with the same method.

### 2.3.3 SPP Mach-Zehnder Interferometer

Mach-Zehnder (MZ) interferometer is a widely used device to determine the relative phase shift variations between two collimated beams derived by splitting light from a single source. It is quite sensitive to the subtle change of refractive index. It is used to measure the phase difference between the two beams caused by a sample or a change in length of one of the paths. The device is frequently used in measurement of the temperature, density or pressure of fluid, gas, shock wave, heat transfer, and so on. MZ interferometer is a highly configurable and flexible device, so it always attracts great research enthusiasm, even in the field of quantum entanglement [37]. It is of great importance to realize MZ interferometer and control it in the field of SPP [33].

The key to the MZ interferometer is the precise splitting ratio and the relative phase difference between the two arms. They can be easily controlled by the design of the nanostructure for the splitter for the SPP as we discussed in the previous part. The SPP is coupled from 633 laser with grating as in the previous experiments and it will be split to upper and lower propagating SPPs evenly when the incidence illuminate to the center of the grating. The Bragg nanoarray is fabricated and used as reflectors for SPP in both side of the grating as in Fig. 2.20b. A grating is fabricated in the position where the SPPs meet each other at the right side of the in-coupling grating and performs as a splitter to realize about 1:1 split ratio for the SPPs from both side. It is a standard SPP MZ interferometer and the relative phase of the two arms can be changed by the position of the two nanoarray. The experimental results are shown in Fig. 2.21, in which Fig. 2.21a–c show the results with no relative phase difference and the relative phase difference of $\pm\pi/2$, respectively. The relative intensity after the splitter of the two arms are equal (Fig. 2.21a), or has a high ratio [only have the upper branch (Fig. 2.21b) or the lower branch (Fig. 2.21c)] with different relative phase, respectively. There's no structure at the left side of the in-coupling grating and we can see the interference pattern in the overlap area caused by the two reflected SPPs. It means that it is an easy way to control the relative position to control the relative phase difference of the MZ interferometer. Since SPP is a subwavelength system, the size of the SPP MZ interferometer can be further reduced, even shrink to less than 10 μm. It will have great importance to the future integration optics.

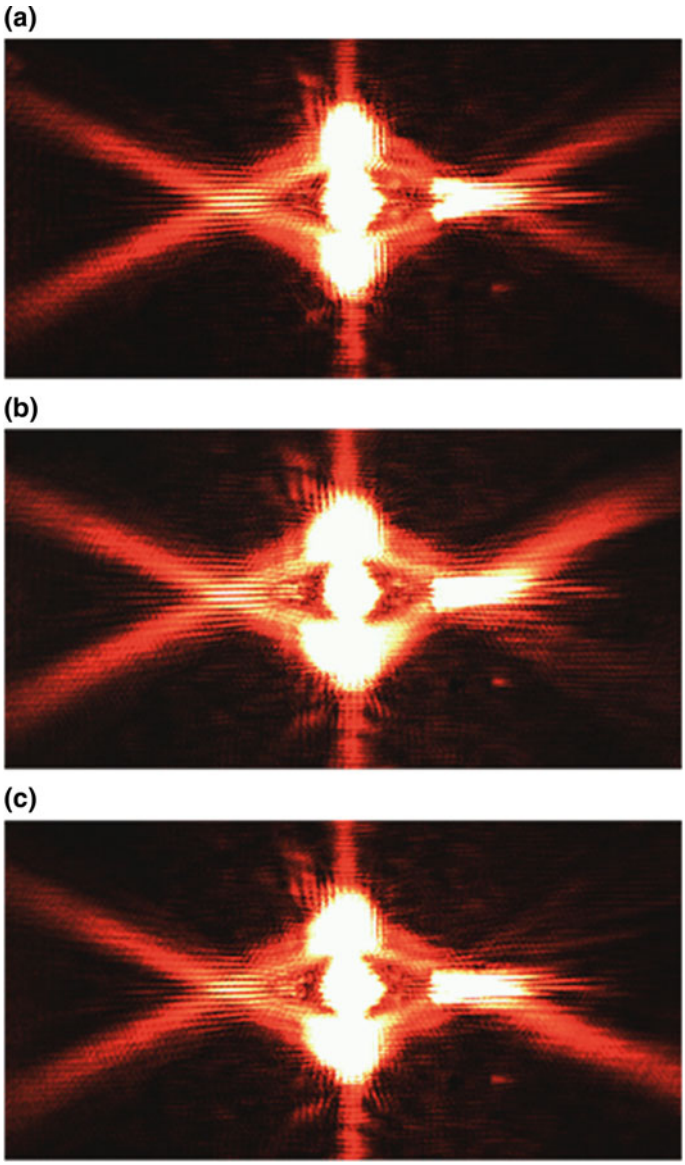


**Fig. 2.21** SPP MZ interferometer

## 2.4 Summary

In this chapter, the basic properties, the excitation and measurement methods of SPPs are introduced. The excitation of SPPs is successfully realized experimentally. We set up an LRM imaging system and observe the propagation of SPPs both in the

real space and in the reciprocal space (k-space). Some special phenomenon such as the beat pattern are successfully explained. Furthermore, some preliminary manipulations of SPPs are realized with Bragg's principle, such as reflection, MZ interferometer, which will have good applications in the integrated optics.

## References


1. Raether H (1988) Surface-plasmons on smooth and rough surfaces and on gratings. Springer Tr Mod Phys 111:1–133
2. Barnes WL, Dereux A, Ebbesen TW (2003) Surface plasmon subwavelength optics. Nature 424:824–830
3. Zia R, Schuller JA, Chandran A, Brongersma ML (2006) Plasmonics: the next chip-scale technology. Mater Today 9:20–27
4. Benson O (2011) Assembly of hybrid photonic architectures from nanophotonic constituents. Nature 480:193–199
5. Fano U (1936) Some theoretical considerations on anomalous diffraction gratings. Phys Rev 50:573
6. Fano U (1941) The theory of anomalous diffraction gratings and of quasi-stationary waves on metallic surfaces (Sommerfeld's waves). JOSA 31:213–222
7. Ferrell RA (1958) Predicted radiation of plasma oscillations in metal films. Phys Rev 111:1214–1222
8. 王振林 (2009) 表面等离激元研究新进展. 物理学进展 29:287–324
9. Zayats AV, Smolyaninov II, Maradudin AA (2005) Nano-optics of surface plasmon polaritons. Phys Rep 408:131–314
10. Burke J, Stegeman G, Tamir T (1986) Surface-polariton-like waves guided by thin, lossy metal films. Phys Rev B 33:5186
11. Tanaka K, Tanaka M (2003) Simulations of nanometric optical circuits based on surface plasmon polariton gap waveguide. Appl Phys Lett 82:1158–1160
12. Wang B, Wang GP (2004) Surface plasmon polariton propagation in nanoscale metal gap waveguides. Opt Lett 29:1992–1994
13. Bozhevolnyi SI, Volkov VS, Devaux E, Ebbesen TW (2005) Channel plasmon-polariton guiding by subwavelength metal grooves. Phys Rev Lett 95:046802
14. Maier SA, Kik PG, Atwater HA, Meltzer S, Harel E, Koel BE, Requicha AA (2003) Local detection of electromagnetic energy transport below the diffraction limit in metal nanoparticle plasmon waveguides. Nat Mater 2:229–232
15. Kretschmann E, Raether H (1968) Radiative decay of non radiative surface plasmons excited by light (Surface plasma waves excitation by light and decay into photons applied to nonradiative modes). Zeitschrift Fuer Naturforschung, Teil A 23:2135
16. Otto A (1968) Excitation of nonradiative surface plasma waves in silver by the method of frustrated total reflection. Zeitschrift für Physik 216:398–410
17. Hecht B, Bielefeldt H, Novotny L, Inouye Y, Pohl D (1996) Local excitation, scattering, and interference of surface plasmons. Phys Rev Lett 77:1889
18. Wang B, Aigouy L, Bourhis E, Gierak J, Hugonin J-P, Lalanne P (2009) Efficient generation of surface plasmon by single-nanoslit illumination under highly oblique incidence. Appl Phys Lett 94:011114
19. Hooper IR, Sambles JR (2002) Dispersion of surface plasmon polaritons on short-pitch metal gratings. Phys Rev B 65:165432
20. Courjon D, Bainier C (1994) Near field microscopy and near field optics. Rep Prog Phys 57:989

21. Liu Z, Steele JM, Lee H, Zhang X (2006) Tuning the focus of a plasmonic lens by the incident angle. Appl Phys Lett 88:171108
22. Drezet A, Hohenau A, Koller D, Stepanov A, Ditlbacher H, Steinberger B, Aussenegg FR, Leitner A, Krenn JR (2008) Leakage radiation microscopy of surface plasmon polaritons. Mater Sci Eng B-Adv 149:220–229
23. Bouhelier A, Huser T, Tamaru H, Guntherodt HJ, Pohl DW, Baida FI, Van Labeke D (2001) Plasmon optics of structured silver films. Phys Rev B 63:155404
24. Drezet A, Hohenau A, Stepanov AL, Ditlbacher H, Steinberger B, Galler N, Aussenegg FR, Leitner A, Krenn JR (2006) How to erase surface plasmon fringes. Appl Phys Lett 89:091117
25. Baudrion A-L, de Leon-Perez F, Mahboub O, Hohenau A, Ditlbacher H, Garcia-Vidal FJ, Dintinger J, Ebbesen TW, Martin-Moreno L, Krenn JR (2008) Coupling efficiency of light to surface plasmon polariton for single subwavelength holes in a gold film. Opt Express 16:3420–3429
26. Drezet A, Stepanov AL, Hohenau A, Steinberger B, Galler N, Ditlbacher H, Leitner A, Aussenegg FR, Krenn JR, Gonzalez MU, Weeber JC (2006) Surface plasmon interference fringes in back-reflection. Europhys Lett 74:693–698
27. Hohenau A, Krenn J, Drezet A, Mollet O, Huant S, Genet C, Stein B, Ebbesen T (2011) Surface plasmon leakage radiation microscopy at the diffraction limit. Opt Express 19: 25749–25762
28. Lopez-Tejeira F, Rodrigo SG, Martin-Moreno L, Garcia-Vidal FJ, Devaux E, Ebbesen TW, Krenn JR, Radko IP, Bozhevolnyi SI, Gonzalez MU, Weeber JC, Dereux A (2007) Efficient unidirectional nanoslit couplers for surface plasmons. Nat Phys 3:324–328
29. Laluet J-Y, Devaux E, Genet C, Ebbesen TW, Weeber J-C, Dereux A (2007) Optimization of surface plasmons launching from subwavelength hole arrays: modelling and experiments. Opt Express 15:3488–3495
30. Yin L, Vlasko-Vlasov VK, Pearson J, Hiller JM, Hua J, Welp U, Brown DE, Kimball CW (2005) Subwavelength focusing and guiding of surface plasmons. Nano Lett 5:1399–1402
31. Drezet A, Koller D, Hohenau A, Leitner A, Aussenegg FR, Krenn JR (2007) Plasmonic crystal demultiplexer and multiports. Nano Lett 7:1697–1700
32. Zhao CL, Zhang JS (2010) Plasmonic Demultiplexer and guiding. Acs Nano 4:6433–6438
33. Drezet A, Hohenau A, Stepanov AL, Ditlbacher H, Steinberger B, Aussenegg FR, Leitner A, Krenn JR (2006) Surface plasmon polariton Mach-Zehnder interferometer and oscillation fringes. Plasmonics 1:141–145
34. Minovich A, Klein AE, Janunts N, Pertsch T, Neshev DN, Kivshar YS (2011) Generation and near-field imaging of airy surface plasmons. Phys Rev Lett 107:116802
35. Gonzalez M, Weeber J-C, Baudrion A-L, Dereux A, Stepanov A, Krenn J, Devaux E, Ebbesen T (2006) Design, near-field characterization, and modeling of 45 surface-plasmon Bragg mirrors. Phys Rev B 73:155416
36. Wang SM, Cheng QQ, Gong YX, Xu P, Sun C, Li L, Li T, Zhu SN (2016) A 14 x 14 μm(2) footprint polarization-encoded quantum controlled-NOT gate based on hybrid waveguide. Nat Commun 7
37. Born M, Wolf E (1999) Principles of optics: electromagnetic theory of propagation, interference and diffraction of light. CUP Archive, Cambridge

# Chapter 3
# Non-perfectly-matched Bragg Diffraction and the Realization of Airy Plasmon

In recent years, non-diffraction beam became a hot research area, especially Airy beam [1, 2]. Except for non-diffraction, Airy beam has some other unique amazing properties, such as self-accelerating [2], ballistic dynamics [3], self-healing [4, 5], and so on. These unique properties will have a serial of possible applications, such as particle clearing [6], curved plasma channel [7], and so on. Intensive studies have been carried out on its novel properties and the potential applications, while the research enthusiasm to Airy beam still keeps growing. Since SPP is a probable candidate for the integration optics, it is of great importance to realize SPP Airy beam for manipulating the trajectory of SPP.

The Bragg's principle shows the importance in in-plane manipulation of the propagation of SPP. However, there is a great restriction with the principle which will limit the manipulations on plane wave, so that the functions realized with this principle are quite limited. In addition, the principle will limit the function to very narrow bandwidth as well. It will limit the applications in the all-optical integration with SPP. An alternative method must be proposed for the SPP manipulation. There is a principle called reciprocal lattice rod theory, which is well established in diffraction kinetics [8]. Based on the principle, a constructive diffraction will happen even when the Bragg's condition is not perfectly matched. This principle can be used in SPP as well. It can help to realize a nonlinear phase modulation, so that greatly improve the abilities of in-plane SPP manipulation.

In this chapter, we will first discuss a diffraction phenomenon called non-perfectly-matched (NPM) diffraction, which is based on the reciprocal lattice rod theory. By taking advantage of this NPM diffraction, the phase and amplitude of the SPPs can be manipulated. We then propose an in-plane nonlinear phase modulation method with this principle and successfully realize a plasmonic Airy beam, which reveals all the major properties of Airy beams.



L. Li, *Manipulation of Near Field Propagation and Far Field Radiation of Surface Plasmon Polariton*, Springer Theses,
DOI 10.1007/978-981-10-4663-6_3

## 3.1 Non-perfectly-matched Bragg Diffraction

### *3.1.1 Reciprocal Lattice Rod*

Reciprocal lattice rod is used in the kinetic theory of electron diffraction and X-ray diffraction [8, 9]. Since some realistic samples may have special shapes and limited size, the corresponding reciprocal lattice spots are not ideal dots, but elongated in some directions. The smaller the size is in the real space, the larger the size is in the reciprocal space. Usually, it will be hard to have the dot located exactly on the Ewald sphere to get the diffraction patterns if the reciprocal lattice spots are ideal dot. People usually prepare the samples into film so that the reciprocal spots will be elongated to rods (Fig. 3.1) in the direction perpendicular to the film. So that the rods will have much more possibility to intersect with the Ewald sphere. The electron diffraction will happen corresponding to the cross intensity when the high energy electron beam incident and the diffraction pattern can be observed.

There are some different types of samples that can generate diffraction pattern as well. The reciprocal spots will become reciprocal plate for the rod samples, and become reciprocal sphere for the powder samples. These enlarged reciprocal pattern will increase the opportunity for the intersection between the pattern and the Ewald sphere so that to get the diffraction pattern. The reciprocal rod, plate or sphere break the hard restriction of Bragg's law and increase the opportunity for the diffraction, pave a way for better research and understanding of materials' properties.

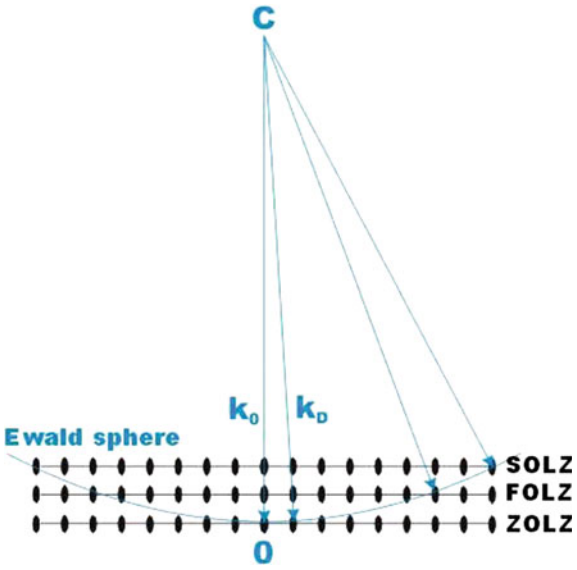


**Fig. 3.1** Reciprocal rod in electron diffraction

### 3.1.2 Non-perfectly-matched Bragg Diffraction in SPP

We want to break the restriction of Bragg's law in SPP system as well, so that to get more flexible and versatile manipulation of SPP system. Is it possible to realize it in SPP? The reciprocal rod, plate and sphere come from the limit size in certain dimension so that similar effects exist in SPP as well. SPP is a two dimensional system and we can limit the size of the structures in the two dimensions. However, if we shrink the size of the structure in both dimension, it will perform as a point defect and the SPP will be scattered to all direction evenly. It will not be helpful for the manipulation of SPP. As a result, we will just shrink the size in single dimension. Here we shrink the size of the nanoarray in the direction which is normal to the propagation direction of the incident SPP. In the extreme case, the array will be shrink to an one dimensional line. Certain diffraction will happen with the dot line. However, the efficiency will be quite low and it will limit the practical application. Meanwhile, it is hard to tune the amplitude distribution as well. As a result, a nanoarray with a limited width is more practical for real application.

We experimentally tested the scheme which is shown in Fig. 3.2a. An SPP wave propagates to a periodic nano-array and is diffracted to a new direction. Figure 3.2b is the corresponding lattice in the reciprocal space when the Bragg's law is matched, where the reciprocal spots lie on the Ewald sphere [10]. As a result, the incident SPP will be reflected to the direction with the angle of θ with respect to the horizontal direction by the reciprocal vector of $\mathbf{G_{-1,1}}$. In fact, the incident SPP has a limited width of about 2–4 μm, so that the nano-array which experiences the incident SPP is limited in the lateral direction and the corresponding reciprocal spots will be elongated to reciprocal rods along this direction, which are shown in Fig. 3.2c, d. In this situation, there are crosses between the reciprocal rods and the Ewald circle and there are corresponding diffractions determined by the reciprocal vectors of $\mathbf{G_{1,0}}$,$\mathbf{G_{2,0}}$, and so on, even when the reciprocal spots are not exactly on the Ewald circle.

In experiment, the same scheme were used as we discussed in Sect. 2.3.2. The SPP is coupled in by a grating with the light from a He–Ne laser. Two nano-arrays were fabricated in both side of the grating symmetrically to diffract the incident SPPs. The precise angle measurements were taken in the reciprocal space. We fabricated a serial of nano-array with the period in the horizontal direction of $P_z$ = 700 nm and the periods in the vertical direction are from 400 to 1100 nm. The Bragg's condition will not be matched in most of the diffraction arrays. Figure 3.3 shows the typical images observed with LRM system, in which Fig. 3.3a, c are the SPPs in the real space with the vertical period of $P_x$ = 390 nm (a) and 790 nm (c) respectively. There is some directional diffraction when the Bragg's condition is not perfectly matched. Figure 3.3b, d are the corresponding images in the reciprocal space, which are in good agreement with Fig. 3.2c and d, confirming our theoretical analysis. Moreover, for the sample of $P_x$ = 790 nm, a better matched condition is revealed for a higher ordered reciprocal vector $G_{-2,1}$ (shown in Figs. 3.2d and 3.3d), it consequently results in a stronger diffraction beam in this order, as shown in Fig. 3.3c. It also confirms our prediction of the intensity sacrifice from the mismatch. By carefully measure the diffraction angles of all samples in their reciprocal

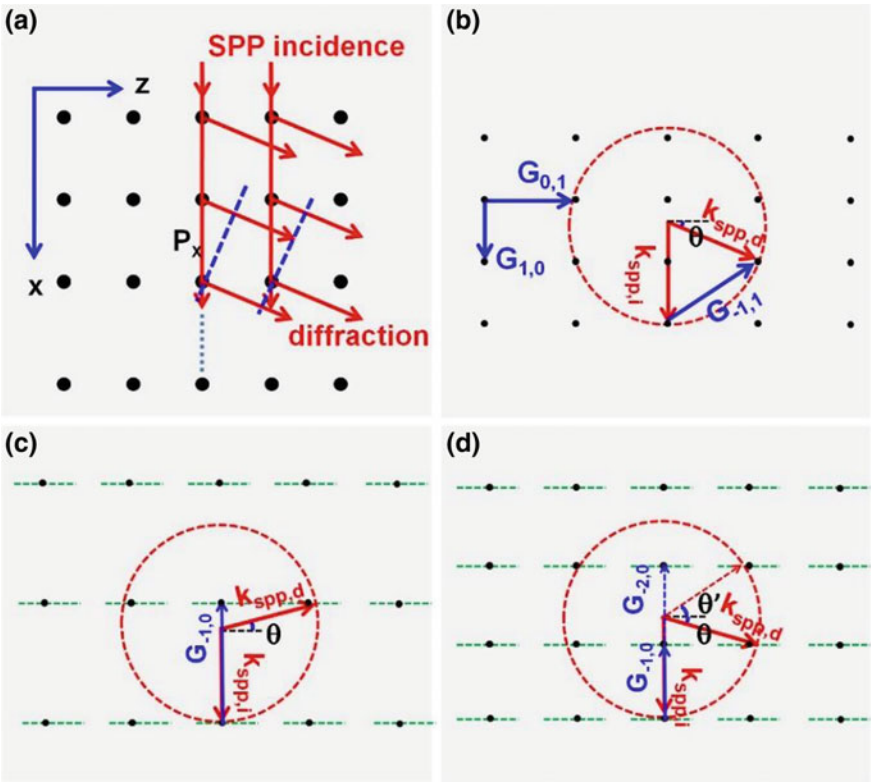


**Fig. 3.2** Non-perfectly-match diffraction. **a** Scheme of SPP diffraction by periodic array. **b** The situation in k-space when Bragg's condition is perfectly matched. **c**–**d** The situations when Bragg's condition is not perfectly matched in the case of the 1st order (**c**) and the 1st and the 2nd order diffraction. Figure adapted with permission from Ref. [10], APS

space, we obtained the whole experimental data, which are in extremely good agreement with the calculated ones from Eq. (3.2) as shown in Fig. 3.4. It proved our hypothesis about the diffraction. That is the diffraction will exist even when the Bragg's condition is not perfectly matched in our experiment system and the diffraction angle is determined by the period of the vertical direction. We call this principle as non-perfectly-matched Bragg diffraction.

### *3.1.3 The Amplitude of Non-perfectly-matched Bragg Diffraction*

There is another conclusion that the amplitude of the diffraction are different from the nano-array with different period from above experiments, which is clearer from the results in the reciprocal space. It is due to the different intensities at the intersections of the reciprocal rods and the Ewald circle. We performed Fourier

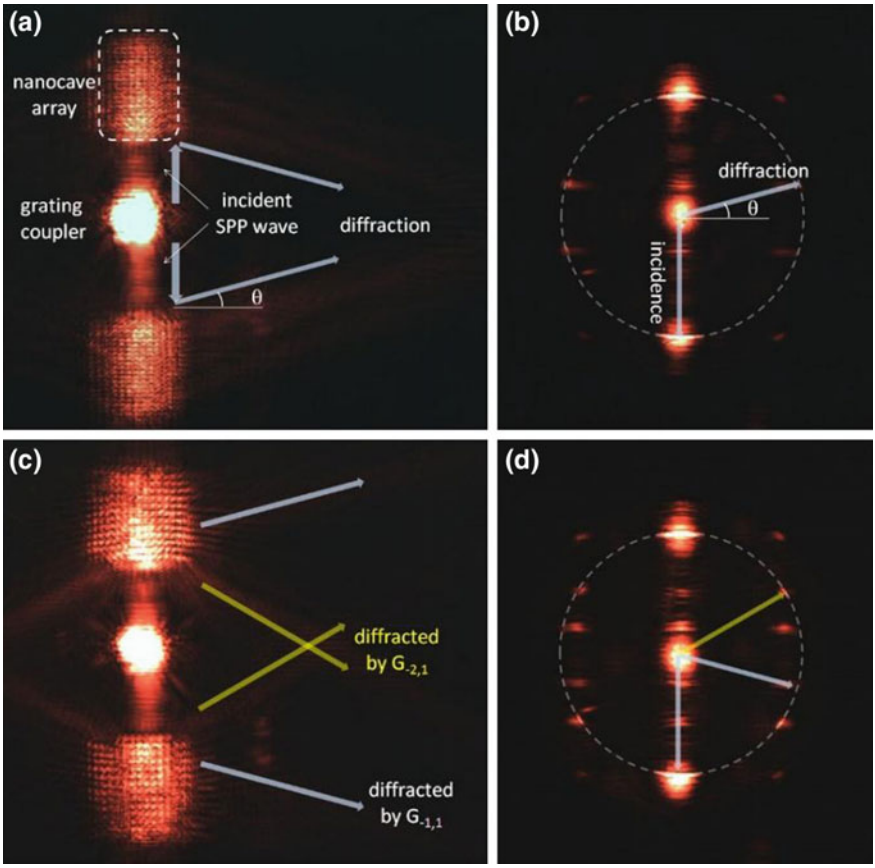


**Fig. 3.3** SPP diffraction under non-perfectly-matched Bragg's condition. **a**, **c** SPP propagation in real space, **b**, **d** corresponding images in the reciprocal space. Figure adapted with permission from Ref. [10], APS

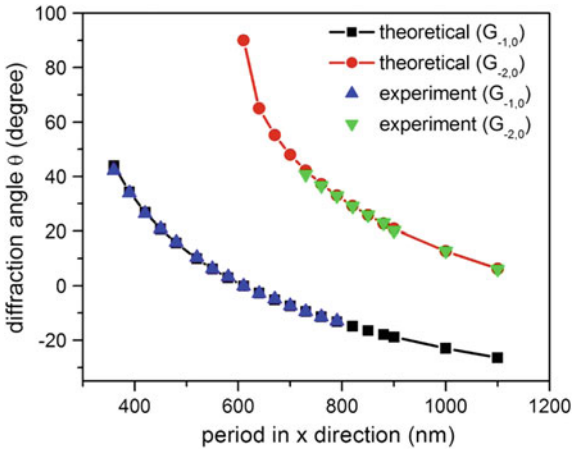


**Fig. 3.4** SPP diffracted directions under diffracted arrays with different periods. Figure adapted with permission from Ref. [10], APS

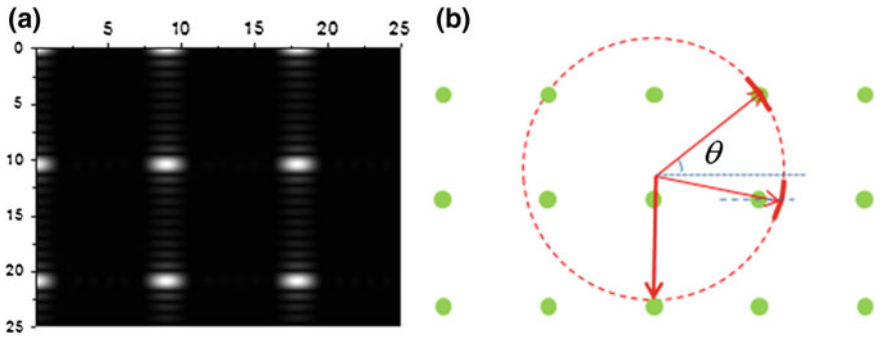


**Fig. 3.5** **a** Fourier transformation result for finite array. **b** The corresponding situation in the k-space

transformation to an array with limited size, in which the period in the horizontal direction is px = 700 nm and that in the vertical direction is py = 600 nm. The number of the periods are 7 × 15 in horizontal and vertical direction, respectively. The transformed result is shown in Fig. 3.5a, where the reciprocal spots are not ideal dots but elongated to rods. The intersection between the rods and the Ewald sphere are not dots but arcs, which are shown in Fig. 3.5b. As a result, the diffracted SPPs in the reciprocal space are arcs in the experiments as shown in Fig. 3.3. The intensity distributions on the arcs determined the amplitudes of the diffractions. Figure 3.6 shows the relation between the diffraction intensity and the period of the vertical direction, where the period in the horizontal direction is still 700 nm and the periods in the vertical direction varying from 360 to 1000 nm. The red and blue dots are the highest intensities of the arcs in the reciprocal space for the 1st and 2nd order diffraction from the experiments, respectively, while the black and green dots are the corresponding calculated intensities with Fourier transformation. The experimental results are well coincident with the calculated results, which indicate that the diffraction amplitude can be estimated by the calculation with Fourier transformation.

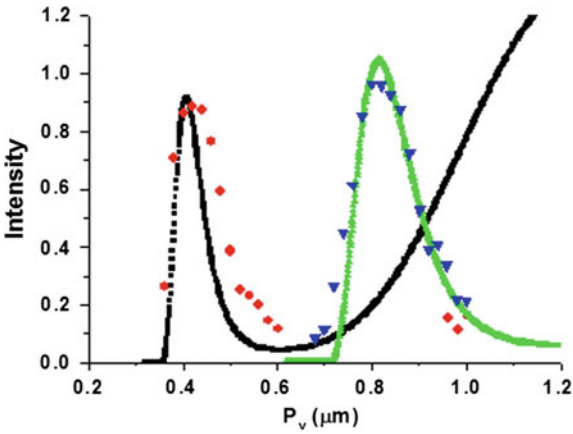


**Fig. 3.6** Diffracion intensity under arrays with different period. The *red* and *blue dots* are the highest intensities of the arcs in the k-space for the 1st and 2nd order diffraction from the experiments, while the *black* and *green dots* are the corresponding calculated intensities with Fourier transformation

There are a lot of beams or optical manipulation request special amplitude distributions, (e.g. Airy beam request an amplitude distribution of $x^{-1/4}$). It is hard to realize the amplitude distribution with Bragg's principle. However, it is possible to change the period of the corresponding structure so that to manipulate the amplitude distribution. This method provide more flexible in-plane manipulation to SPP.

There is no doubt that there are other methods to tune the diffraction amplitude, such as change the depth, shape, size of the unit nanostructure [11]. These parameters will change the reciprocal lattice and change the diffraction amplitude. However, it will be hard to have a good control of them with current fabrication method. Further research and optimization for these parameters will be performed in practical application in the future.

In summary, a constructive SPP diffraction still exists on the condition that the Bragg's condition is not perfectly matched. The diffraction direction is determined by the period of the structure in the propagation direction of the incident SPP in our system. It provides a good opportunity for more flexible tuning of SPP, which is to tune the phase of the SPP with the vertical period of the structure and to tune the amplitude with the horizontal period. This new method open up a new avenue in planar photonic modulations and integrations. We will further study this method in the following sections.

## 3.2 Generation of SPP Airy Beam

Diffraction is a nature of any wave [12]. In nature, waves with limited energy will spread due to the diffraction, e.g. a Gaussian beam will gradually spread after its waist. The diffraction nature of light limits the delivery of the energy or information in free space. Researchers try to suppress the diffraction of beams, even in a certain range. In 1987, Durnin et al. realized Bessel beam, which is the first realization of a non-diffractive beam [13]. The research enthusiasm to non-diffractive beams was light up and several similar non-diffractive beam were realized and studied, as well as a lot of practical applications in biological, nonlinear optics, optical manipulation, and so on. Meanwhile, Berry and Balazs predict a different non-diffractive beam, Airy beam in 1979. Airy beam is the only nontrivial 1D solution for a wave propagation maintaining the non-spreading property, which was deduced from Schrödinger equation in quantum mechanics for a free particle[9]. Airy beam is a novel beam with properties of self-accelerating or self-bending [14], self-healing as well as non-diffraction. However, due to the complex phase and amplitude requirement, it was not observed until 2007 [1]. The special beam provide us an opportunity to control the delivery path of the energy of optics in free space. As a result, since its recent observation in optics, intensive studies have been carried out on its novel properties, such as self-accelerating, ballistic dynamics, self-healing [2–5, 15], as well as the recent nonlinear generation [16] and possible applications [6, 17, 18] (e.g., particle clearing, curved plasma channel). Some new methods were proposed to generate Airy beam, even in electron [19] and plasmon [7] systems.

### 3.2.1 Airy Beam and Its Realization

In 1979, Berry and Balazs proposed a beam which can be non-diffractive, self-accelerating inspired by solving Schrödinger equation in quantum mechanics for a free particle, which is Airy beam [14]. Actually, Airy beam can be deduced from Helmholtz equation. In Helmholtz equation

$$\nabla^2 u + k^2 u = 0 \tag{3.1}$$

where assume $u(x, y, z) = \phi(x, y, z)\mathrm{e}^{ikz}$. A proximate Helmholtz equation under paraxial condition can be deduced by neglecting the high order items as Eq. 3.2

$$\frac{\partial^2 \phi}{\partial x^2} + \frac{\partial^2 \phi}{\partial y^2} + 2ik\frac{\partial \phi}{\partial z} = 0 \tag{3.2}$$

Assuming a 2 dimensional system where the field in y direction is homogeneous, Eq. 3.2 will be reduced to:

$$\frac{\partial^2 \phi}{\partial x^2} + 2ik\frac{\partial \phi}{\partial z} = 0 \tag{3.3}$$

It is analog the Schrodinger equation $-\frac{\hbar^2}{2m}\frac{\partial^2 \psi}{\partial x^2} = i\hbar\frac{\partial \psi}{\partial t}$ for the free particle's movement. Both of the two equations have the form of Airy equation:

$$y'' - xy = 0 \tag{3.4}$$

The solution of Airy equation is $y = C_1 Ai(x) + C_2 Bi(x)$, in which

$$Ai(x) = \frac{1}{\pi}\int_0^\infty \cos\left(\frac{t^3}{3} + xt\right)dt$$

$$Bi(x) = \frac{1}{\pi}\int_0^\infty \left[\exp\left(-\frac{t^3}{3} + xt\right) + \sin\left(\frac{t^3}{3} + xt\right)\right]dt$$

$Bi(x)$ is not convergent. People usually consider the solution of $y = Ai(x)$. Make $\phi = Ai(f_1)\exp(f_2)$, in which $f_1$ and $f_2$ are functions of x, z. Then we can deduce the form of $\frac{\partial \phi}{\partial z}, \frac{\partial^2 \phi}{\partial x^2}$ and put them into Eq. 3.3. Meanwhile, $Ai''(x) = xAi(x)$. By comparing the coefficients of corresponding items of the equations, we can have the following equations:

$$\begin{cases} \frac{\partial^2 f_1}{\partial x^2} + 2\frac{\partial f_1}{\partial x}\frac{\partial f_2}{\partial x} = -2ik\frac{\partial f_1}{\partial z} \\ \left(\frac{\partial f_2}{\partial x}\right)^2 + \frac{\partial^2 f_2}{\partial x^2} + f_1\left(\frac{\partial f_1}{\partial x}\right)^2 = -2ik\frac{\partial f_2}{\partial z} \end{cases} \tag{3.5}$$

To get a diffraction free solution, of which the wave packet keeps the same when propagating along z-direction, $f_1 = ax + f_3(z)$ need to be satisfied, in which $f_3$ is a function of z. After plugging the equation into the Eq. 3.5 and considering the initial conditions, we can get the solutions:

$$f_1(x,z) = ax - \frac{a^4 z^2}{4k^2}, \tag{3.6}$$

$$f_2(x,z) = i\frac{a^6 z^3}{12k^3} - i\frac{a^3 xz}{2k}, \tag{3.7}$$

$$f_3(z) = -\frac{a^4}{4k^2} z^2. \tag{3.8}$$

Plug these solutions into $\phi$, and

$$\phi(x,z) = Ai\left(ax - \frac{a^4 z^2}{4k^2}\right) \exp\left(i\frac{a^6 z^3}{12k^3} - i\frac{a^3 xz}{2k}\right) \tag{3.9}$$

It is the nondiffraction Airy beam, in which

$$Ai(x) \sim \begin{cases} \frac{1}{2\sqrt{\pi} x^{\frac{1}{4}}} \exp\left(-\frac{2}{3} x^{\frac{3}{2}}\right) & (x > 0) \\ \frac{1}{\sqrt{\pi}(-x)^{\frac{1}{4}}} \sin\left[\frac{2}{3}(-x)^{\frac{3}{2}} + \frac{\pi}{4}\right] & (x < 0) \end{cases} \tag{3.10}$$

Figure 3.7 is the intensity of Airy beam when it propagating in free space, in which s and $\xi$ are the reduced coordinates in the start and propagating direction. The inset is the intensity at the start plane with $\xi = 0$. The shape of the wave packet doesn't change along $\xi$. The trajectory of the main lobe is a parabolic trajectory and it is self-bended, or we call it self-accelerating.

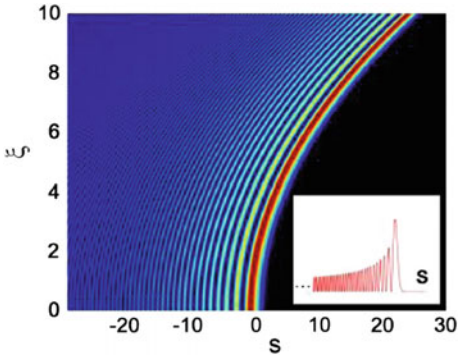


**Fig. 3.7** Airy beam in free space. Figure adapted with permission from Ref. [1], APS

At the start plane,

$$\begin{aligned}\phi_0(x) &\approx \left(-\pi^2 x\right)^{-1/4}\sin\left[2/3(-x)^{3/2}+\pi/4\right] \\ &= A_0^+ \exp(ik\psi_o^+) + A_0^- \exp(ik\psi_o^-) \\ &= \phi_0^+(x) + \phi_0^-(x)\end{aligned} \tag{3.11}$$

In which $k\psi_o^{\pm}(x) = \mp\left[2/3(-x)^{3/2}+\pi/4\right]$, $A_0^{\pm}(x) = \pm(i/2)(-\pi^2 x)^{-1/4}$. From ray optics, the rays emerging from $\phi_0^-(x)$ will propagate to the left, while the rays emerging from $\phi_0^+(x)$ will propagate to the right (SB+) and converging to a caustic along the curving main beam trajectory as shown in Fig. 3.8[20]. The Airy beam is a caustic beam, which is comprised by a serial of rays in different direction. The rays are mainly come from $\phi_0^+(x)$.

Although Airy beam was proposed theoretically in 1970s, it was first observed experimentally in 2007 since its complicate form. Siviloglou et al. made a Fourier transformation to Eq. 3.9

$$\Phi(k) \propto \exp(-ak^2)\exp(ik^3/3) \tag{3.12}$$

which is clearer and it means applying a cubic phase to a Gaussian beam. In experiment, a spatial light modulator (SLM) was used to generate the cubic phase for Gaussian beam and realized Airy beam in real space by applying Fourier transformation by a lens to the beam from the SLM. Figure 3.9a, b are the gray map of SLM to generate 1 and 2-dimensional cubic phase. The experiment set up is schematically shown in Fig. 3.9c. An ideal nondiffraction beam requires infinite start plane and energy so that to compensate the diffraction. However, it is

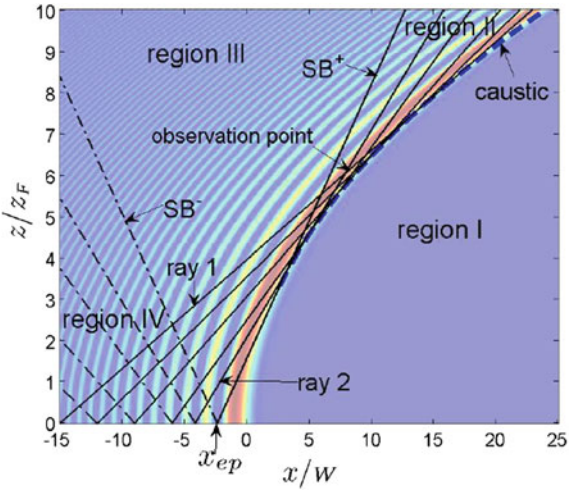


**Fig. 3.8** Caustic scheme of Airy beam. Figure adapted with permission from Ref. [20], OSA

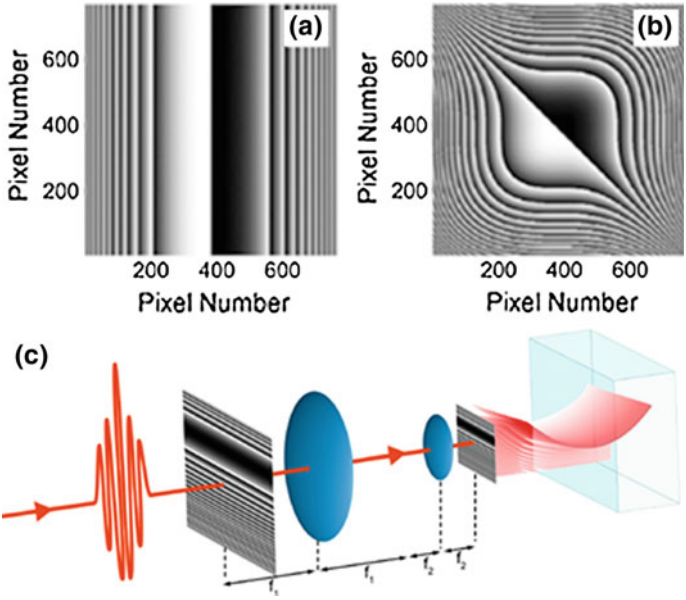


**Fig. 3.9** Generation of Airy beam with SLM. **a**, **b** Phase profile of SLM with cubic phase in 1D (**a**) and 2D space (**b**). **c** scheme of Airy beam generation with SLM in free space

impossible to make it in real world and all the nondiffracted beams are generated in finite range, including the Bessel beam. The Airy beam realized in above works are also finite nondiffraction beams.

### *3.2.2 Airy Beam Realization on Metal Surface*

Airy beam provides a new avenue to manipulate the energy and information of light because the special properties such as nondiffraction, self-bending and self-healing. However, the previous realizations of Airy beam were in 3-dimensional free space. More interesting physics and applications will be explored if we can realize Airy beam in 2D SPP system. Salandrino et al. theoretically predicted the possibility of SPP Airy beam [21]. However, the conventional scheme to generate Airy beam is hard to be performed in 2D system. An SLM will be required to generate a cubic phase for a Gaussian beam and a lens will be required for the inverse Fourier transformation to get Airy beam in real space. The SLM and lens are hard to be realized in the metal surface. An alternative way is to couple an Airy beam generated in free space into SPP. However, there're some problems, and a good coupling result is hard to get as well.

A 1.5 power phase for the start plane is a key to generate Airy beam from the analysis in Sect. 3.2.1 [20, 22]. We proposed a method for nonlinear phase

modulation based on non-perfectly-matched Bragg's condition as discussed in Sect. 3.1. The intensity distribution could be controlled with this method as well. Is it possible to generate a 1.5 power phase with a non-periodic lattice, so that to generate Airy beam in 2D system? We tried this and proved the possibility.

First of all, we experimentally proved the hypothesis of nonlinear phase modulation with non-perfectly-match diffraction with non-periodic array. The non-periodic nano-array is periodic in z-direction, while it is gradient in x-direction (the gradient is $\Delta$ = 10 nm). Figure 3.10a is the SEM image of the graded nano-array fabricated with FIB. The non-perfectly-match diffraction is expected to be still effective in this small gradient case. A laser light from a He–Ne laser ($\lambda$ = 632.8 nm in free space) was used as the source of SPP and we measured the result with LRM system. Figure 3.10b is the experimental result, where a self-bending, non-spreading beam is shown. A theoretical calculation was performed based on Huygens-Fresnel principle. Every nano-hole was considered as a point source and the total field will be the integration of the field from each point source [23, 24]. The theoretical result is shown in Fig. 3.10c, which coincident very well with the experimental result. To make a quantitative evaluation on the experimentally achieved self-bending beam, profiles at different propagation distances (marked with white dash lines in Fig. 3.10b) are plotted in Fig. 3.10d, from which a set of Airy-like wave profile are clearly manifested. The main lob keeps at a narrow width of about 1.3 μm, showing non-spreading property in a propagation range of 30 μm, which is long enough for an SPP wave at the wavelength of 632.8 nm. The decay speed is much less than that of normal SPP. In this regard, it behaves like a lateral confined in-plane waveguide and suggests possible applications in guiding SPP waves.

To further analyze the Airy-like beam achieved by non-periodic array, we deduced the phase evaluation of the graded array. The phase evaluation in x-direction can be obtained with non-perfectly-match principle, that is, an extra

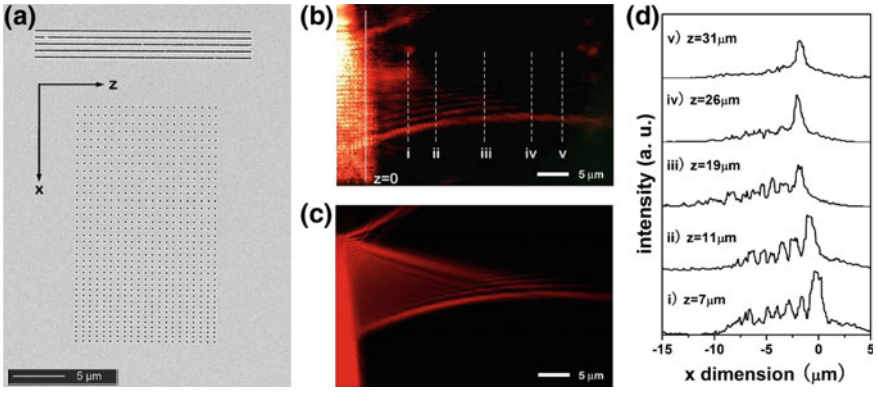


**Fig. 3.10** Generation SPP Airy beam with graded nano-array on metal surface. **a** SEM image of the fabricated sample, **b** The experimental result observed with LRM and **c** The corresponding calculation result, **d** The profiles of the beams at the corresponding locations marked with *white dash line* in **b**. Figure adapted with permission from Ref. [10], APS

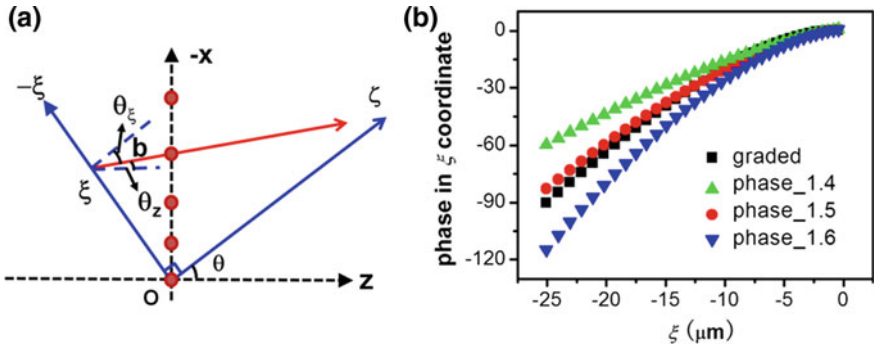


**Fig. 3.11** **a** Scheme of the phase transformation from the x axis to a virtue ξ axis, which can be designed with respect to the beaming angle θ for the main branch of SPP Airy beam. **b** Deduced phase distributions in the starting ξ axis together with the 1.4, 1.5, 1.6-power phase modulations. Figure adapted with permission from Ref. [10], APS

phase change of $2\pi$ from every local lattice is yielded. The phase for the diffracted beam at the $m$th row is $\phi(x) = \phi_0 + k_{spp}x + 2\ m\pi$, in which $\phi_0$ is an arbitrary reference. There is an angle of $\theta$ ($\theta \sim 20°$) between the main lob and $z$-axis, which means the lattice boundary (line $z = 0$) is not the start line of this SPP Airy beam. The phase evaluation along x-direction can be deduced to the direction of the start plane of Airy beam in $\xi$-axis, which is normal to the tangent of trajectory of the main lob of Airy beam as shown in Fig. 3.11a.

$$\phi(\xi) = \phi(x) - k_{spp}b = 2m\pi + k_{spp}x - k_{spp}b, \tag{3.13}$$

In which

$$b = -\frac{x\tan(\theta_0)}{\cos(\theta_x) + \tan(\theta_0)\sin(\theta_x)}, \quad \xi = \frac{x}{\cos(\theta_0)(1 + \tan(\theta_x)\tan(\theta_0))}, \tag{3.14}$$

$$\sin(\theta_0) = \frac{\lambda_{spp} - a_0}{a_0}, \quad \sin(\theta_x) = \frac{\lambda_{spp} - a_x}{a_x} \tag{3.15}$$

In which $a_x$ is defined as the local lattice determined by the mean value of two distances before and after the lattice of $x$. According to the experimental results of the position of original point of $O$ ($a_0 \sim 450$ nm) and initial angle ($\theta \sim 20°$), we calculated the transformed phase $\phi(\xi)$ shown in Fig. 3.11b together with the results of 1.4, 1.5, and 1.6-power phase modulation. It is clearly seen that the deduced data from the graded array matches the 1.5 power relation considerably well. It well explains the outcome of Airy-like SPP beam. In addition, the intensity of diffraction from every local lattice is dominated by the matching condition, i.e., the better Bragg's condition satisfied, the stronger diffraction formed. Thus, the location of the main lobe is usually near the match point, which is in coincidence with the Airy function. Unfortunately, the precise modulation of intensity for this graded case is

rather complicated and remains a problem to be further explored. Nevertheless, at this moment we mainly study the phase modulation, which is considered as the critical factor to achieve the Airy beam.

It is proved that the non-perfectly-matched diffraction is still effective in non-periodic array in above result, so that a nonlinear phase modulation can be achieved with a non-periodic array. Next we will get further understanding of this phase modulation method. More precise and versatile Airy beam generation will be achieved with the method.

Figure 3.12 is the scheme of the realization of Airy beam with our nonlinear phase modulation method, in which a groove grating is used to couple a He–Ne laser beam (632.8 nm) into an in-plane propagating SPP wave, which subsequently incidents into a non-periodically arranged nanocave array. By appropriate arrangement, diffracted SPP waves from nanocaves will interfere and ultimately form two SPP Airy beams on both sides. The inset is the Airy beam we realized in above experiment.

Based on the analysis above, SPP Airy beam with a defined beaming direction (for the main lobe) can be generated by a proper non-periodic array. With a beaming angle of $\theta$, the corresponding phase along the $x$ axis is retrieved as

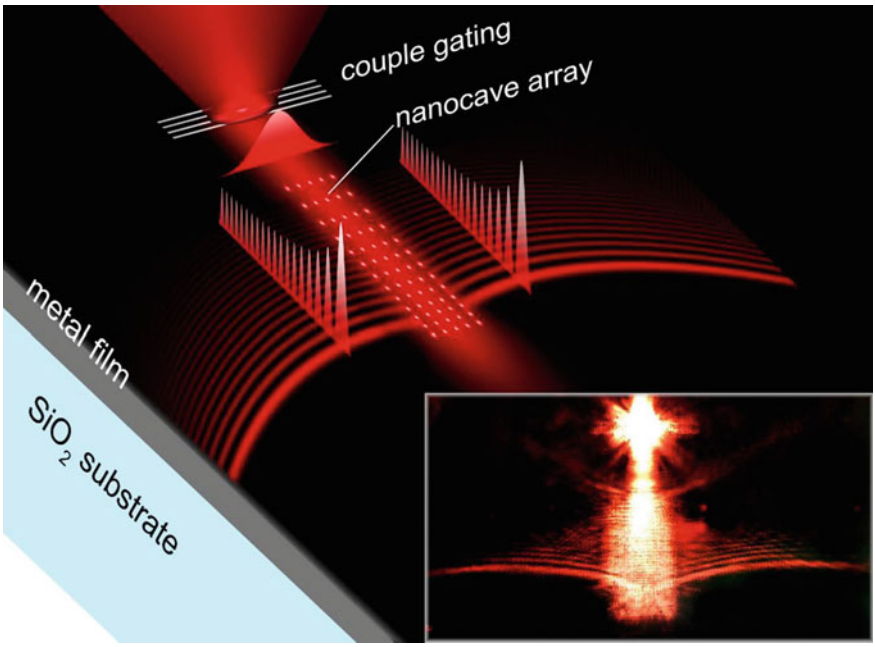


**Fig. 3.12** Scheme of Airy beam generation with non-periodic nano-array. Figure adapted with permission from Ref. [10], APS

$$\psi(x) = -\frac{2}{3}\left(-\frac{\xi}{\xi_0}\right)^{3/2} - \frac{\pi}{4} - k\frac{\xi \sin\theta}{\cos(\theta - \theta_\xi)}, \tag{3.16}$$

where $x = \xi\cos(\theta) + \xi\sin(\theta)\tan(\theta - \theta_\xi)$, $\theta_\xi = \arcsin(\partial_\xi \phi(\xi))$, and $\xi_0$ is a constant determines the acceleration of Airy beam. According to the equivalent phase by diffraction $\phi_m(x) = kx + 2m\pi$, we can deduce the location of the $m$th diffraction unit by solving $\phi_m(x) = \psi(x)$, and ultimately retrieve the arrangement of nanocave array. Figure 3.13a, b are the designed array data and calculated results of the SPP Airy beam with the angle of $\theta = 0$ and $-7°$, respectively. The corresponding

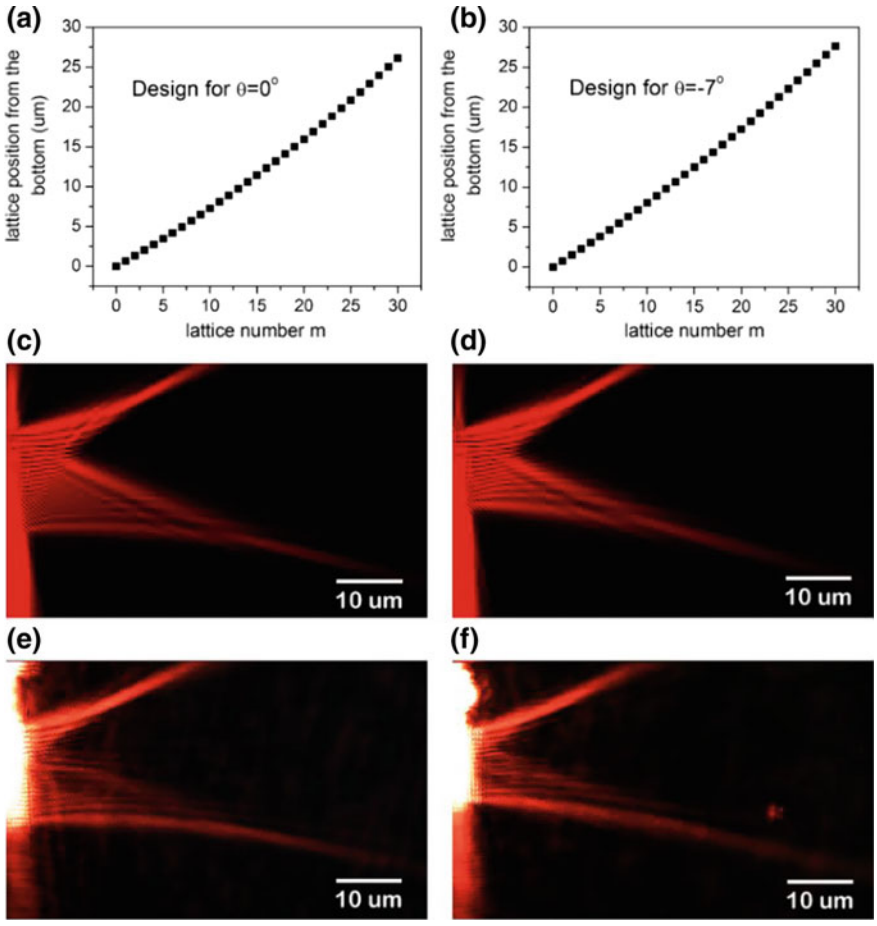


**Fig. 3.13** Designable generation of SPP Airy beam. **a**, **b** Designed non-periodic lattice in x-dimension (scaled with respect to the *bottom* of the array) for **a** horizontal beaming θ = 0° with Pz = 640 nm, $\xi_0$ = 1.08 and **b** down-inclined beaming θ = −7° with Pz = 650 nm, $\xi_0$ = 1.33. **c**, **d** Calculated results and **e**, **f** Experimental results respectively. Figure adapted with permission from Ref. [10], APS

experimental results are subsequently shown in Fig. 3.13e, f, which agree well with the calculated ones. By carefully examining these beaming profiles, a set of upper branches with considerable strong intensities are exhibited besides Airy beam features revealed in main parts. It is actually due to another matched condition corresponding to the reciprocal $G_{-2,1}$ in the larger $a_x$ region. So far, of importance is that SPP Airy beams are realized in a designable way by proper phase modulation, where the non-spreading, self-bending properties are well demonstrated. As for the precise intensity modulation, we believe it may be improved by carefully tuning the diffraction elements. The achieved SPP Airy beam further proved the efficient of the nonlinear phase modulation method.

### 3.2.3 *Characteristics of Plasmonic Airy Beam*

We analyzed the characteristics for the achieved plasmonic Airy beam with the angle of $\theta = 0°$. First of all we examined the nondiffraction property, with which the width of the main lob will keep the same. Figure 3.14a is the measured result of the width of the main lob in Fig. 3.13e, in which the width is kept in around 1.3 μm in the propagation range of about 50 μm except a fluctuation near the start position. 50 μm is very long considering the propagation length of the SPP respect to the wavelength of 632.8 nm, which means the realized Airy beam is a non-diffraction beam.

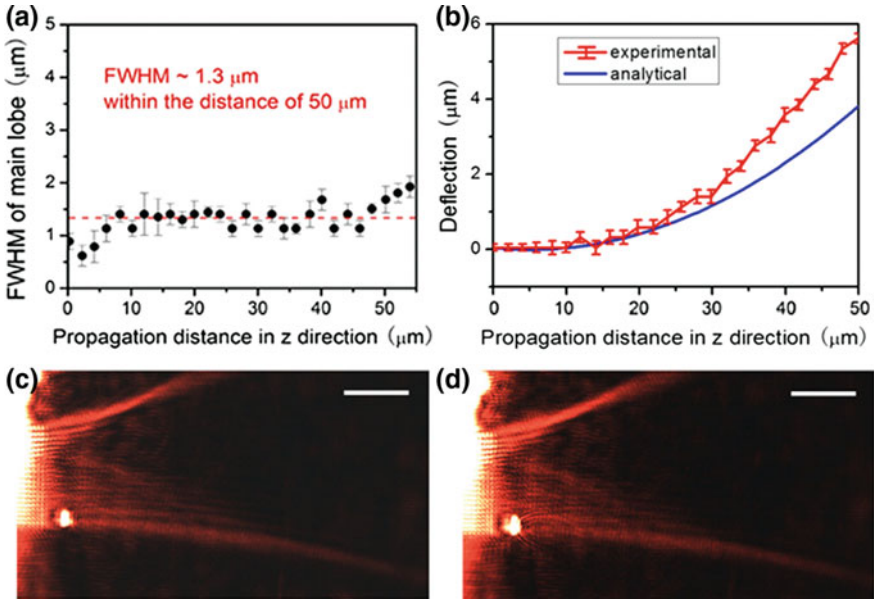


**Fig. 3.14** Properties of plasmonic Airy beam. **a** Non-diffraction. **b** Ballistic trajectory. **c**, **d** Self-healing properties. Figure adapted with permission from Ref. [10], APS

Next the self-bending property is examined. We plot the trajectory of the main lobe, which is shown in the red curve in Fig. 3.14b, while the theoretical trajectory corresponding to the experimental design parameter $\xi_0 = 1.08$ is shown in blue curve of Fig. 3.14b. The experimental trajectory shows considerable coincidence with the analytical parabolic curve. The deviation is because of the finite size of nanocave array.

In addition, we studied the self-healing property. Self-healing is a very interesting property of Airy beam. If Airy beam is block by some obstacle, it will be recovered after a certain distance from the obstacle. We artificially introduced two blocks in the beam paths to test the self-healing property, as shown in Fig. 3.14e and f for blocks of small ($1.5 \times 0.6\ \mu m^2$) and large ($2.2 \times 0.6\ \mu m^2$) rectangular holes, respectively. It is evidently that the SPP Airy beams really heal up by themselves for both cases, showing good self-healing property.

Non-diffraction, self-bending and self-healing properties are the most important properties of Airy beam. The achieved plasmonic Airy beam shows all the three properties, which means, there is no doubt that a well-developed SPP Airy beam is accomplished in a designable way.

The Eq. 3.2 is deduced under the paraxial condition, that is Airy beam can only exist in the paraxial condition [25]. According to the paraxial condition, the larger $\xi_0$ value is, the better condition is satisfied, which is proved by our calculation using Eq. (3.4) in Ref. [24]. We calculated the beam profile with different constant $\xi_0$ and the results are shown in Fig. 3.15. The beam will maintain a very good non-diffraction status in a very long propagation range when $\xi_0$ is large ($\xi_0 = 2.16$)

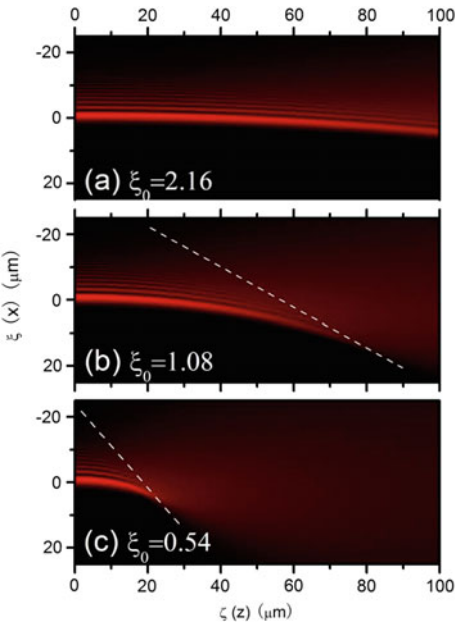


**Fig. 3.15** Profiles of Airy beams under different paraxial condition ($\xi_0$). **a** $\xi_0 = 2.16$, **b** $\xi_0 = 1.08$ and **c** $\xi_0 = 0.54$. Figure adapted with permission from Ref. [10], APS

as shown in Fig. 3.15a. However, if $\xi_0$ is small ($\xi_0 = 0.54$), the non-diffraction status will collapse to a featureless background quickly. Here we chose a median constant with $\xi_0 = 1.08$. The main lob can maintain the non-diffraction status in a propagation range of about 70 μm as shown in Fig. 3.15b. 70 μm is a good number for our experiment since the SPP suffers serious propagation loss and the propagation length is about 20 μm in the wavelength of 633 nm. When $\xi_0$ gets larger, the accelerating rate will be reduced as shown in Fig. 3.15a, so that it will depress the distinguishable of the self-bending property of Airy beam for such a lossy SPP case. Overall, we chose $\xi_0 = 1.08$, so that the beam can be remarkably distinguished without loose the Airy beam characteristics in a considerable propagation distance.

We further studied the energy variation during the propagation of the beam. The normalized intensity evolution along the main lob of the experimentally achieved plasmonic Airy beam is shown with the black squares in Fig. 3.16, while the intensity evolution of SPP Gaussian beam (shown in the inset of Fig. 3.16 recorded by LRM) is shown with red spots. Here we define the distance for the intensity to decay to 1/e as the propagation length. It is well demonstrated that Airy beam has a much longer propagation length ($\sim$50 μm) than the Gaussian beam ($\sim$15 μm), although its beam width preserves at a much smaller one. The plasmonic Airy beam doesn't change the propagation length of SPP. It only change the energy distribution on the surface. However, it will be quite helpful to the propagating and processing of the optical information.

We achieved plasmonic Airy beam with the nonlinear phase modulation method flexibly in previous section. However, the 1.5 power phase evolution is just the $\phi_0^+(x)$ part of formula 3.11. A good non-diffraction main lob of Airy beam can be realized with the 1.5 power phase evolution. But it is not a complete Airy beam. The $\phi_0^-(x)$ part is also essential to the formula 3.11, with which a complete Airy beam can be realized. The complete phase evolution can be realized with our nonlinear phase modulation method as well. We designed two set of non-periodic nanoarray as shown in Fig. 3.17a, in which the blue one is for the positive 1.5

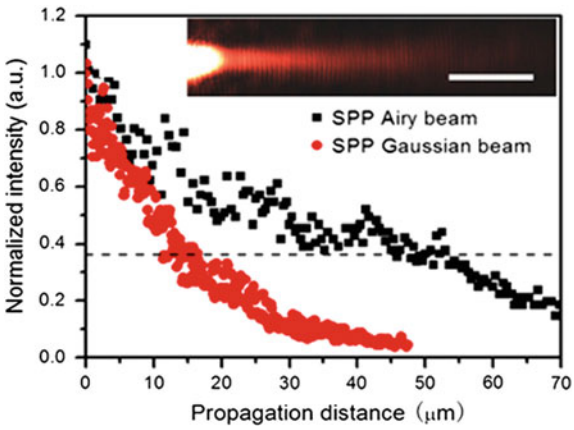


**Fig. 3.16** Propagation length of SPP Airy beam. Intensity evolution with propagation length of SPP Airy beam (*black squares*) and regular SPP Gaussian beam as the in set image (*red dots*). Figure adapted with permission from Ref. [10], APS

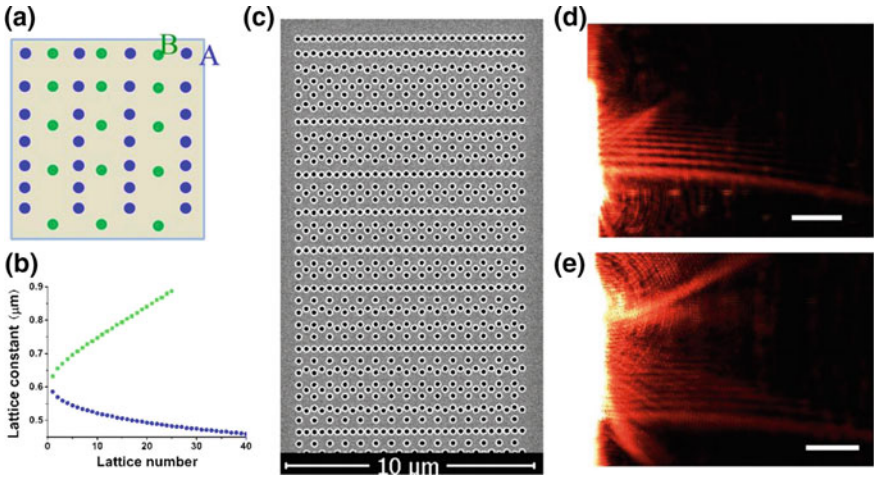


**Fig. 3.17** Realization of sine phase evolution. **a** Scheme of design for sine phase realization. **b** The designed lattice data for the nano-array. **c** SEM image for the nano-array fabricated by FIB. **d** Airy beam generated with sine phase evolution, comparing with **e** Airy beam generated with monotonic 1.5 power phase evolution

power phase evolution to realize $\phi_0^+(x)$ part, while the green one is for the negative 1.5 power phase evolution to realize $\phi_0^-(x)$ part. They are put together to realize both $\phi_0^+(x)$ and $\phi_0^-(x)$ simultaneously to get a sine wave packet for a complete Airy beam. Figure 3.17b are the design data for both positive and negative phase evolution. The SEM image of the fabricated sample is shown in Fig. 3.17b. Figure 3.17d is the result recorded by LRM. Comparing to the previous Airy beam with only the phase of $\phi_0^+(x)$ part (Fig. 3.17e), the main lob of Airy beam in Fig. 3.17d of the complete design is much better, and the sub-lobs are clearer as well. It is closer to the ideal Airy beam. It is concluded that the non-perfectly-match phase modulation method can not only realize the monotonic phase evolution, but can realize more complicated phase evolution as well. The phase modulation method is a general method which has an universal applicability.

In the same time Zhang et al. in UC Berkeley and Minovich et al. in Australian National University realized plasmonic Airy beam independently [26, 27]. Zhang generated Airy beam in free space and coupled it into SPP, while Minovich generated the wavefront of Airy beam with the coupling process between light and SPP. Their generation of plasmonic Airy beam relied on the out of plane process, which is not applicable for the 2D photonics integration. While our generation is completed totally in the 2D in-plane system, so that it will be more applicable for the realistic photonics integration.

In conclusion, non-perfectly-match diffraction is still effective in non-periodic arrays. With the non-perfectly-match diffraction, we can not only realize monotonic phase evolution, the more complicated non-monotonic phase evolution can be realized as well. With this phase modulation method, we achieved plasmonic Airy

beam by in-plane process. It provides a helpful inspiration to the in-plane manipulation of the optical energy distribution in 2D system without any structure restriction.

## 3.3 Summary

To break the restriction of Bragg's law, we proposed a method called non-perfectly-matched diffraction. The constructive diffraction exists even when Bragg's condition is not perfectly matched. The diffraction direction is determined by the lattice constant in the propagation direction and it was experimentally proved.

Based on the non-perfectly-match diffraction, a nonlinear phase modulation method was proposed with non-periodic array. The non-perfectly-match diffraction is not only effective in the periodic array, it is also effective in the non-periodic array. The phase modulation method breaks the restriction of Bragg's law, which can only realize a linear phase modulation. With this new method, we realized a 1.5 power phase evolution and a plasmonic Airy beam was demonstrated for the first time in the in-plane process. The achieved plasmonic Airy beam has the properties of ordinary Airy beam, such as non-diffraction, self-bending and self-healing. Meanwhile it can compensate the propagation loss of SPP. It is worth to notice that the phase modulation method together with the achieved plasmonic Airy beam are all in-plane processes, which will be more applicable to the future integration photonics than conventional manipulation method with the coupling process. Furthermore, this phase modulation method is not only useful for SPP manipulation, it can also be applicable to modulation the other waves.

## References

1. Siviloglou GA, Broky J, Dogariu A, Christodoulides DN (2007) Observation of accelerating Airy beams. Phys Rev Lett 99:213901
2. Siviloglou GA, Christodoulides DN (2007) Accelerating finite energy Airy beams. Opt Lett 32:979–981
3. Siviloglou G, Broky J, Dogariu A, Christodoulides D (2008) Ballistic dynamics of Airy beams. Opt Lett 33:207–209
4. Broky J, Siviloglou GA, Dogariu A, Christodoulides DN (2008) Self-healing properties of optical Airy beams. Opt Express 16:12880–12891
5. Carretero L, Acebal P, Blaya S, GarcÝa C, Fimia A, Madrigal R, Murciano A (2009) Nonparaxial diffraction analysis of Airy and SAiry beams. Opt Express 17:22432–22441
6. Baumgartl J, Mazilu M, Dholakia K (2008) Optically mediated particle clearing using Airy wavepackets. Nat Photonics 2:675–678
7. Polynkin P, Kolesik M, Moloney JV, Siviloglou GA, Christodoulides DN (2009) Curved plasma channel generation using ultraintense Airy beams. Science 324:229–232
8. Warren BE (1969) X-ray diffraction. Courier Dover Publications, USA

9. Oura K, Zotov A, Lifshits V, Saranin A, Katayama M (2003) Surface science. Springer, Berlin
10. Li L, Li T, Wang SM, Zhang C, Zhu S N (2011) Plasmonic Airy beam generated by in-plane diffraction. Phys Rev Lett 107
11. Baudrion A-L, Weeber J-C, Dereux A, Lecamp G, Lalanne P, Bozhevolnyi S (2006) Influence of the filling factor on the spectral properties of plasmonic crystals. Phys Rev B 74:125406
12. Born M, Wolf E (1999) Principles of optics: electromagnetic theory of propagation, interference and diffraction of light. CUP Archive
13. Durnin J (1987) Exact-solutions for nondiffracting beams. 1. The scalar theory. J Opt Soc Am A 4:651–654
14. Berry M, Balazs N (1979) Nonspreading wave packets. Am J Phys 47:264–267
15. Kaminer I, Segev M, Christodoulides DN (2011) Self-accelerating self-trapped optical beams. Phys Rev Lett 106:213903
16. Ellenbogen T, Voloch-Bloch N, Ganany-Padowicz A, Arie A (2009) Nonlinear generation and manipulation of Airy beams. Nat Photonics 3:395–398
17. Chong A, Renninger WH, Christodoulides DN, Wise FW (2010) Airy-Bessel wave packets as versatile linear light bullets. Nat Photonics 4:103–106
18. Polynkin P, Kolesik M, Moloney J (2009) Filamentation of femtosecond laser Airy beams in water. Phys Rev Lett 103:123902
19. Voloch-Bloch N, Lereah Y, Lilach Y, Gover A, Arie A (2013) Generation of electron Airy beams. Nature 494:331–335
20. Kaganovsky Y, Heyman E (2010) Wave analysis of Airy beams. Opt Express 18:8440–8452
21. Salandrino A, Christodoulides DN (2010) Airy plasmon: a nondiffracting surface wave. Opt Lett 35:2082–2084
22. Cottrell DM, Davis JA, Hazard TM (2009) Direct generation of accelerating Airy beams using a 3/2 phase-only pattern. Opt Lett 34:2634–2636
23. Chang S-H, Gray S, Schatz G (2005) Surface plasmon generation and light transmission by isolated nanoholes and arrays of nanoholes in thin metal films. Opt Express 13:3150–3165
24. Zhao C, Wang J, Wu X, Zhang J (2009) Focusing surface plasmons to multiple focal spots with a launching diffraction grating. Appl Phys Lett 94:111105
25. Novitsky AV, Novitsky DV (2009) Nonparaxial Airy beams: role of evanescent waves. Opt Lett 34:3430–3432
26. Zhang P, Wang S, Liu Y, Yin X, Lu C, Chen Z, Zhang X (2011) Plasmonic Airy beams with dynamically controlled trajectories. Opt Lett 36:3191–3193
27. Minovich A, Klein AE, Janunts N, Pertsch T, Neshev DN , Kivshar YS (2011) Generation and near-field imaging of Airy surface plasmons. arXiv preprint arXiv:1105.2625

# Chapter 4
# SPP Beam Engineering Based on Non-perfectly-matched Bragg Diffraction

Phase modulation is a high effective method to manipulate electromagnetic waves. Optical elements, such as lenses, gratings, zone plates and etc. are commonly used to modulate the phase of wave. In 1980s, researchers at MIT Lincoln Laboratory developed binary optics [1], a way of steering light propagation using phase-only modulation method, which has promoted optical researches, applications and the development of technologies in many areas. In 2011, Capasso's group in Harvard University proposed the concept of metasurface [2], which use a thin layer of metal structures to modulate the phase of light. Instantly, it gave rise to a new exciting upsurge of using phase to modulate light propagation. Non-perfectly-matched (NPM) Bragg diffraction method is also a new phase modulation method which achieves the non-linear phase modulation of in-plane SPP [3]. Thus we can expect that it will provide new opportunities for two-dimensional optical systems. Since the observation of self-bending Airy beam, people's enthusiasm for beam engineering rose again. Besides Airy beam, nonparaxial nondiffracting beams [4, 5], arbitrary nondiffracting beams [6–8] and etc. were proposed and realized. Among them, there are two kind of beams attracted particular attention. One is the collimated nondiffracting beam which has realistic significance in applications of optical integration; another is nonmonotonic beam, which reflects the capability of controlling the energy distribution of light in free space, which is important both in scientific researches and applications.

In this chapter, we will further reveal the physics and the applications of non-perfectly-matched diffraction phase modulation method. We first realize collimated SPP beams and propose a new method to control the intensity distribution of the collimated beams. Furthermore, we extend the method to beam generation with curved trajectories and successfully realize non-monotonic beams. We then achieve broad band SPP focusing, which can be used as demultiplexer with high spatial resolution. All these schemes and results can be extended to SPPs of other forms such as point sources, indicating the generality of our method. The flexibility of the phase modulation method in designs and applications will also be discussed.



L. Li, *Manipulation of Near Field Propagation and Far Field Radiation of Surface Plasmon Polariton*, Springer Theses,
DOI 10.1007/978-981-10-4663-6_4

## 4.1 Collimated SPP Beam with Controllable Intensity Distribution

Nondiffracting beams have attracted great research interests in recent years. They reflect people's capability to control energy and information of light in free space and will probably have significant applications in future information technologies. We expect to achieve nondiffracting beams in SPP system, which is one of the possible carrier of future all-optical integration, and will be of great importance both in fundamental scientific researches and applications. As mentioned in the previous chapter, Airy beam is one kind of nondiffracting beam. Actually, manipulations of nondiffracting beams, such as arbitrary accelerating caustic beams [6, 7], non-paraxial beams [4] and etc., have attracted increasing attention recently. In some sense, nondiffracting beams can be regarded as a particular kind of focusing keeping a preserved focal spot during beam propagation. Hence it is well worth controlling elaborately. However, the well demonstrated self-bending nondiffracting beams such as Airy beam would not be so applicable in on-chip integrations. To generate a straight beam with strong field confinement and controllable intensity would be more important in practical applications.

### *4.1.1 Collimated SPP Beam*

In principle, a collimated SPP beam can be formed by the interference of two intersecting plane waves, just like the generation of Bessel beam in free space [9]. It was realized on metal surface by Lin et al. as shown in Fig. 4.4. They call this kind of nondiffracting beam Cosine-Gauss beam [10]. Two intersecting placed gratings were designed to couple the incident laser to two Gaussian SPP beams with planar wavefronts. They will intersect at certain angle and interfere with each other. The coupled SPP beams are uniform within a certain region. Thus the intersecting part is nondiffracting leading to a collimated and nondiffracted SPP beam (Fig. 4.1).

However, as we all know plane wave has a linear-phase wavefront which is quite different from the 1.5-power phase type of Airy beam. By carefully investigating we can easily find that the self-bending feature of Airy beam should attribute to its phase distribution (1.5-power phase in $x < 0$ while exponential decay in $x > 0$). This asymmetric phase distribution leads to the asymmetric beam. Thus, we would intuitively consider whether we can use the 1.5-power phase to generate a collimated nondiffracting SPP beam. If yes, it would possibly contain novel physical ideas and thus open up a new avenue to engineer nondiffracting beams.

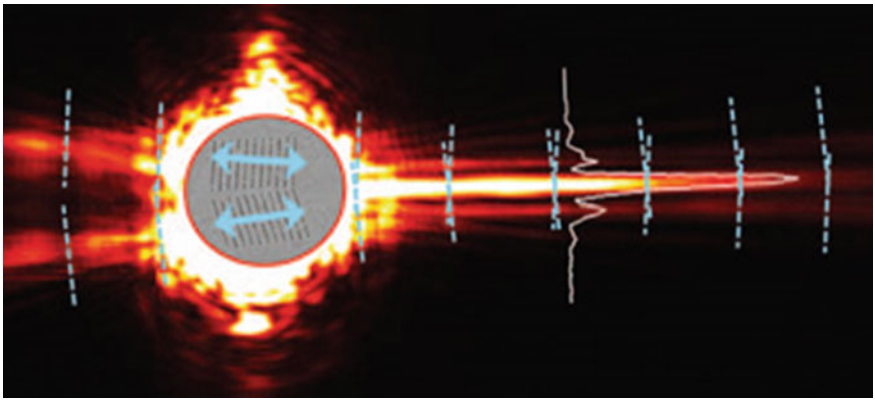

**Fig. 4.1** Cosine-Gauss SPP beam. Figure adapted with permission from Ref. [10], IOP

### *4.1.2 Collimated SPP Beams Generated by Non-perfectly-matched (NPM) Bragg Diffraction Method*

Here we investigate this scheme experimentally. Firstly, we utilize the NPM Bragg diffraction method to establish a symmetrical 1.5-power phase distribution which will lead to a symmetrical beam as shown in Fig. 4.2a [11]. The design parameters of the nanoarray are calculated by solving $\phi_m(x) = \psi(x)$, here $\psi(x) = cx^{1.5}$ (c = 0.6) is the symmetrical 1.5-power phase distribution. The result is depicted in Fig. 4.2c. The local lattice ($a_x$) of the nanoarray varies from 477 to 826 nm. The retrieved phase distribution along x direction (red dots) in Fig. 4.2d is consistent with the desired phase distribution (black curve). The sample with these parameters was fabricated on a silver film by FIB. Figure 4.2b shows the SEM image of the sample, where each unit is a rectangular nanohole with a size of 240 × 120 nm$^2$, depth of 20 nm and transversal period $P_z$ = 610 nm. The white arrow indicates the symmetric position ($x$ = 0), where the corresponding local lattice $a_x$ = 610 nm matches the Bragg's condition, and the lengths of the array on both sides of the symmetric position are almost the same (∼9.7 μm).

In experiment, we used a 633 nm He–Ne laser as the incident light. It was coupled to the SPP wave by grating on the metal surface. Figure 4.3a shows the image recorded by LRM system: two collimated SPP beams symmetrically distribute on both sides of the structure. For a clearer analysis of the generated beams, we retrieved the intensity distributions of the right beam at certain positions as plotted in Fig. 4.3b. It can be seen that a nearly nondispersive main lobe keeps the FWHM at 1.5 μm during propagating (∼30 μm before it vanishes) and has a high contrast compared with the surrounding lobes. More interestingly, the peak intensity of the main lobe increases gradually during propagating and then decreases suddenly at 30 μm as shown in the inset in Fig. 4.3b.

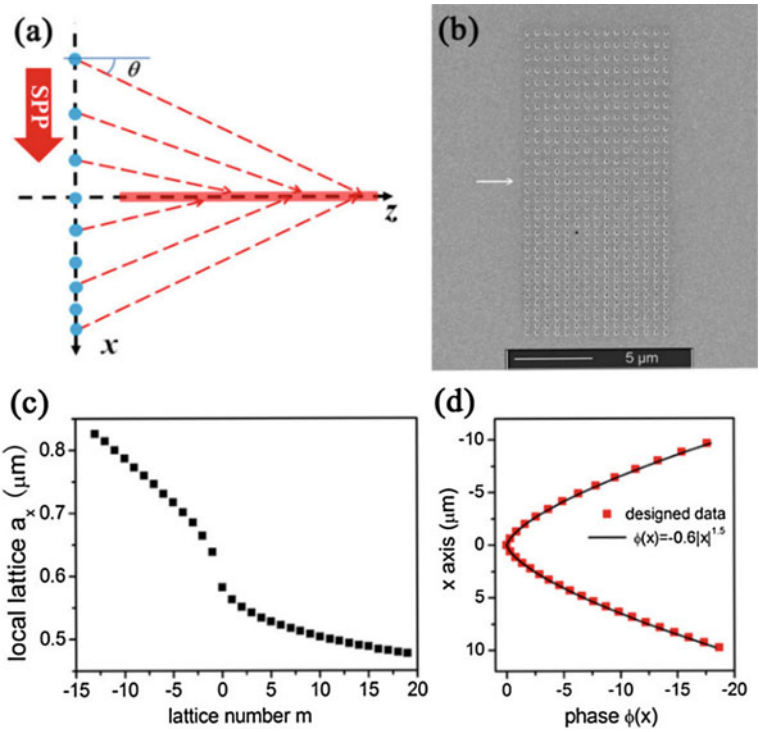


**Fig. 4.2** Symmetrical 1.5-power phase distribution generated by NPM bragg diffraction method. **a** Schematic diagram of symmetrical phase in SPPs system. **b** SEM image of the sample. **c** Design data for the phase generation. **d** The corresponding phase designed (*red dots*). Figure adapted with permission from Ref. [11], APS

A detail analysis is taken to the formation of the main lobe. The result of theoretical calculation based on Huygens–Fresnel principle is shown in Fig. 4.4. The SPP attenuation length is about 15 μm according to our previous experiments in last chapter. As we can see, the beam trajectory, profile and evolution of the intensity in the experiment are in good agreement with the theoretical results. It's easy to understand that symmetric phase distribution will undoubtedly form symmetric beam. And constructive interference always occurs in the center line because of equal phase, thus forming the main lobe. However, what's the underlying physics of the interesting intensity distribution? As it has been said in the NPM Bragg diffraction, a different local lattice will lead to an optimum diffraction angle ($\theta$). The angle can be derived from the differential of the corresponding phase distribution, as

$$\sin\theta = -\frac{1}{k}\frac{\partial\psi(x)}{\partial x} = \frac{cn}{k}x^{n-1} \tag{4.1}$$

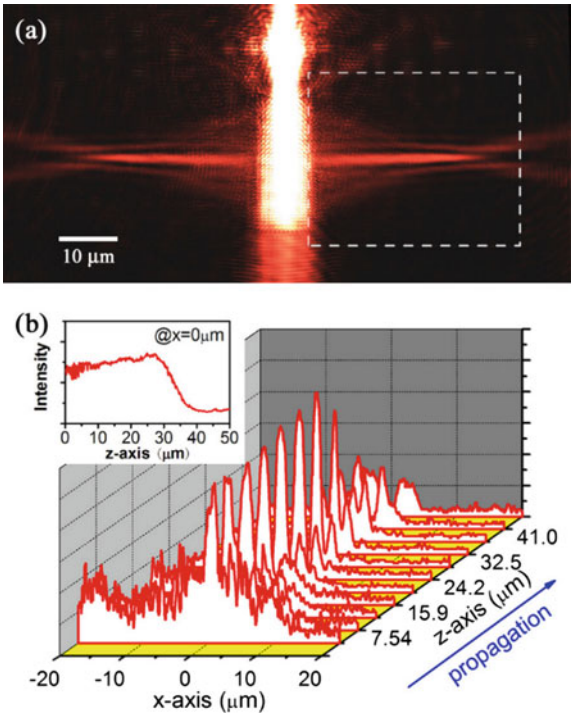


**Fig. 4.3** **a** The propagating image of SPP recorded by LRM. **b** The intensity profiles at different positions within the white region in **a**, the inset depicts the intensity of the main lobe along propagation. Figure adapted with permission from Ref. [11], APS

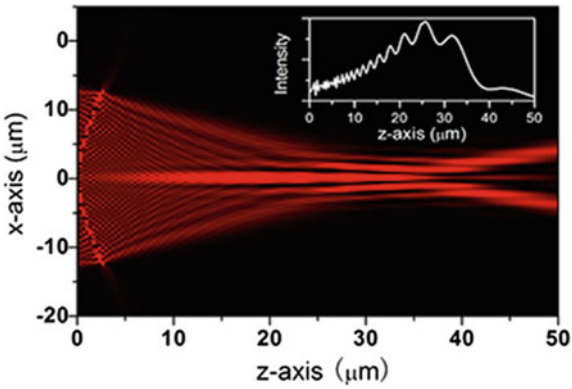


**Fig. 4.4** Theoretical calculated SPP beam, where the inset image shows the intensity variation of the main lobe against the propagation length. Figure adapted with permission from Ref. [11], APS

where $\psi(x) = -cx^n$. The diffracted SPPs can be regarded as a cluster of geometrical rays, intersecting with z axis. Thereby, the relation of the intersections and the corresponding source positions in the x axis can be derived as

$$z_a = x_a \cot\theta = \sqrt{\left(\frac{k}{cn}x_a^{2-n}\right)^2 - x_a^2} \tag{4.2}$$

Here, $(0, z_a)$ and $(x_a, 0)$ are the coordinates of the intersection and the corresponding source position, respectively (as shown in Fig. 4.5a). Calculating Eq. 4.2 with $n = 1.5$, $c = 0.6$ as before, we get a curve as shown in Fig. 4.5b. The slope increases gradually with the increasing of z. As the diffracting sources along the x axis distributed evenly, we can then conclude that more sources contribute to enhance the intensity of the main lob as the beam propagates. The blue dash line in Fig. 4.5b represents the boundary of the designed array ($\sim$9.7 μm). Thus no source out of the structure will contribute to the beam, leading to an abrupt drop in the intensity at about 34 μm. The analysis is consistent with the above theoretical and experimental results, indicating a close relation between Eq. 4.2 and the beam formation.

Furthermore, we calculated the cases of other symmetric phase distributions with n changing from 1.0 to 1.8. Figure 4.6a–d shows the experimental results of the

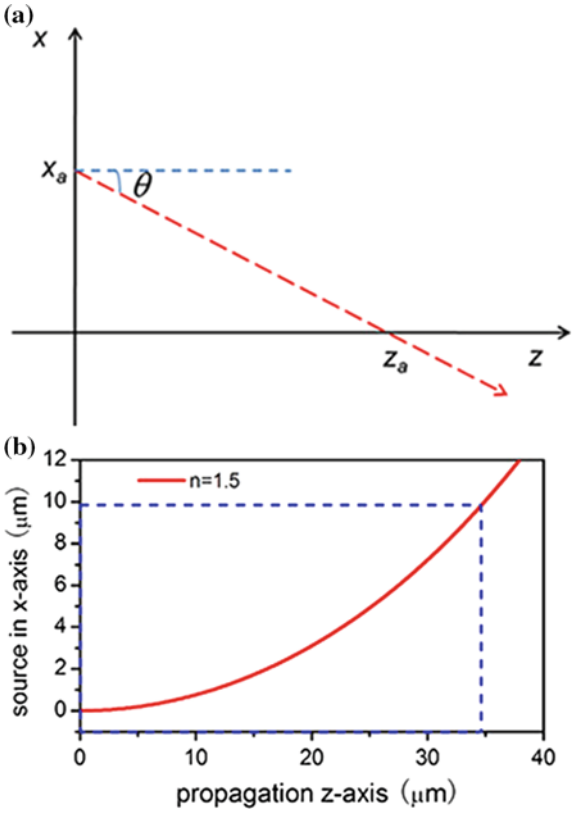


**Fig. 4.5** The relation between sources and intersections. **a** The schematic of a ray propagation. **b** The relation of source to beam (the intersection). Figure adapted with permission from Ref. [11], APS

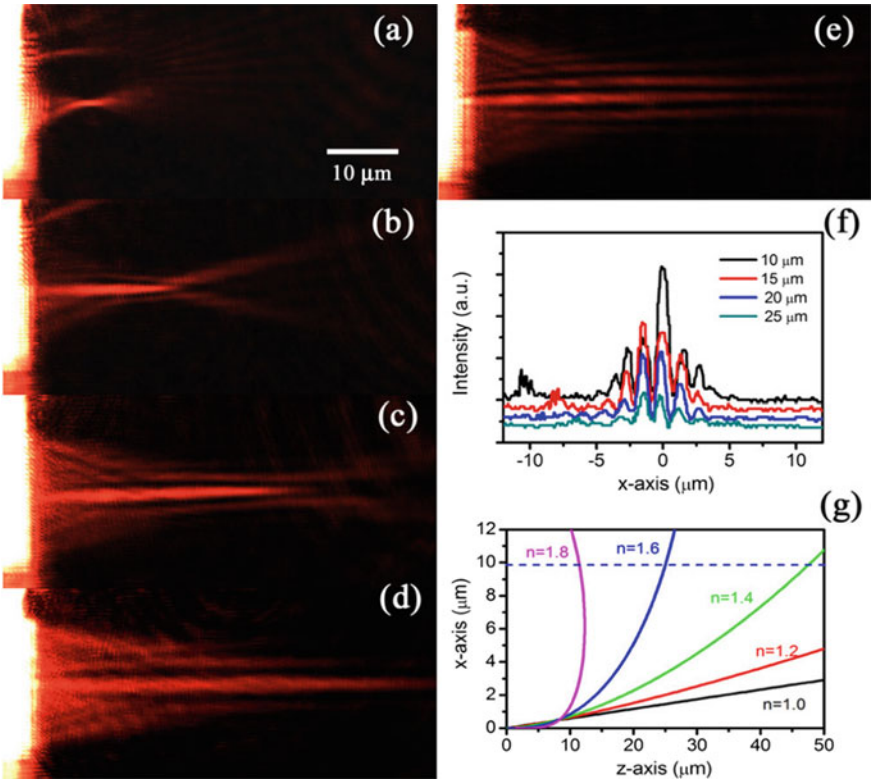


**Fig. 4.6** **a**–**e** SPP beams at the case of n = 1.8, 1.6, 1.4, 1.2 and 1.0, respectively. **f** The beam intensity at different z positions at the case of n = 1.0. **g** The source-to-beam relation curves for all cases with constant c = 0.6. Figure adapted with permission from Ref. [11], APS

samples with c = 0.6 and n = 1.8, 1.6, 1.4 and 1.2, respectively. A clear evolution from a strong focusing to a nearly nondiffracting beaming is demonstrated. However, with the decrease of n, the length of the beam will be longer and longer and the intensity will be too disperse to be observed. So we increase the constant c to get a much more concentrate intensity in the case of smaller n. In Particular, we studied the case with c = 1.5 and n = 1 showing in Fig. 4.6e. That is equivalent to the case of two plane waves intersecting with a certain angle, which is similar to Lin's method to generate Cosine-Gauss beam [1]. Figure 4.6f shows the beam intensity at different positions along propagating. The width was preserved during propagation, indicating the feature of nondiffracting. Besides, we also calculated their source-to-beam diagrams in the case of different phase distributions showing in Fig. 4.6g. Expect the linear case of n = 1.0, all the others are curves with different increasing tendency. The same as the previous n = 1.5 case, there is a cutoff in the main lobe due to the finite structure, as indicated by the blue dash line. Actually, the light beam is truly nondiffracted only at the case of n = 1.0. However, as indicated in the experiment, the beam widths in other cases are nearly changeless, which can also be regarded as nondiffracting to some extent.

According to the discussion above, we can find out the substantial effect of source-to-beam relation in the process of beam formation. For a further understanding, we will investigate several special kind of beams firstly. Their source-to-beam relations can be obtained from Eq. 4.2 as:

$$z = \pm x\sqrt{\left(\frac{k}{cn}\right)^2 - 1}, \quad (n = 1); \tag{4.3}$$

$$z^2 + \left[x - \frac{1}{2}\left(\frac{k}{cn}\right)^2\right]^2 = \frac{1}{4}\left(\frac{k}{cn}\right)^4, \quad (n = 1.5); \tag{4.4}$$

$$z^2 + x^2 = \left(\frac{k}{cn}\right)^2, \quad (n = 2). \tag{4.5}$$

As we can see, for the case of n = 1 (i), the source-to-beam relation corresponds to a straight line; However, for the case of n = 1.5 (ii) and n = 2 (iii), they are two circular curves with different radiuses and centers, as shown in Fig. 4.7a. With the

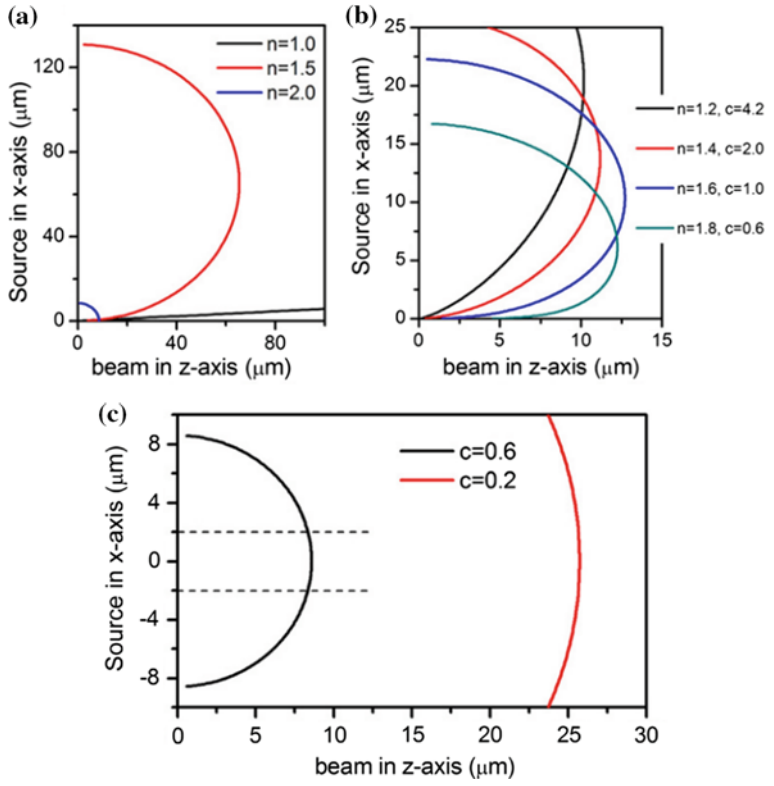


**Fig. 4.7** **a** Source-to-beam relation at the case of c = 0.6. **b** Source-to-beam relation at the case of different n and c. **c** Source-to-beam relation at the case of n = 2.0. Figure adapted with permission from Ref. [11], APS

same constant c, the radius of curve (ii) is much larger than the radius of curve (iii). When c = 0.6 as adopted in our experiment, the corresponding radiuses are $r_{(\mathrm{ii})} = \frac{1}{2}\left(\frac{k}{cn}\right)^2 = 65.49\,\mu\mathrm{m}$ and $r_{(\mathrm{iii})} = \left(\frac{k}{cn}\right) = 11.44\,\mu\mathrm{m}$, respectively. Hence we didn't compare these two cases in our experiment due to their high contrast.

For other values of n, the corresponding source-to-beam relations can be calculated numerically. As discussed above, the ultimate relation curves are determined by the values of coefficient c and phase factor n. To locate the curves in our desired range, the coefficient c was appropriately selected for different n. The results are shown in Fig. 4.7b. As the source position increases, all the curves experience maximum values which indicate the maximum length of the corresponding beams. These curves start from z = 0, that is to say the corresponding beams also starts from the initial place of z = 0 regardless of the beam intensity, which is significantly different from the case of n = 2.

In the case of n = 2, the intersection of the ray and z axis moves from the focus position to the negative direction of z. In fact, the method using 2-power phase to achieve focusing is just in paraxial approximation, which is clearly shown in Fig. 4.7c. The black arc represents the result of n = 2 and c = 0.6. In this case, if source region has a range of $-10\ \mu\mathrm{m} < x < 10\ \mu\mathrm{m}$, the corresponding beam will cover a wide range of $0 < z < 8.5\ \mu\mathrm{m}$. That is not a typical focusing. But if we shrink the source region to $-2 < x < 2\ \mu\mathrm{m}$, indicated by the black dashed lines, the arc will project a small region in z axis leading to a good focusing as the paraxial approximation is fulfilled. In order to design a better focusing, a much smaller coefficient c is needed to get a longer focal length, thus satisfy the paraxial approximation in a much wider range. For example, as the red arc with c = 0.2 showed in Fig. 4.7c, the intersections concentrate around 25 μm leading to a good focusing with focal length of 25 μm.

### 4.1.3 *Intensity Modulation of Collimated SPP Beam*

As has been discussed above, the beam intensity is influenced by the source-to-beam relation which is determined by the initial phase distribution. So we wonder whether we can change the beam intensity by phase design. As we know, the applications of SPP wave are limited by its large propagation loss. As a result, to compensate or reduce the loss will play an important role in SPP applications. Indeed, in the case of c = 0.6 and n = 1.5, the formed SPP beam has already been compensated and even strengthened in a certain region. Actually, by modulating the source-to-beam relation, we can achieve arbitrary intensity distribution including intensity-preserved SPP beams. While knowing the source-to-beam relation, we can deduce certain phase distribution for a desired intensity distribution from the relation of source-to-beam relation. The phase distribution can be further achieved by certain phase design method, such as the NPM phase modulation method.

According to the previous discussion, we know that the ray density ρ(z) through one position of z-axis is proportional to the slope of the source-to-beam relation at the corresponding point (as shown in Fig. 4.8b), i. e. $\rho(z) \propto dx/dz$. Assuming an SPP beam with a propagation length of $l$ and a source with even intensity distribution along x-direction, the beam intensity in the z axis contributed by a unit source can be expressed as:

$$I_i \propto \exp(-r/l) = \exp(-x/l \sin\theta) \tag{4.6}$$

Here r is the propagation length from source to beam. We want to get a lossless SPP beam, that is the beam intensity is fixed along the propagation as $I(z) = \rho(z)I_i = c$ by certain phase design. That is:

$$(dx/dz)\exp(-x/l \sin\theta) = c \tag{4.7}$$

By solving Eqs. 4.1, 4.2 and 4.7, we get the phase distribution for a lossless SPP beam. The calculated result with $l$ = 15 μm is shown by the red line in Fig. 4.8c together with the 1.5-power phase distribution (black line) for comparison. As we can see, the designed lossless one has a smaller curvature than the case of 1.5-power phase. It is reasonable for the latter has an increased intensity along propagation. Figure 4.8a is the theoretical calculated propagation image for the designed phase distribution based on Huygens Fresnel principle, with the intensity distribution of

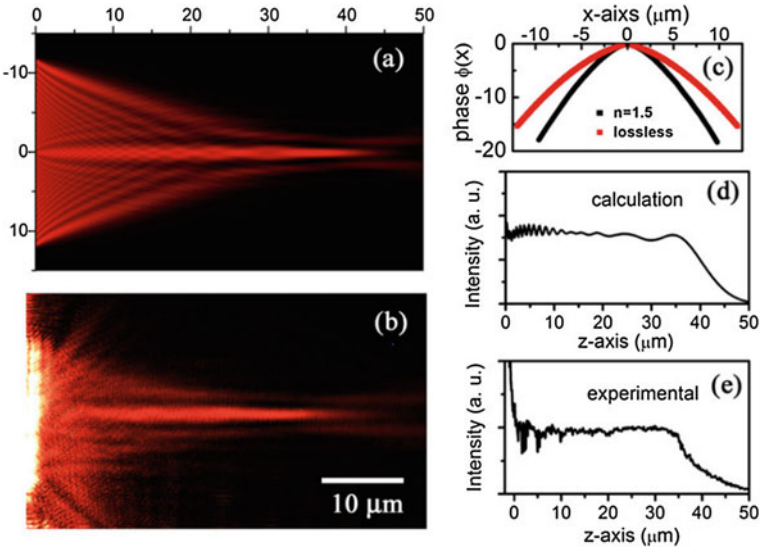


**Fig. 4.8** The realization of lossless SPP beam. **a** The theoretical calculated propagation image. **b** The experimental image recorded by LRM. **c** The corresponding phase distribution of lossless SPP beam (*red line*) compared with the 1.5-power case (*black line*), The calculated (**d**) and experimental (**e**) intensity distributions of the corresponding main lobes. Figure adapted with permission from Ref. [11], APS

the main lobe depicted in Fig. 4.8d. Clearly, the intensity keeps almost unchanged during propagation. (It should be noted that the SPP source points were evenly selected from the derived phase distribution and radiate cylindrical waves on the metal surface. Different from the previous method using metal nanostructures as radiation source, here the propagation image was generated by the point sources with certain phases.)

Next, we use the previous NPM phase design method to design nano arrays and carry on the corresponding experiments. Figure 4.8b is the image recorded by LRM, which is almost the same with the theoretical result showing in Fig. 4.8a. Figure 4.8e is the intensity distribution of the main lobe with a preserved intensity within 35 μm, except for a strong disturbance in a small range near the structure. Thus, an intensity-preserved and nearly nondiffracting SPP beam is well demonstrated through the above critical design.

From the discussion above, it is easy to conclude that any intensity distributions might be realized by using the source-to-beam relations. Assuming an arbitrary intensity distribution $F(z)$, we can get the required phase distribution by solving $I(z) = \rho I_i = cF(z)$. Here, we take an exponential increasing beam with $F(z) = \exp\left(\frac{z-z_0}{l'}\right)$ as example, where $l'$ is a coefficient and $z_0$ is a start point. Figure 4.9a depicts the designed phase distribution in the case of $l' = 20$ μm, $z_0 = 10$ μm, which has a much greater curvature compared with the phase distribution of the lossless SPP beam. The theoretical calculated result is shown in Fig. 4.9b with intensity of the main lobe retrieved (red line) in the inset, where an exponential increase profile is clearly presented from z = 10 to 40 μm. Here we didn't carry out corresponding experiment, because the source range ($-24 < x < 24$ μm) in the calculation is relatively larger than the practical SPP propagation length. However,

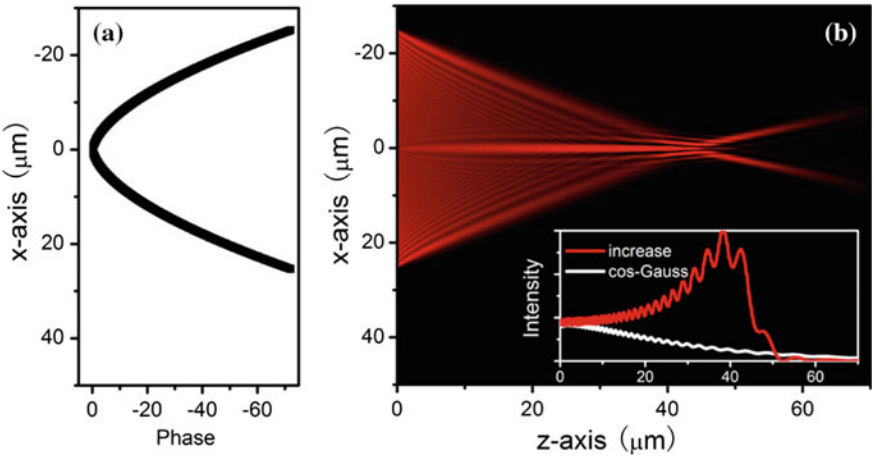


**Fig. 4.9** **a** The required phase distribution for an intensity exponential increasing beam. **b** The propagation image by theoretical calculation. Inset is the calculated intensity of the main lob and that of a cos-Gauss beam in the same situation. Figure adapted with permission from Ref. [11], APS

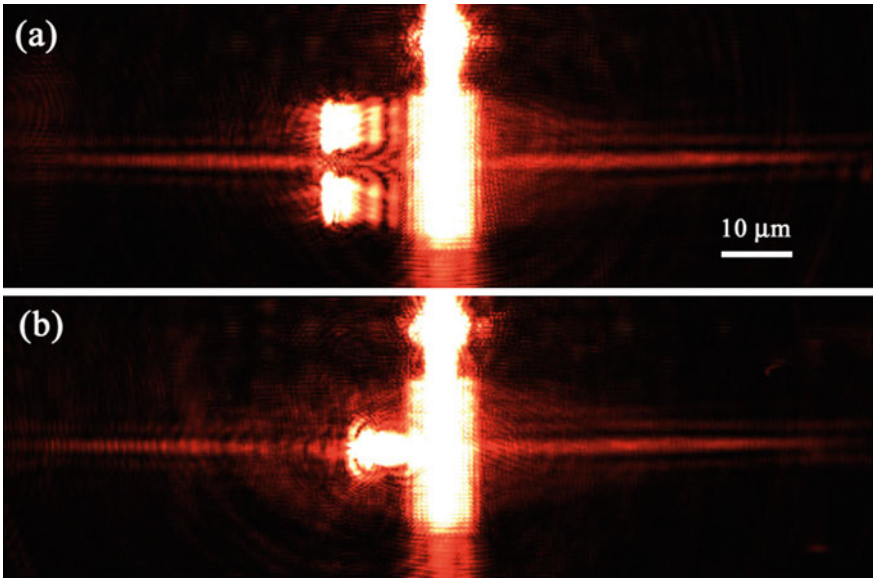


**Fig. 4.10** Self-healing property of the collimated SPP beam. Figure adapted with permission from Ref. [11], APS

as long as the source is large enough, we believe that beams with arbitrary intensity distributions can be achieved using the method above, which would possibly imply particular applications in some particular areas (e.g., in optical trapping). Notably, this design scheme is valid not only for the lossy SPP but also for other beam systems, only replacing the item of $\exp(-r/l)$ with a more general form.

The achieved collimated SPP beams also have self-healing property as the Airy beam, which is demonstrated experimentally with the phase parameters c = 0.6 and n = 1.4 as shown in Fig. 4.10. Big holes (6–8 wavelength in size) were fabricated by FIB in the SPP beam path to block the side lobes (Fig. 4.10a) and the main lobe (Fig. 4.10b), respectively. The blocking and self-healing processes of the left beams are clearly observed compared with the intact ones on the right side. However, the situation of the self-healing is not so much consistent with the above explanation of source-to-beam relation because the obstacles could not block the SPP beams totally. However we can still find the relation between the blocked source and the corresponding beam by comparing the left beams at the same positions in Fig. 4.10a, b. It should be mentioned that the NPM Bragg diffraction method and the phase-ray relation described by geometric optics are both based on average effects. Thus they will not be so suitable when consider a precise position. Here the self-healing property of this kind of collimated SPP beam is well demonstrated.

In summary, we achieved a series of collimated SPP beams including non-diffracting ones by utilizing symmetrical phase distribution. Meanwhile, we proposed an understanding about the source-to-beam relation and explained the beam formation successfully. Moreover, according to the explanation, we proposed a new

intensity modulation method by phase, subsequently achieving collimated SPP beams with preserved and exponential increased intensities distributions, respectively.

### 4.1.4 Research on Nonmonotonical Beams

In the previous section, the constructive interference always occurs along the optical axis due to symmetrical phase distribution, forming collimated SPP beam. It is easy to extend the model to a much general case. As shown in Fig. 4.11a, the straight optical axis is transformed to a bending one. And the phase distribution on both sides of the relative positions are still symmetrical about the new axis. As a result, arbitrary bending beams with high contrast can be achieved due to constructive interference along the curving axis. Furthermore, we can enhance the beam-background contrast by design more rays that constructively interfere and superimpose on the beam as shown in Fig. 4.11b.

According to the scheme, we calculated the required phase distribution of a certain beam with a bending trajectory and obtain such phase distribution by NPM Bragg diffracting method. Both theoretical and experimental results are presented in Fig. 4.12a, b, where the beam with the designed bending trajectory is well demonstrated.

However, we are just achieving some preliminary results. There are still a lot of deficiency on contrast, beam intensity and so on in these results, which need further optimization and improvement. But the results above have already shown the advantages of the method on unconventional beam generation. In recent years, the researches on beam steering have attracted a lot of attention and several special beams have been achieved successively. Besides the beams discussed above, the non-paraxial nondiffracting beam [4, 5, 12], the arbitrary beams with monotonic trajectory [6–8, 13] and so on were realized as well. Some new methods of beam modulation have also been proposed, including holographic method [14–16],

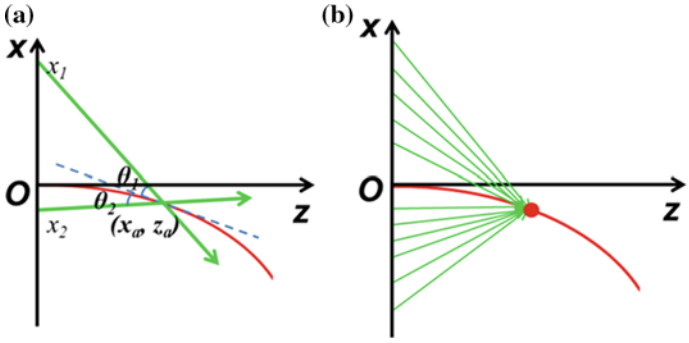


**Fig. 4.11** **a** The general and **b** Improved schemes of the symmetrical phase method

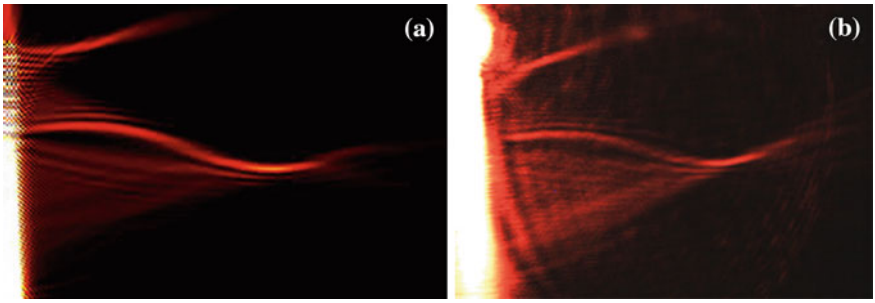


**Fig. 4.12** **a** Calculated and **b** Experimental results of an arbitrary bending beam by symmetrical phase method

caustic method [7] and so on. Comparing with these methods, our method has a clearer physics and might achieve much higher contrast. We can expect that it will have specific applications and significances on the modulations of beams with curving, even non-monotonic and arbitrary trajectories and inspire the research on optical field modulations.

## 4.2 Focusing and Demultiplexing of SPP Beam

Focusing is one of nature's most common and important optical phenomena. It can gather energy or information at the focal point to achieve a much higher intensity, which is rather useful in processes of collecting, detecting and so on. SPP focusing also attracted a lot of attention. Arc-shaped slit [17], grating [18–20], V-shaped waveguide [21], conical-shaped structures [22, 23] and so on have been proposed to convert free space light to subwavelength focused SPP. Zhang's group have proposed a binary plasmonic method to design different binary plasmonic structures, which can be used to realize single and multiple SPP focal spots [24, 25]. However as we have discussed before, these methods to achieve SPP focusing are based on 3D coupling process, which is not applicable in 2D photonic integration. It is required to achieve in-plane SPP focusing without coupling process. Though the in-plane zone plate was proposed to obtain SPP focusing on the metal surface [26, 27], it requires a relative wide SPP beam which is a disadvantage for optical integration. A more applicable method for in-plane focusing is needed.

On the other hand, demultiplexer is a critical device in optical information and technologies, which is used to divide light of different frequencies to different channels. Since the increasing requirement of information capacity, a much higher frequency resolution is desired and different frequencies need to be separated to different ultra-narrow channels. Due to the subwavelength confinement, SPPs provide great opportunities to increase the resolution. The Bull's eye structures [28], the metal/dielectric/metal (MIM) structures [29] and so on have been proposed to realized frequency division by SPPs. However, all of these results were realized

in 3D space, which are not applicable to 2D photonics integration. Recently, Zhang's group, Tanemura and etc. have realized SPP demultiplexing in the form of focusing by designing coupled structures on the metal surface [30, 31]. Due to the process of focusing, they can separate the SPPs with different frequencies to much narrower regions and achieve higher resolution. Unfortunately these focusing and demultiplexing are rely on the coupling process which is not practical for the 2D system as well. As in the realm of in-plane manipulation, plasmonic crystal was designed to realize double-wavelength demultiplexing [32]. However, this kind of plasmonic crystal is based on Bragg's principle, thus is only valid for the design wavelength, not to mention the resolution. To achieve the more data channels with high resolution, we try to realize the focusing as well as the demultiplexing through in-plane manipulation.

### 4.2.1 Focusing of SPP

First, we would demonstrate the SPP focusing of a single wavelength on the metal surface. As we have known in the previous chapter, NPM Bragg diffraction method, written as $\phi(x) = \phi_0 + k_{spp}x - 2m\pi$, can be used to realize various kinds of continuous phase modulations. Based on this method, we can achieve focusing through a quadratic phase evolution. The desired structure parameters can be deduced by solving equation $\phi_m(x) = \psi(x)$, in which $\psi(x) = -kx^2/2f_0$ is the quadratic phase distribution with a focal length of $f_0$.

Figure 4.13a, b are the schematic diagrams of our design [33]. An SPP wave launched by a focused laser with grating coupling method incidents directly into a non-periodic nanocave array. By appropriately designing the nanoarray, the diffracted SPP waves will process square phase distribution and focus to spots in both sides of the array. Figure 4.13c depicts the local lattice data along x direction, which is the distance between two adjacent nanocaves along the propagation direction of the SPP. The period in the z direction was chosen as $p_z$ = 640 nm to make diffracting intensity almost even within the whole structure and get a well focus. The designed sample was fabricated by FIB on a 60 nm thick silver film. Both of the grating and nanoarrays have a depth of 20 nm. Each nanocave has the size of 120 nm × 240 nm and the long side is long x direction. Here the rectangle-shaped nanohole is chosen, which is different from the structure adapted in the last chapter, to get a more even diffracting intensity distribution. The well-demonstrated SPP focusing with a focal length of 40 μm recorded by the LRM system is shown in Fig. 4.13d. Further, we did theoretical calculation with the corresponding structure based on Huygens-Fresnel principle and the result is shown in Fig. 4.13e, which is in good agreement with the experimental one. Figure 4.13f illustrates the profiles of the focal spots, whose full widths at half-maxima (FWHM) in experiment are about 12.2 and 0.93 μm in longitudinal (z) and transverse (x) dimensions, respectively, agreeing well with the calculated values of 9.35 and 0.82 μm accordingly. It is worth to mention that the SPP intensity at the foci (about

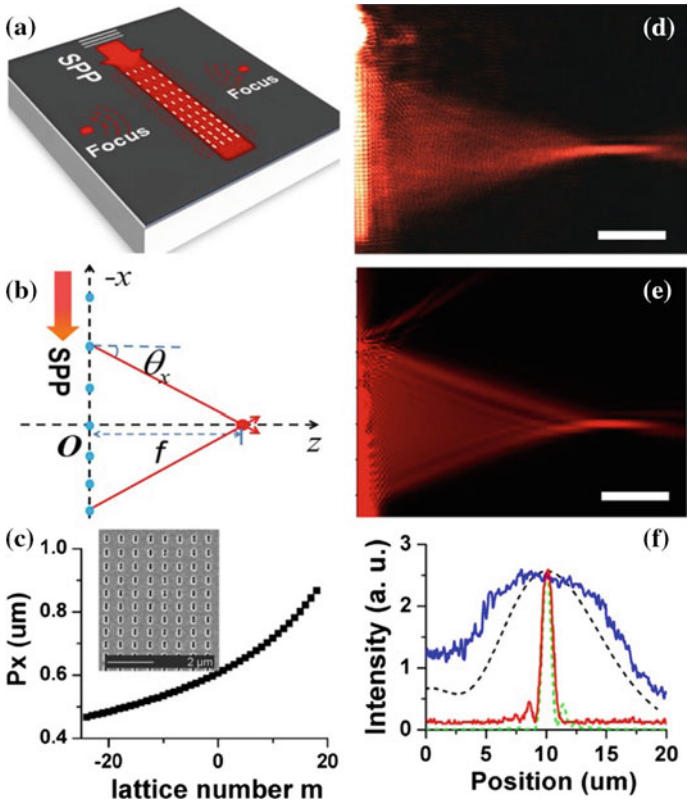


**Fig. 4.13** SPP focusing by NPM Bragg diffraction method (**a**) Schematic of focusing propagating SPPs. **b**, **c** Designed non-periodic lattice parameters in x-dimension for horizontal focus. Experimental (**d**) and Theoretical (**e**) result of SPPs focus. **f** Intensity profiles of the focal spots in **d** (*solid line*) and **e** (*dash line*). The *red* and *green lines* are the longitudinal profiles and the *blue* and *black lines* are the transverse ones (scale bar = 10 μm). Figure adapted with permission from Ref. [33], ACS

60 μm away from the SPP source—the grating coupler) is as strong as the intensity only 20 μm away from the source due to a focusing effect. As we all know, SPPs were limited in practical applications due to their strong propagation loss, which however can be overcome to some extent by the property of the focusing.

### *4.2.2 Broad Band Focusing and Demultiplexing of SPPs*

As shown in Fig. 4.13c, the designed lattice parameters, which determine the diffracting directions and phase distribution of the SPP at corresponding wavelength, have almost a linear increment against the corresponding lattice numbers in a certain range. In other words, our design may be applicable to SPPs with different

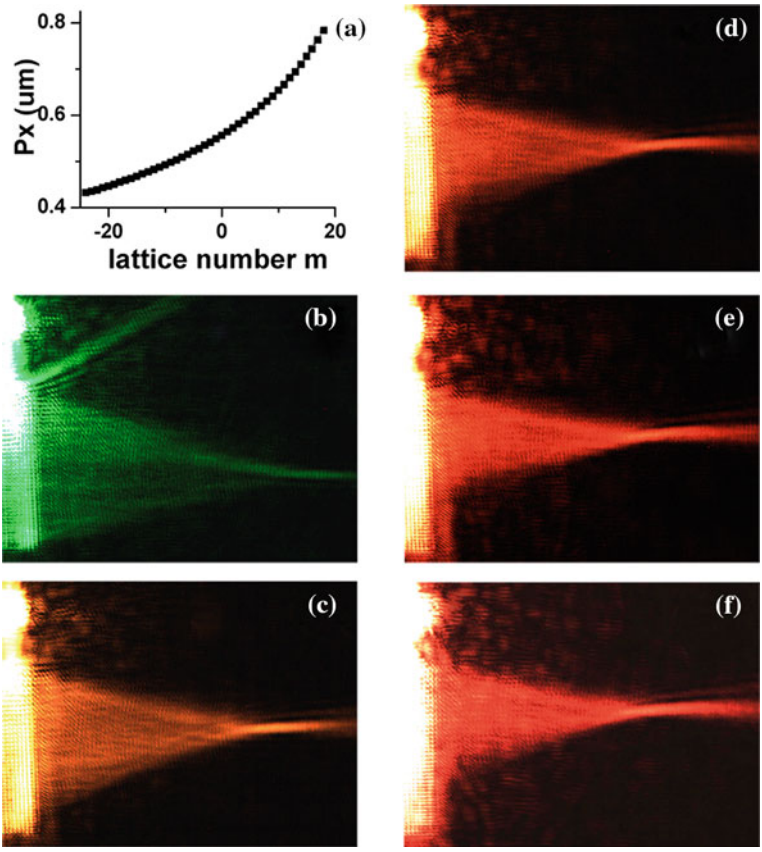


**Fig. 4.14** Broad band focusing of SPPs. **a** Design parameters of the structure. **b–f** The experimental focusing images detected by LRM with the laser wavelengths of 543 nm (**b**), 594 nm (**c**), 604 nm (**d**), 612 nm (**e**), and 633 nm (**f**), respectively. Figure adapted with permission from Ref. [33], ACS

wavelengths around the designed one, leading to broad band effect, which was also demonstrated in our experiments. The structure was designed to generate focusing with a focal length of 40 μm for an SPP of 560 nm (the corresponding free space wavelength is about 580 nm) and the design parameters along x direction is depicted in Fig. 4.14a with a lateral period of $p_z$ = 560 nm. A five-color He–Ne laser (543, 594, 604, 612 and 633 nm) was used as the incident source and the corresponding results were shown in Fig. 4.14a–e, where the focusing of SPPs of wavelengths from 543 nm (green) to 633 nm (red) are well demonstrated, indicating a broad band responses of about 100 nm. The lateral FWHMs of the focal spots change from 0.9 to 1.3 μm as the incident wavelength increases as illustrated by red dots in Fig. 4.15.

To better demonstrate the realization of focusing for all these wavelengths, we retrieved the phase distributions for the five wavelengths at the original position

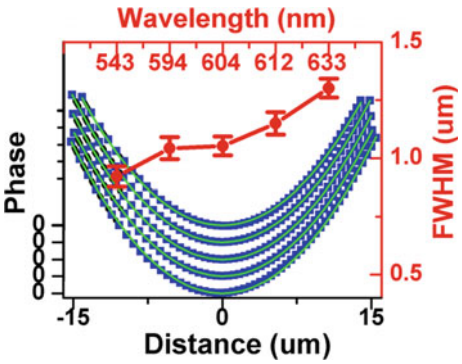


**Fig. 4.15** The analysis of broadband focusing. *Red dots* represent the foci FWHMs of different wavelengths; *blue dots* represent the retrieved phase distributions from experimental results; *green lines* represent the theoretical required phase distributions. The lines from *bottom* to *top* correspond to the cases of 543, 594, 604, 612 and 633 nm, respectively. Figure adapted with permission from Ref. [33], ACS

according to the practical measured focal lengths and directions. The results depicted by square dots in Fig. 4.15 are in good agreement with the theoretical required quadratic phase distributions for focusing (shown as blue lines in Fig. 4.15), which explains why we can get the focusing results within the wavelength range in the experiments. Nevertheless, the phase deviation from the theoretical required phase distribution trends to increase when the operating wavelength is far from the designed one, leading to a worse focusing result in the experiment. However in practical applications, a better focusing effect can be fulfilled with a careful trade-off between the required bandwidth and the design wavelength. Here, our design is enough to realize a focusing with a bandwidth of 100 nm in the visible range.

Also our structure can be used as a demultiplexer for the property that the SPPs of different wavelengths are focused to different positions. For a clear demonstration, we introduce another He–Ne laser (633 nm) as a reference together with the previous five-color laser, which then incident onto the coupled structure as a dual-wavelength SPPs source. Figure 4.16a–c are the experimental results corresponding to the incident laser beams of 633 nm together with 594, 604, and 612 nm in turn, where the variation of the distance between the focal spot of the corresponding SPP and that of the reference SPP was clearly observed. The lateral cross-section of the intensity at the focal spots are shown in Fig. 4.16d by aligning the focus positions of the reference SPP. The relation between the wavelength differences ($\Delta\lambda = \lambda - \lambda_{ref}$) and the focal distances (d) can be obtained as $\Delta\lambda(d)$. We can also get the average $FWHM_a$ of the focal spots around the wavelength range. Thus the resolution of the SPP demultiplexer can be written as:

$$R = \Delta\lambda(d = FWHM_a) \tag{4.9}$$

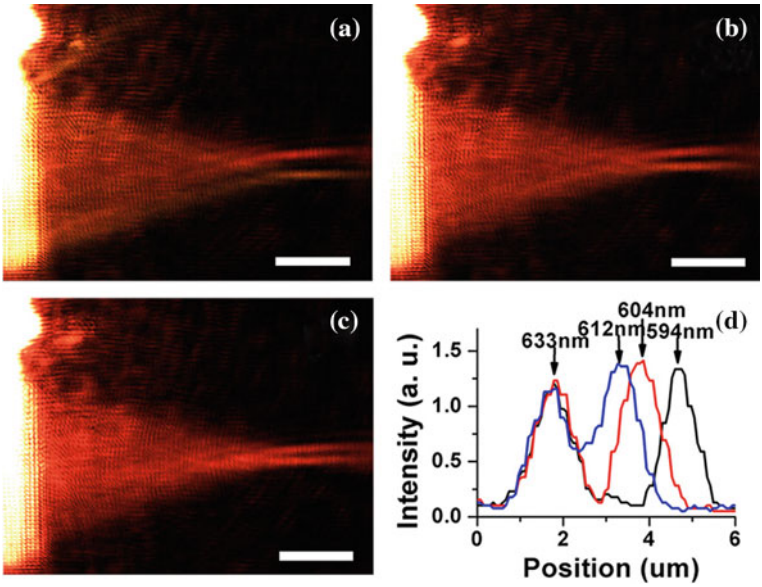


**Fig. 4.16** Experimental results for dual-wavelength beams. LRM detected SPP focusing of reference wavelength $\lambda 1 = 633$ nm and operating wavelength $\lambda 2 =$ **a** 594 nm, **b** 604 nm, **c** 612 nm, respectively. **d** The lateral profile of the focal spots. Figure adapted with permission from Ref. [33], ACS

Strictly speaking, it is not a very accurate method to use an average FWHM to determine the resolution of the device, because the FWHM is also a function of SPP wavelength. However, the practical FWHMs of the focal spots of the nearby wavelengths change very little, thus having limited influence on the resolution. So the definition of resolution from the Eq. 4.9 is suitable. As for our results of the concerned SPP wavelength of around 600 nm, the retrieved resolution is about 12 nm. A higher resolution is reasonably expected by more careful modulation of the relating parameters (e.g. larger NA, longer focal length and etc.).

### *4.2.3 Further Modulation on Focusing*

As we know from discussion in previous chapter, we can use NPM Bragg diffraction method to obtain the wavefronts for any reference directions. Here we can realize SPP focusing with optical axis deviating from the propagation direction. The design schematics in Fig. 4.17a, b correspond to up-inclined and down-inclined focusing, respectively. According to the principle of geometric optics, we can deduce the phase of the nonperiodic nanoarray to a new coordinate $\xi$ (perpendicular to the expected optical axis), which can be written as:

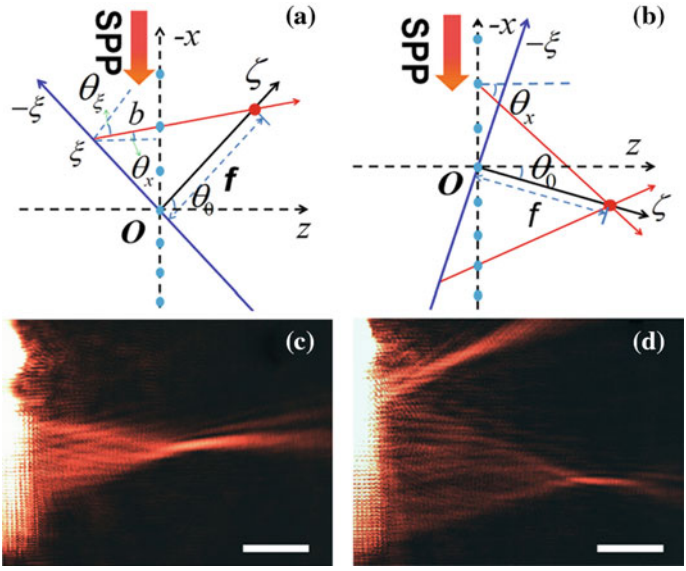


**Fig. 4.17** Schematic diagrams of **a** up-inclined and **b** down-inclined focusing, and the corresponding experimental results of **c** up-inclined and **d** down-inclined focusing. Figure adapted with permission from Ref. [33], ACS

$$\psi(\xi) = \psi(x) - k_{spp}b = k_{spp}x + 2m\pi - k_{spp}b \tag{4.10}$$

Here, $\psi(\xi)$ is the desired phase for focusing.

$$b = -\frac{x\,\tan(\theta_0)}{\cos(\theta_x) + \tan(\theta_0)\sin(\theta_x)} \tag{4.11}$$

is the direct distance from the intersection of the geometric ray and $\xi$ axis to the corresponding structure,

$$\xi = \frac{x}{\cos(\theta_0)(1 + \tan(\theta_x)\tan(\theta_0))} \tag{4.12}$$

$$\sin(\theta_0) = \frac{\lambda_{spp} - a_0}{a_0}, \quad \sin(\theta_x) = \frac{\lambda_{spp} - a_x}{a_x} \tag{4.13}$$

We can obtain the design parameters of the nanoarray as above method by solving $\phi_m(x) = \psi(x)$. Figure 4.17c, d are the experimental results of the SPP focusing. They are SPP focusing with f = 30 μm and upward offset angle of 10° in panel c, and f = 40 μm and downward offset angle of 10° in panel d, respectively, which well realized our design expectation.

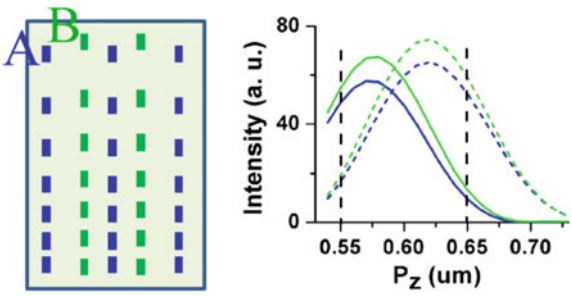


**Fig. 4.18** Schematic diagram of the sublattices. Figure adapted with permission from Ref. [33], ACS

Inspired by the above designs and results, a more flexible wavelength demultiplexer with further improved resolution is proposed. The schematic diagram is shown in Fig. 4.18a, where two sets of sublattice A (blue) and B (green) are included corresponding to two SPP wavelengths of 610 and 570 nm, respectively. According to our phase modulation method, the SPP focusing trajectories will be maintained if the longitudinal lattice parameters ($a_x$) are keeping unchanged, while the focusing intensity will be determined by the lateral lattice period ($p_z$). Figure 4.18b shows the intensity variation of two SPP beams with respect to different lateral period $p_z$, where blue and green curves are intensities corresponding to lattice A and B respectively, and the solid and dotted lines are intensities corresponding to design wavelength 570 and 610 nm respectively. According to the intensity curves, we select 650 nm for lattice A and 550 nm for lattice B as the lateral periods to get a strong intensity contrast at both of the two different wavelengths.

With this idea, we proposed an improved demultiplexer for SPPs with the wavelength of 570 and 610 nm. The design parameters for these two wavelengths and the corresponding experimental image are shown in Fig. 4.19a–c, where the distance between the two focal spots is about 7 μm, much larger than 3 μm in Fig. 4.16.

Moreover, we can use the sublattice structures to realize confocal for SPPs with different wavelengths as well. Figure 4.20a, b are the focusing images of SPPs with free space wavelengths of 633 and 594 nm, respectively, with focal spots designed at the same position. Figure 4.20c is the image in the case of dual-wavelengths, where two focal spots are completely overlapped. Thus the confocal of two wavelengths based on the sublattice structure are well demonstrated.

The realization of the two functions above well demonstrate the flexibility and validity of our sublattice design in beam modulations. However, in this kind of sublattice design more noises are usually introduced compared with the uniform-lattice design as the above results show. In this regard, the uniform and sublattice designs can be selectively adopted for specific design purposes to better fulfill the requirement.

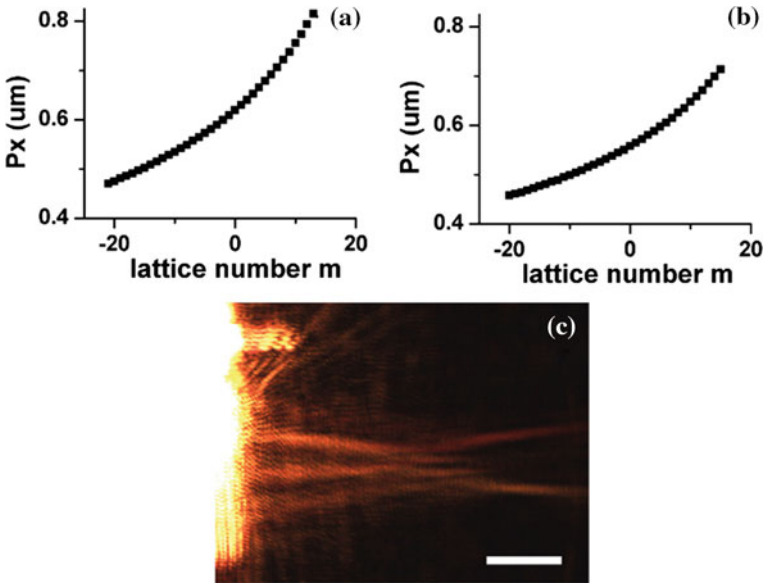


**Fig. 4.19** Improved demultiplexer. **a**, **b** The design parameters for wavelengths of 570 and 610 nm. **c** The corresponding experimental result of the improved demultiplexer

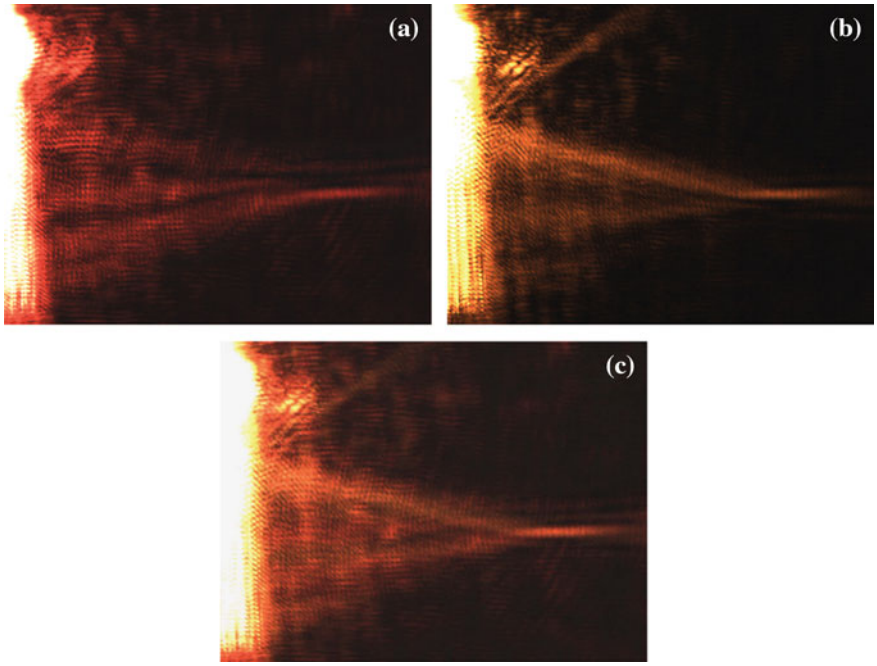


**Fig. 4.20** Confocal of two SPP beams with different wavelengths. Focusing of single SPP beam with **a** $\lambda$ = 633 nm, **b** $\lambda$ = 594 nm, respectively. **c** Results of two incident beams

So far, based on the principle of NPM Bragg diffraction, we have realized SPP focusing completely by in-plane manipulation. This kind of focusing has a broadband effect, which is about 100 nm wide in the visible range. It can also be used as demultiplexer with a resolution as high as 12 nm. Besides, it is flexible to upgrade our uniform design to a sublattice design, which can be used to increase the resolution of the demultiplexer or realize confocal function. All of the results as well as our design schemes will provide significant inspirations for 2D all-optical integrations.

## 4.3 Modulations of SPPs from a Point Source

By far, a lot of SPP functions and SPP beams have been realized, providing inspirations and preparations for SPP manipulations and integrations. However, most of those functions rely on either the out-of-plane coupling process or SPP plane wave incidence. A probable part of future integrated photonic circuits would be such a device that SPPs are generated by the source from one port, then manipulated and injected to another port [34]. For example, SPP can be excited by a quantum dot or a narrow waveguide. In this situation, these SPPs possess nonzero NA and should be regarded as point source instead of plane waves. Thus a method is required to modulate this kind of SPPs generated from point source to realize focusing, various of beams and so on.

We extend the NPM Bragg diffraction method to the SPP from point source [35]. In the previous discussion, we use the NPM Bragg diffraction method to realize phase modulation. In fact, this kind of method is based on planar wavefront as illustrated in Fig. 4.21a. However, according to the principle of diffraction, the method is still valid for the SPPs from a point source, that is, every diffracting unit will produce an extra 2π phase change. But the initial phase of every diffracting unit

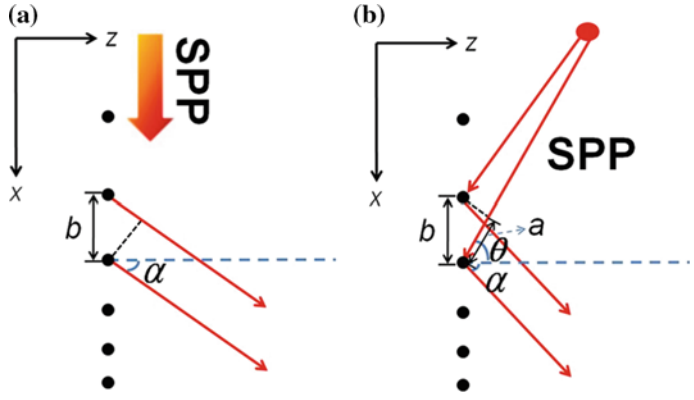


**Fig. 4.21** Schematics of diffraction principle for SPPs from **a** plane-wave, and **b** point source. Figure adapted with permission from Ref. [34], OSA

will be different from that in the case of plane wave incidence. As Fig. 4.12b shows, because of the point source, the initial phase difference of two diffracting units with a distance of b away is: $\Delta\varphi = k_{spp}b\sin\theta$. For two adjacent diffracting units, that is: $\Delta\varphi = k_{spp}b\sin\theta - 2n\pi$, which is $\Delta\varphi = k_{spp}b - 2n\pi$ under plane wave incidence. Here, θ is the intersection angle between incident SPP and z direction, which changes with the locations of the diffracting units as:

$$\sin\theta_n = \frac{x_0 - l_n}{\sqrt{(x_0 - l_n)^2 + z_0^2}} = \frac{x_0 - \sum_n b_n}{\sqrt{\left(x_0 - \sum_n b_n\right)^2 + z_0^2}} \tag{4.14}$$

In which $(x_0, z_0)$ is the location of the point source, $b_n$ is the distance between nth and (n − 1)th units, and $l_n$ is the x coordinate of nth unit. Thus we can obtain the phase evolution in the case of point source as:

$$\varphi_n = \sum_n \Delta\varphi_n = \sum_n k_{spp}b_n \frac{x_0 - \sum_n b_n}{\sqrt{\left(x_0 - \sum_n b_n\right)^2 + z_0^2}} - 2n\pi \tag{4.15}$$

According to this new phase diffraction law, we can design all kinds of point source based nanostructures to realize beam modulations that we need.

First, we would demonstrate the focusing of SPPs from one point source ($O_1$) to another point ($O_2$) by our designed structure. The schematic diagram is shown in Fig. 4.22a. We first calculated the horizontal positions ($z_m$) of the nanoarray along z axis (x = 0) according to the phase modulation method for plane waves as mentioned before. Under this arrangement, we can focus the SPPs propagating along z axis to $O_1$. Such SPPs can be considered as beams emitted by $O_2$ and propagate along z axis. According to the principle of reciprocity, it is easy to get that all SPPs emitted from $O_1$ will have the same phase (or phase difference of $2m\pi$) when they pass through $O_2$. Then we got the positons of nanoarray at the line of $z = z_m$ by solving $\varphi_n = \Psi(x)$, where $\varphi_n$ is the phase evolution of the SPPs from point source after passing through the structure and $\Psi(x) = -k_{spp}x^2/2(f_0 - z_m)$ is the phase evolution for focal length of $(f_0 - z_m)$. Here, $f_0$ is the focal length of the entire structure measuring from $z = z_c$. So that all the SPPs excited by point source $O_1$ will focus to $O_2$ after diffracting by the nanocaves of all lines and the focus of every line will have the same phase, finally realizing the focusing of SPP beams from point source $O_1$.

In experiments, we fabricated the well-designed nanohole array by FIB on a silver film. A series of concentric circle grooves are designed to couple the incident laser beam to the SPP beam, which works as the SPP point source. Figure 4.22b is the SEM image of the sample with a datum line of $z_c = 5$ μm and a focal length of $f_0 = 30$ μm. The concentric circle grooves with inner circle radius of 3 μm and incremental of 610 nm are centered (the location of the point source) at $z_0 = 0$ μm, $x_0 = -25$ μm, which are used to couple the incident He–Ne laser beam with a

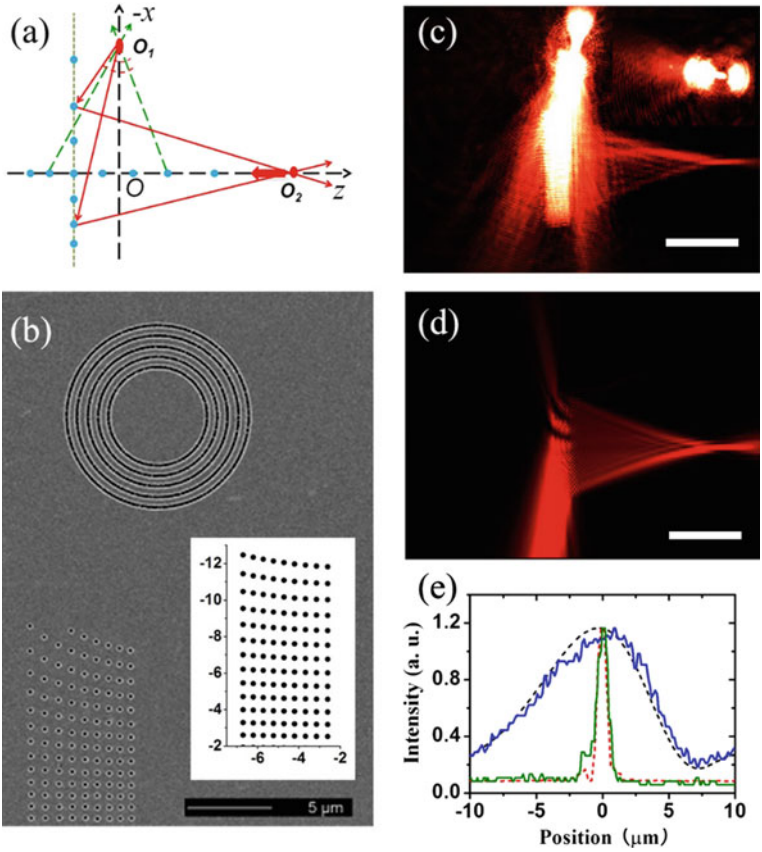


**Fig. 4.22** SPP focusing from a point source. Figure adapted with permission from Ref. [34], OSA

wavelength of 633 nm to SPP beams. The coupling result is shown in the inset of Fig. 4.22c, which is similar with the circular wave generated by point source. Each nanohole has a diameter of 240 nm and a depth of 20 nm. The propagation of SPPs detected by LRM system is shown in Fig. 4.22c, which agrees well with the corresponding theoretical calculation result based on Huygens–Fresnel Principle (as shown in Fig. 4.22d). As in Sect. 4.2, we plot the longitudinal and transverse profiles of the focal spot in Fig. 4.22e, which is as good as the previous focusing result based on plane wave, demonstrating the realization of SPP focusing from a point source.

Notably, the realized focusing here exists only at one side of the designed structure which is quite different from the focusing with symmetrical focal spots on both sides of the structure in Sect. 4.2. This is a unique unidirectional SPP focusing design based on a structure with an almost rectangle shape. Thus the focal intensity is much higher than that of the previous bidirectional focusing design based on plane wave at the same condition, which is quite useful in restraining the power consumption and would have practical significance in optical integrations.

With this method, we can also realize previous-mentioned nondiffracting, self-accelerating Airy beam from a point source. Based on the previous results, we know that the critical condition to generate Airy beam is the 1.5-power phase distribution. With the corresponding phase evolution of a point source, we can obtain the design parameters by solving $\varphi_n = \Psi(x)$, where

$$\psi(x) = -\frac{2}{3}\left(-\frac{x}{x_a}\right)^{3/2} - \frac{\pi}{4} \tag{4.16}$$

is the phase distribution of Airy beam and $x_a$ = 1.08 μm is a scale factor same as that in Sect. 2.2. The point source is located at $z_0$ = 5 μm, $x_0$ = −25 μm. The calculated vertical positions along x direction are shown in Fig. 4.23c and the horizontal period is set as $P_z$ = 520 nm to get the proximate amplitude distribution of the Airy beam. Next, theoretical calculation based on Huygens–Fresnel principle and corresponding experiments were performed. The results are shown in Fig. 4.23a, b, respectively, which are in good agreement with each other. The experimental trajectory of the main lobe and the parabolic trajectory of an ideal Airy beam are plotted together in Fig. 4.23d, which are in good coincidence, indicating the realization of plasmonic Airy beam from point source.

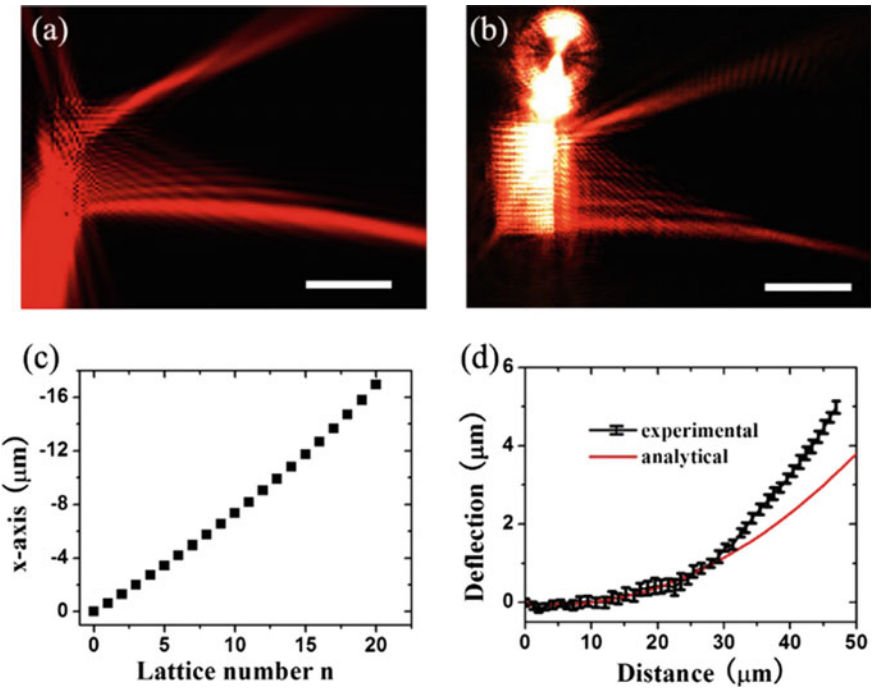


**Fig. 4.23** The realization of plasmonic Airy beam from point source. Figure adapted with permission from Ref. [34], OSA

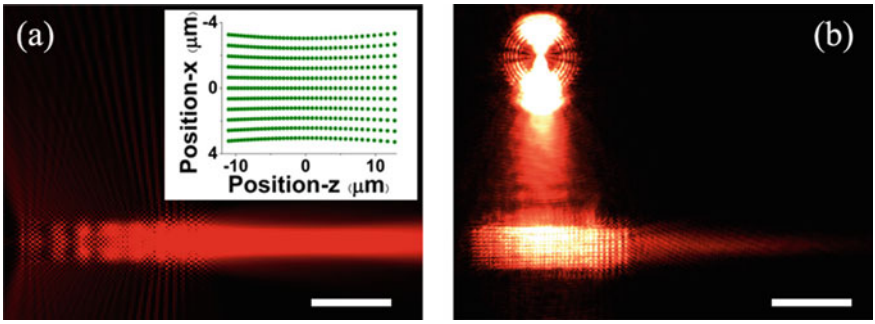


**Fig. 4.24** The realization of finite SPP plane wave from point source. Figure adapted with permission from Ref. [34], OSA

Finally, we demonstrated the realization of a finite SPP plane wave from a point source based on the above method. A plane wave is a constant-frequency wave with parallel wavefronts normal to the propagation direction. What we realized here is a plane wave propagating along z direction with a finite wavefront. The design process is similar with the previous realized focusing from point source. We first get the structure positions $z_m$ at the axis of x = 0 according to the principle of reciprocal. Then the structure positions at the line of $z_m$ are determined by solving $\varphi_n = \Psi(x)$, where $\Psi(x)$ is the phase distribution of a plane wave written as $\Psi(x) = 0$. The designed parameters for point source at $x_0 = -30$ μm, $z_0 = 0$ μm are shown in the inset of Fig. 4.24a. Similarly, we carried out theoretical calculations and experiments, which are shown in Fig. 4.24a, b, respectively. In spite of the intensity attenuation of the experiment result due to the propagation loss of SPP, the theoretical and experimental results are in good agreement, indicating the realization of finite SPP plane wave from point source.

In conclusion, we successfully extended the in-plane phase modulation method for plane wave incidence to the case of point source incidence, and realized SPP focusing, Airy beam and finite plane wave with the SPP from a point source. Furthermore, different from the previous demonstrated bidirectional focusing and Airy beam, all the realized beams here are unidirectional, indicating the beneficial of our design in power consumption. All of the above results indicate the extensibility and generality of our in-plane phase modulation method in other systems. The method together with the above achieved functions are expected of promising applications in future beam manipulations and optical integrations.

## 4.4 Conclusion

In this chapter, the physical intension and applications of the non-perfectly matched Bragg diffraction method were further revealed. With this method, we realized collimated SPP beams. We also proposed our understanding on a source-to-beam

relationship, with which we came up with a method to realize intensity controllable beams, such as lossless and exponential increasing SPP beams. Furthermore, we extended the method to beams generation with curve trajectories, realizing non-monotonical beams and successfully restraining the background noise at the inflection points of the SPP beams. We also achieved broad band SPP focusing, which can be used as demultiplexer with high resolution. All the methods and results can be extended to SPPs of other forms such as point source, indicating the generality of our method. Moreover, we showed the flexibility of our phase modulation method in designs and applications. Focusing with inclined optical axis and improved demultiplexer are such examples that fully demonstrate the usefulness and capacity of the NPM diffraction method. The methods and results in this chapter are totally 2D based, which have more application possibilities in future optical integrations than the common cases relying on out-of-plane coupling processes. All of these methods and results provide us good references and preparations in optical integrations and manipulations.

## References

1. Veldkamp WB, Mchugh TJ (1992) Binary Optics. Sci Am 266:92–97
2. Yu NF, Genevet P, Kats MA, Aieta F, Tetienne JP, Capasso F, Gaburro Z (2011) Light propagation with phase discontinuities: generalized laws of reflection and refraction. Science 334:333–337
3. Li L, Li T, Wang SM, Zhang C, Zhu SN (2011) Plasmonic airy beam generated by in-plane diffraction. Phys Rev Lett 107:126804
4. Zhang P, Hu Y, Li T, Cannan D, Yin X, Morandotti R, Chen Z, Zhang X (2012) Nonparaxial Mathieu and Weber accelerating beams. Phys Rev Lett 109:193901
5. Zhang P, Hu Y, Cannan D, Salandrino A, Li T, Morandotti R, Zhang X, Chen Z (2012) Generation of linear and nonlinear nonparaxial accelerating beams. Opt Lett 37:2820–2822
6. Froehly L, Courvoisier F, Mathis A, Jacquot M, Furfaro L, Giust R, Lacourt P, Dudley J (2011) Arbitrary accelerating micron-scale caustic beams in two and three dimensions. Opt Express 19:16455–16465
7. Greenfield E, Segev M, Walasik W, Raz O (2011) Accelerating light beams along arbitrary convex trajectories. Phys Rev Lett 106:213902
8. Epstein I, Arie A (2014) Arbitrary bending plasmonic light waves. Phys Rev Lett 112:023903
9. Arlt J, Dholakia K (2000) Generation of high-order Bessel beams by use of an axicon. Opt Commun 177:297–301
10. Lin J, Dellinger J, Genevet P, Cluzel B, De Fornel F, Capasso F (2012) Cosine-Gauss plasmon beam: a localized long-range nondiffracting surface wave. Phys Rev Lett 109:093904
11. Li L, Li T, Wang SM, Zhu SN (2013) Collimated Plasmon Beam: nondiffracting versus linearly focused. Phys Rev Lett 110:046807
12. Kaminer I, Bekenstein R, Nemirovsky J, Segev M (2012) Nondiffracting accelerating wave packets of Maxwell's equations. Phys Rev Lett 108:163901
13. Aleahmad P, Miri M-A, Mills MS, Kaminer I, Segev M, Christodoulides DN (2012) Fully vectorial accelerating diffraction-free Helmholtz beams. Phys Rev Lett 109:203902
14. Chen Y-H, Huang L, Gan L, Li Z-Y (2012) Wavefront shaping of infrared light through a subwavelength hole. Light: Sci Appl 1:e26

15. Ozaki M, Kato J-I, Kawata S (2011) Surface-plasmon holography with white-light illumination. Science 332:218–220
16. Dolev I, Epstein I, Arie A (2012) Surface-plasmon holographic beam shaping. Phys Rev Lett 109:203903
17. Yin L, Vlasko-Vlasov VK, Pearson J, Hiller JM, Hua J, Welp U, Brown DE, Kimball CW (2005) Subwavelength focusing and guiding of surface plasmons. Nano Lett 5:1399–1402
18. Kiyan R, Reinhardt C, Passinger S, Stepanov AL, Hohenau A, Krenn JR, Chichkov BN (2007) Rapid prototyping of optical components for surface plasmon polaritons. Opt Express 15:4205–4215
19. Chen Y-G, Chen Y-H, Li Z-Y (2014) Direct method to control surface plasmon polaritons on metal surfaces. Opt Lett 39:339–342
20. Steele JM, Liu Z, Wang Y, Zhang X (2006) Resonant and non-resonant generation and focusing of surface plasmons with circular gratings. Opt Express 14:5664–5670
21. Volkov VS, Bozhevolnyi SI, Rodrigo SG, Martin-Moreno L, García-Vidal FJ, Devaux E, Ebbesen TW (2009) Nanofocusing with channel plasmon polaritons. Nano Lett 9:1278–1282
22. Ropers C, Neacsu C, Elsaesser T, Albrecht M, Raschke M, Lienau C (2007) Grating-coupling of surface plasmons onto metallic tips: a nanoconfined light source. Nano Lett 7:2784–2788
23. Choi H, Pile DF, Nam S, Bartal G, Zhang X (2009) Compressing surface plasmons for nano-scale optical focusing. Opt Express 17:7519–7524
24. Wang J, Zhang J, Wu X, Luo H, Gong Q (2009) Subwavelength-resolved bidirectional imaging between two and three dimensions using a surface plasmon launching lens. Appl Phys Lett 94:081116
25. Zhao C, Zhang J (2009) Binary plasmonics: launching surface plasmon polaritons to a desired pattern. Opt Lett 34:2417–2419
26. Feng L, Tetz KA, Slutsky B, Lomakin V, Fainman Y (2007) Fourier plasmonics: Diffractive focusing of in-plane surface plasmon polariton waves. Appl Phys Lett 91:081101
27. Fang Z, Lin C, Ma R, Huang S, Zhu X (2009) Planar plasmonic focusing and optical transport using CdS nanoribbon. ACS Nano 4:75–82
28. Laux E, Genet C, Skauli T, Ebbesen TW (2008) Plasmonic photon sorters for spectral and polarimetric imaging. Nat Photonics 2:161–164
29. Diest K, Dionne JA, Spain M, Atwater HA (2009) Tunable Color Filters Based on Metal–Insulator–Metal Resonators. Nano Lett 9:2579–2583
30. Zhao CL, Zhang JS (2010) Plasmonic demultiplexer and guiding. Acs NANO 4:6433–6438
31. Tanemura T, Balram KC, Ly-Gagnon D-S, Wahl P, White JS, Brongersma ML, Miller DA (2011) Multiple-wavelength focusing of surface plasmons with a nonperiodic nanoslit coupler. Nano Lett 11:2693–2698
32. Drezet A, Koller D, Hohenau A, Leitner A, Aussenegg FR, Krenn JR (2007) Plasmonic crystal demultiplexer and multiports. Nano Lett 7:1697–1700
33. Li L, Li T, Wang SM, Zhu SN, Zhang X (2011) Broad band focusing and demultiplexing of in-plane propagating surface plasmons. Nano Lett 11:4357–4361
34. Briggs RM, Grandidier J, Burgos SP, Feigenbaum E, Atwater HA (2010) Efficient coupling between dielectric-loaded plasmonic and silicon photonic waveguides. Nano Lett 10: 4851–4857
35. Li L, Li T, Wang SM, Zhu SN (2012) Steering plasmon beam from a point source. Opt Lett 37:5091–5093

# Chapter 5
# Far-Field Beam Modulations by Plasmonic Structures

SPPs are beneficial to spatial field modulations in the micro-nano scale due to their subwavelength property and field confinement abilities, which are superior in integration and device miniaturization than traditional optical elements like lenses, spatial light modulators and so on. Thus spatial beam modulations by SPPs have attracted great research enthusiasm. In fact, the NPM phase modulation method utilizing the diffractions of plasmonic micro-structures not only work for the in-plane optical fields, but also work for the out-of-plane optical fields scattered by these structures, with which we can also achieve spatial beam modulations.

Optical vortex is an very important and interesting research field of optics. In 1989, Coullet et al. first proposed the concept of "optical vortices" [1]. In 1992, Allen et al. demonstrated that light beams with an phase dependence of $exp(in\theta)$ carry an orbital angular momentum (OAM) equal to $n\ \hbar$ under the paraxial approximation (that is optical vortex) [2], which began to attract people's great interests on optical vortices and provided theoretical foundations for the future applications of OAM of optical vortices. In 1994, they demonstrated that the OAM was also equal to $n\ \hbar$ even at the non-paraxial situation [3]. Later, the optical vortex beams were applied to numerous areas, such as optical manipulations [4, 5], optical computations [6], especially in the area of optical communications [7–9], where the optical vortex beams provide new degrees of freedom and greatly improve the information capacity. Optical vortex is being a research focus in optical communication since then. To achieve more integrated optical vortex beams with subwavelength, plasmonic structures must bring new vitalities into the research and applications with this kind of beams.

Unlike beams in free space, the SPP modes include two parts: transverse field and longitudinal field, which carry quite different properties, especially in the situation of being scattered by micro/nano structures into space: much of the transverse field is still bound to the metal surface, while the longitudinal field is scattered into space [10]. This property makes SPPs quite unique in spatial field modulations, providing wide space and new methods for the polarization modulations to the spatial beams.



L. Li, *Manipulation of Near Field Propagation and Far Field Radiation of Surface Plasmon Polariton*, Springer Theses,
DOI 10.1007/978-981-10-4663-6_5

In this chapter, we will first discuss the NPM phase modulation method in the conversion of the SPPs and the spatial beams. It is followed by the OAM beam generation with this method. We propose a phase modulation in the radial direction so that to integrated tune the properties of the realized OAM beam, such as non-diffraction, focusing, off-axial ejection, splitting, and so on. At last, we propose a plasmonic polarization generator that can reconfigure an input polarization to all kinds of states based on the interference of the in-plane (longitudinal) field of the SPPs. With a well-designed nanohole array, the in-plane field of SPPs with proper polarization states and phases can be selectively scattered out to form desired light beams in the free space, such as the plane wave, focusing or Airy beams, and so on. More importantly, the scheme provides a new dimension of polarization control, which can co-work with other polarization control systems (such as the coupling system, metasurface etc.).

## 5.1 The Conversion Between SPPs and Spatial Beams

In recent years, spatial beam modulations using plasmonic structures have become a popular research subject. Since the pioneer work of beam focusing with metal bull's eye structure [11], plasmonic structures were used to tailor radiation beams to realize collimation, focusing [12], even holographic imaging [13, 14] and modulations of fluorescence emission [15, 16]. Compared with traditional modulation methods, the plasmonic based modulation can be achieved in much smaller scale, instead of occupying a large space, like lenses, SLM and so on, due to the high confinement and subwavelength properties of the SPPs.

We have already demonstrated the high effectiveness of our NPM diffraction method in in-plane modulations in the previous discussion, which can be extended to spatial beam modulations as well. With this method, spatial Airy beam with a 1.5-power phase distribution was realized in our previous work [17]. The phase distribution for spatial beam modulation with nanoarray on metal surface is written as:

$$\phi_n(x) = \phi_0 + k_{spp}x - 2n\pi \tag{5.1}$$

Which is completely the same with the in-plane phase evolution. But for spatial beam engineering, the required phase distribution corresponds to the free space wavelength instead of SPP wavelength in the case of in-plane, which should be noticed when using plasmonic structures to modulate spatial beams.

## 5.2 The Realization and Modulation of Optical Vortex Beams by Plasmonics

### 5.2.1 Optical Vortex Beams

As we all know, a photon in natural space carries a linear momentum of $\hbar k_0$. It carries a spin angular momentum (SAM) of $\pm\hbar$ if it is right hand or left hand circular polarized. In 1992, Allen et al. demonstrated that light beams with an azimuthal phase dependence of $exp(in\theta)$ will carry orbital angular momentum (OAM) of $n\hbar$ [2], which can be much larger than the spin angular momentum (n is an arbitrary integer and θ is the azimuthal coordinate). Different from ordinary circular polarized beams, OAM beams have helical phase fronts as shown in Fig. 5.1, with the number of helices and handedness determined by the topological number $n$. It's easy to get that the Poynting vector, which is perpendicular to the wavefront plane, always has azimuthal component and thus cause the existence of OAM [18].

The electric field of a light beam propagating along z axis with topological number n can be written as:

$$E(r,\theta,z) = E_0(r,\theta,z)\exp(in\theta)\exp(-ikz) \tag{5.2}$$

where $E_0(r,\theta,z)$ is the amplitude at position z. From the expression, we can see that the electric field has a azimuthal phase of $exp(in\theta)$ and a phase change of $2n\pi$

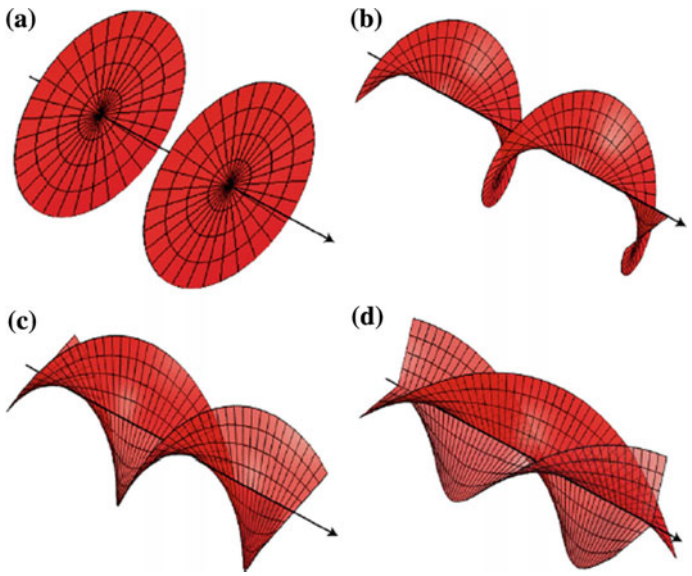


**Fig. 5.1** The phase fronts of OAM beams with **a** n = 0, **b** n = 1, **c** n = 2, **d** n = 3. Figure adapted with permission from Ref. [18], OSA

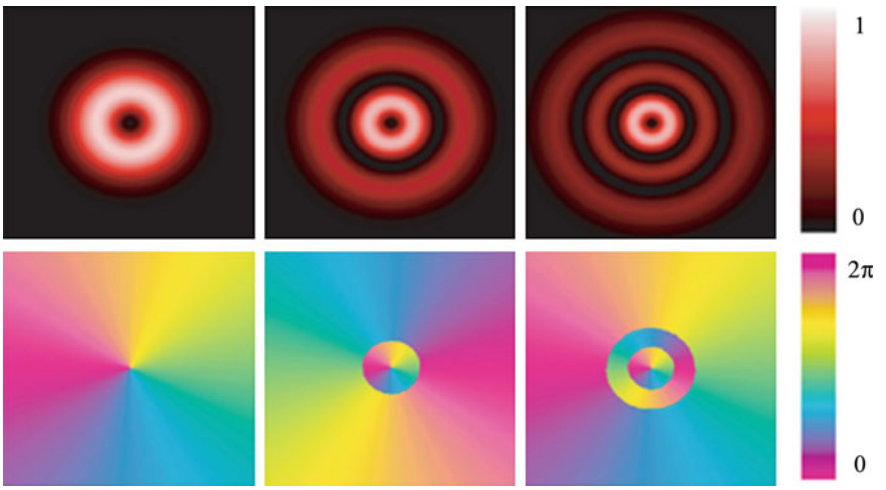


**Fig. 5.2** The intensity and phase profiles of Laguerre-Gaussian beams: LG01, LG11 and LG21 from *left* to *right*. Figure adapted with permission from Ref. [18], OSA

around the vortex center. At the center of the helix there is a phase singularity, where the amplitude is zero and thus no energy exists. Different light fields of OAM beams will lead to different modes. The most common mode of which is Laguerre-Gaussian mode [19]:

$$LG_{pl} = \sqrt{\frac{2p!}{\pi(p+|l|)!}}\frac{1}{w(z)}\left[\frac{r\sqrt{2}}{w(z)}\right]^{|l|}\exp\left[\frac{-r^2}{w^2(z)}\right]L_p^{|l|}\left(\frac{2r^2}{w^2(z)}\right)\exp(il\theta)$$
$$exp\left[\frac{ikr^2z}{2\left(z^2+z_R^2\right)}\right]\exp\left[-i(2p+|l|+1)\tan^{-1}\left(\frac{z}{z_R}\right)\right]$$

where $w(z) = w(0)\left[\left(z^2+z_R^2\right)/z_R^2\right]^{1/2}$ is the beam waist of a Gaussian beam with an initial phase of $w(0)$ at position z and $z_R$ is the Rayleigh radius. $l$ and $p$ are the quantum numbers to characterize the modes: $l$ is the azimuthal quantum number representing a photon with an OAM of $l\hbar$; $p$ is the radial quantum number representing a beam with concentric rings with the number of $(p + 1)$. Figure 5.2 shows the phase distributions and light intensities of several Laguerre-Gaussian modes.

Different from SAM (carried by circular polarized beams) with only two orthogonal states, OAM can have unlimited ones theoretically, providing more freedom for optical communicating and enlarging the communication capacity greatly, thus becomes one of the hot topics in applied research field [7, 8, 20–22] and also attracting a lot of attention in the field of quantum information [23, 24]. The traditional methods to generate OAM beams utilize large optical elements, such as spiral phase plate, lenses, SLMs and so on, which cannot satisfy people's requirements to generate and control OAM beams in a much smaller scale with the development of all-optical integrations. People have been trying to generate OAM beam with more compact structures as well as the function integration.

Cai et al. demonstrated a method to generate OAM beams by grating in an integrated silicon microcavity with a radius of only 3.9 μm [25]. Arie's group utilized QPM with nonlinear crystals to generate OAM beams compactly [26]. Capasso's group demonstrated phase modulation method with metasurface and generated OAM beam with a thin metasurface [27]. They also integrated fork metal gratings onto a silicon detector, realizing OAM detection with SPPs [13]. Zhan's group realized OAM beams at micron scale using Archimedes spiral structures [28] and further modulated the direction of the achieved OAM beams by changing the relative positions of the quantum dots to the spiral structure [29]. There're some works to generate OAM beams with propagating SPPs. Arie's group designed fork gratings with holography on metal surface to scatter the propagating SPPs into far-field OAM beams [30]. Ebbesen's group also used metal spiral structure to generate OAM beams near the metal surface. In addition, different from the previous mentioned methods to generate near-field OAM beams, their structure is able to radiate the OAM beams to far field [31].

### 5.2.2 *The Realization of Optical OAM Beams by Plasmonic Structures*

In fact at almost the same time of the work of Ebbesen's group, we demonstrated a similar method to generate OAM beams. Different from their work, we integratedly introduced phase design in radial direction to further modulate the generated OAM beams, so that to achieve more flexible modulations.

In our previous work [17], our nonlinear phase modulation method is still applicable to spatial beam modulations and the corresponding phase distributions satisfy Eq. 5.1 for 1D. To get phase modulation in 2D, we only need to arrange the phase distribution at the 2D planer. For OAM beams, a phase distribution of $\psi(r,\theta) = \psi(r) + n\theta$ is required, in which $r$ and $\theta$ are the radial and azimuthal coordinates, respectively, $n$ is the arbitrary integrator and $\psi(r)$ is the radial phase distribution. As it was introduced above, such phase distribution can generate an OAM beam with the topological number of n. Meanwhile, the profile of the achieved OAM beams can be modulated as needed by designing $\psi(r)$. However, in Ebbesen's group's work, the structure along radial direction is just a grating with a period of the wavelength of the SPP. Thus the formed beams in their work are similar with Gaussian beams, which will diverge gradually when radiating from the metal surface to far-filed.

Figure 5.3b is the typical structure we designed. A nanohole with a diameter of 150 nm was fabricated through a Silver film with thickness of 200 nm in the origin of coordinates to generate a point SPP source. The positions of the radial structures along different direction $\varphi$ are calculated by solving Eq. 5.1, which satisfies $\phi_n(r, \varphi) = \psi(r, \varphi)$ with $\phi_n(r, \varphi) = \phi_n(r)$. Finally a grating structure is formed as shown in Fig. 5.3b by connecting these discrete points successively. In experiment, the depth of the grating was 50 nm.

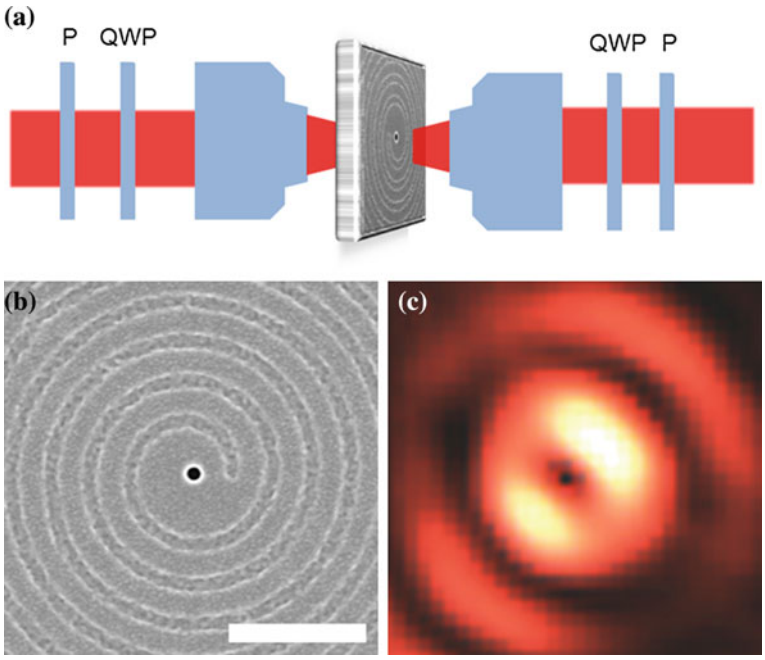


**Fig. 5.3** Experimental realization of OAM beam. **a** The experimental measurement set up. **b** The SEM image of the sample. **c** Experimental image of the typical OAM beam with n = 1

Figure 5.3a shows the schematic diagram of our experimental set up. The incident laser modulated by a polarizer and a quarter-wave plate incidents into the nanohole from the substrate of the sample through a 50× microscope objective to generate SPPs, which are then scattered by the spiral grating. The scattered light is then collected by a 100× microscope objective, detected by a quarter-wave plate and a polarizer, and finally imaged by a CCD camera. Figure 5.3c is the experimental image of an OAM beam with topological number of 1 in the case of 633 nm incidence, where a hollow donut-shaped beam is clearly presented.

We also performed theoretical calculation based on Huygens-Fresnel principle to estimate the result of our design. A series of points on the spiral structure are evenly selected as the sub-sources, which uniformly radiate spherical waves to the space and mutual interfere to form the final beams. According to this, the electric field at any point in space can be written as:

$$E_{tot}(x, y, z) = E_0 \sum_{m,n} \frac{\cos \vartheta}{r_{m,n}} \exp[i(k_{spp} R_{m,n} + k_0 r_{m,n})] \tag{5.3}$$

with $E_0$ the intensity of every sub-source $O_{m,n}$, $R_{m,n}$ the distance from the sub-source to the origin, $r_{m,n}$ the distance from sub-source to the point $P(x, y, z)$, and $\theta$ the intersection angle between ray $O_{m,n}P$ and $OP$. Usually $R_{m,n}$ is small enough for us to ignore the propagation loss of SPPs. Figure 5.4 shows the

calculated result, which agrees well with the experimental result (Fig. 5.3c), indicating the validity of the method in predicting the field distribution in 3D space.

The intensity of the directly transmitted light through the nanohole is comparable with the scattered light, leading to mutual interference and influence the field distribution of the final beam. The field distribution in this case was calculated by the above method as well. A spherical-wave source with an intensity of 100 times of the sub-source on the grating was located at the center, representing the directly transmitted light through the nanohole, which interfered with the beam generated by the structure with topological number of 2. The calculated result is shown in Fig. 5.5a, where a spiral shape with two arms is clearly seen. The experimental

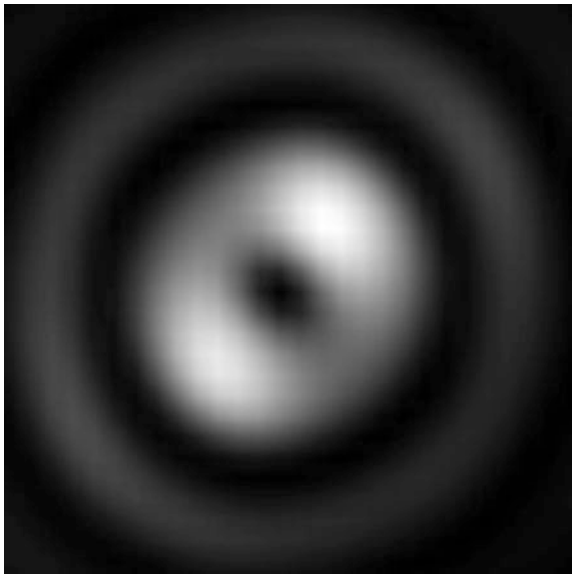

**Fig. 5.4** Calculated OAM beam with n = 1 by Huygens-Fresnel principle

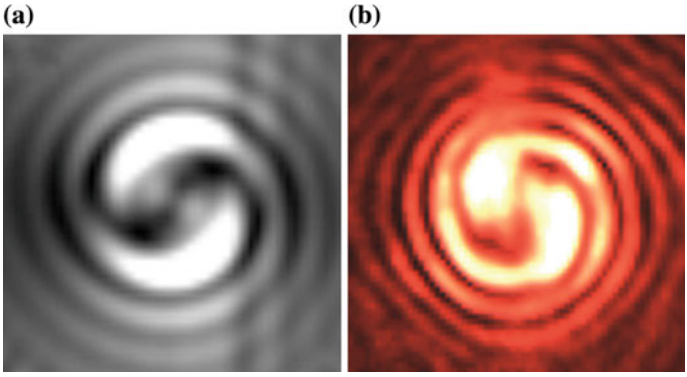


**Fig. 5.5** **a** The theoretical and **b** experimental results of the interference image between a spherical wave and an OAM beam with n = 2

image of the same structure near the metal surface is shown in Fig. 5.5b, which is consistent with the calculation result, indicating the practical existence of such interfered field distribution. With the increase of the distance from the surface, the directly transmitted light will diverge soon and its disturbance to the OAM beams will decrease rapidly. On the other hand, in Fig. 5.5 we noticed that the number of the arms of the light field after interference is equal to the topological number of the OAM, which provide us a convenient method to verify the generated OAM beams and their topological number.

### 5.2.3 The Modulations of OAM Beams

Our phase modulation method can not only modulate the azimuthal phase distribution but also modulate the radial phase distribution $\psi(r)$ to achieve beams for more practical applications. As we mentioned above, the OAM beam generated by the grating with the period of SPP wavelength will diverge gradually, which will be a disadvantage in practical applications. As we all know, however, the Bessel beam is a kind of nondiffraction beams and its high order beam is the OAM beam. Besides a certain phase distribution along the azimuthal direction, a linear phase relationship along the radial direction is required, which can be written as $\psi(r) = -ar$, with $-a$ the negative slope. Then the total phase distribution can be written as $\psi(r, \theta) = -ar + n\theta$. Usually, the zero-order Bessel beam can be realized by conical mirror. Here we used the phase modulation method mentioned above to achieve a nondiffraction OAM beam. By solving $\phi_n(r, \theta) = \psi(r, \theta)$, we got a series of discrete scattering units. Due to the linear radial phase distribution, the obtained diffracting units are periodically distributed, which are connected successively to form a periodic spiral grating. Here, we set $a \approx 1.34\ \mu m^{-1}$ (corresponding to a grating with a period of 540 nm) and topological number of n = 1. The spiral grating has a radius of 15 μm, which can generate a nondiffraction first-order Bessel beam in the range of 110 μm from the metal surface.

Figure 5.6a–c are the theoretical results at the positions of 50, 80 and 100 μm away from the original plane, respectively. As we can see from the figures that the inner circle of the achieved OAM beam is almost unchanged, with a diameter of about 3 μm. Figure 5.6d–f are the experimental results at the corresponding positions, which are well consistent with the theoretical results, indicating the well realization of the nondiffraction OAM beams by our method. Since the OAM of the beams can be transferred to particles to manipulate them, this kind of beams can be regarded as a series of hollow probes with preserved diameters, inserting into substances or organisms to moving, rotating particles or medicals inside noninvasively [5], which are quite valuable in practical applications.

Among real applications, the OAM beams are usually needed to be focused to make optical manipulating, information processing and so on. Thus focusing is one of the frequently-used operations to OAM beams. We can utilize this process through the modulating of the radial phase. Here the radial phase should satisfy the

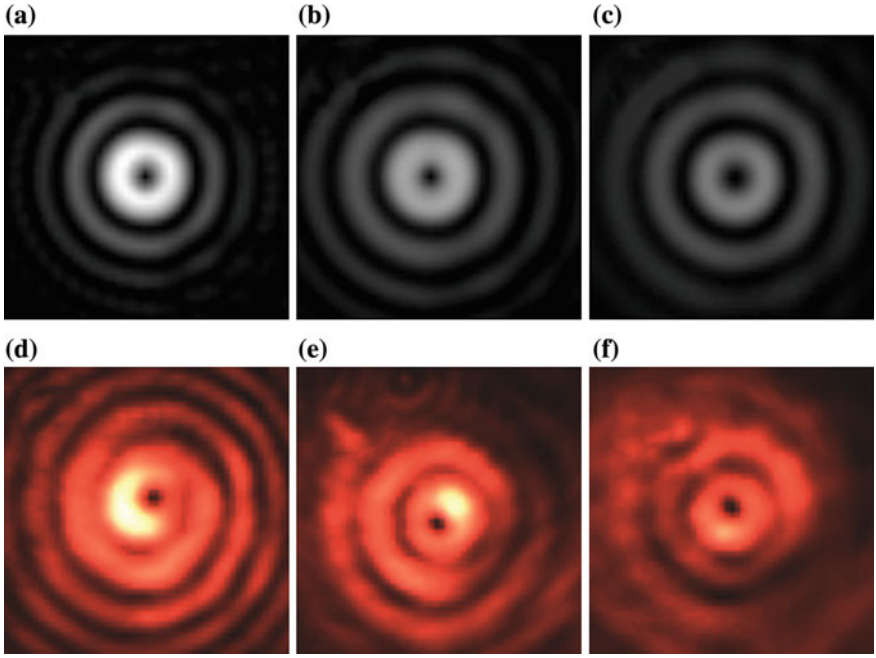


**Fig. 5.6** Non-diffraction OAM beam. The theoretical calculated field distributions at the positions of **a** 50 μm, **b** 80 μm, and **c** 100 μm for OAM beam with n = 1 and **d**–**f** are the corresponding experimental results

phase requirement for focusing, that is $\psi(r) = -k_0 r^2/f$, in which $f$ is the focal length of the OAM beam in space, $k_0$ is the wave vector of the incident laser in free space. With the same method discussed above, we got the corresponding design by solving $\phi_n(r, \theta) = \psi(r) + n\theta$. $f$ was set to be 40 μm and the obtained structure was an aperiodic spiral grating. Figure 5.7a–c are the theoretical field distributions at the positions of 30, 40, and 50 μm from the original plane, respectively and Fig. 5.7d–f are the experimental images at the corresponding positions, which are in good agreement with the former ones. From these results, it is easy to get that the smallest beam diameter and the highest beam intensity appear at the position of 40 μm, indicating the realization of focusing of our designed structure. Meanwhile, the contrast between the inner circle and the outer circles is much higher in the focusing case compared with the nondiffracting result, thereby the accuracy of optical manipulation and information processing will get improved.

In the previous discussion about the 2D in-plane process, our phase modulation method can be used to realize off-axial beams with different exit angles flexibly. The method is also applicable in achieving OAM beams and will be much valuable in practical applications. The angle between the target OAM beam and normal of the metal surface is supposed to be$\gamma$. In this case, the corresponding phase evolution at the metal surface is $\psi(r, \phi) = \psi(r) + n\phi + k_0 r \sin\gamma \cos\phi$ [32], in which $\psi(r)$ is

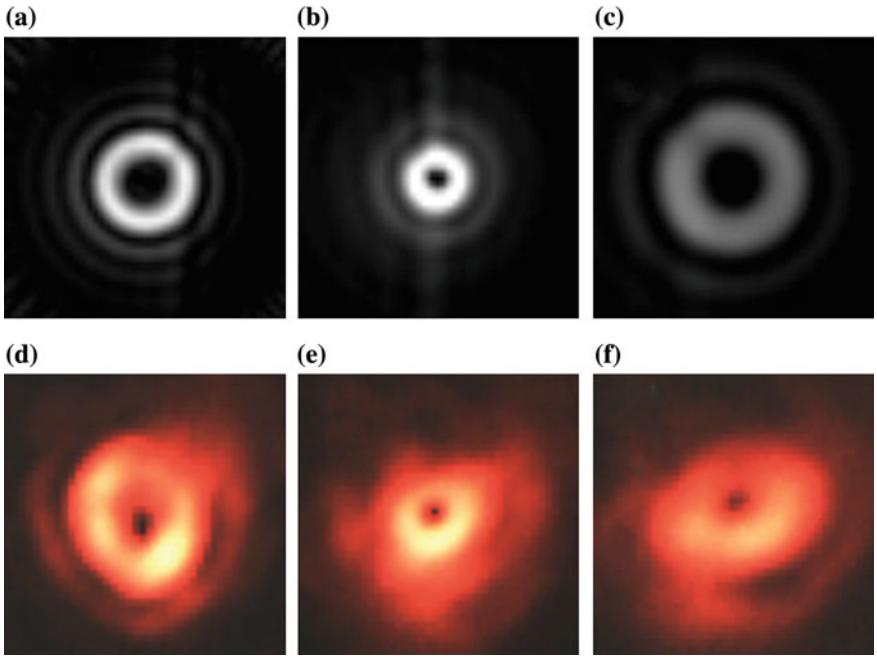


**Fig. 5.7** Focusing OAM beam. Theoretical field distributions at positions of **a** 30 μm, **b** 40 μm and **c** 50 μm, and **d**–**f** the corresponding experimental result

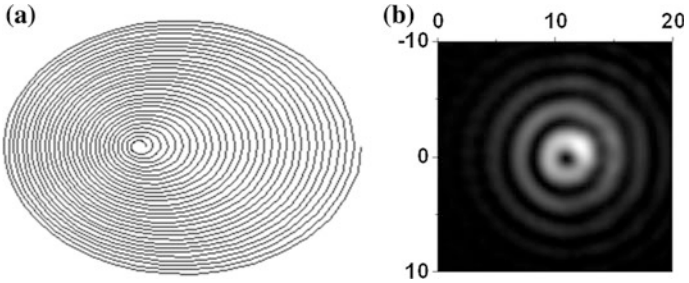


**Fig. 5.8** Off-axis OAM beam. **a** Design pattern for generation of off-axis OAM beam. **b** The calculated field distribution at the position of 50 μm from the surface

the arbitrary radial phase distribution. By solving $\phi_n(r, \theta) = \psi(r, \theta)$ we can get the required design. Figure 5.8a is the design pattern under the conditions of $\gamma = 12°$, topologic number of n = 1, and a linear radial phase distribution for a Bessel beam. Figure 5.8b is the theoretical result at 50 μm away from the metal surface. The central singularity deviates from the design center (0, 0) of about 10 μm along the horizontal direction, which is consistent with our expectation, indicating the effectiveness and accurateness of our off-axis design method for OAM beams.

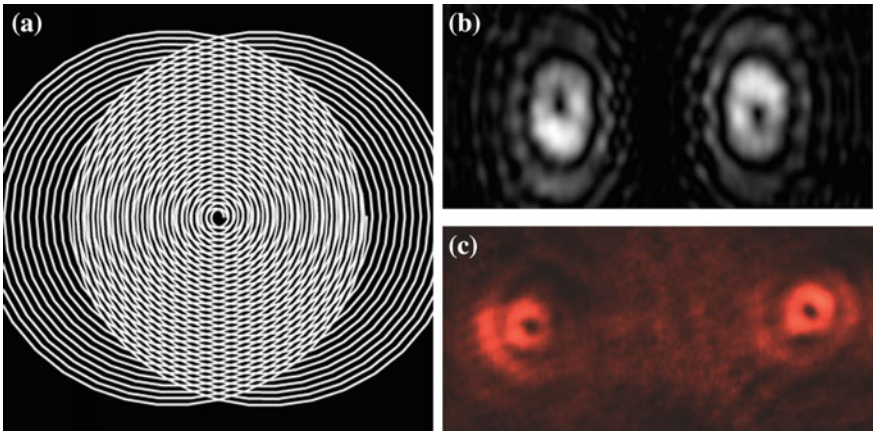


**Fig. 5.9** OAM beam splitter. **a** The design pattern. **b** The theoretical and **c** The experimental results of the splitted OAM beams

Furthermore, a beam splitter of OAM beam is demonstrated based on the off-axis design. From the design pattern in Fig. 5.8a, we can see that the design pattern is not a quasisymmetrical spiral any more, which is different from the previous designs. The asymmetry allows spatial multiplexing on the metal surface. By the design method of spatial multiplexing, it is possible to achieve a beam splitter and the separated beams could carry different information such as topological numbers, beam profiles and so on. Figure 5.9a is the design pattern for split focusing OAM beams with the focal length of 40 μm and topological number of $n = \pm 1$. Figure 5.9b is the corresponding theoretical result. The actual structure is too large, so we only took a smaller part of the design structure in the calculation and obtained the splitting effect obviously. Figure 5.9c is the experimental image at the position of 40 μm, where the two focused OAM beams are separated by 15 μm.

It is to be sure that more splitting beams carrying different OAM topological numbers can be achieved by careful design and fabrication. Beam splitting is one of the necessary operations in information optics, especially in quantum optics. However, the traditional splitters are too large to be applied in the integrations. Our design method can realize beam splitting, different OAM beaming and profile modulating all in one compact structure, which are quite useful for OAM beams in integrations and applications on information and technology.

In this section, we designed spiral grating to generate OAM beams with different topological numbers with plasmonic structures and radiate the beams to the far field. We also introduced a radial phase modulation to the OAM beams into the generating process for the first time to modulate the beam profiles, realizing non-diffracting, focusing and off-axis OAM beams. Furthermore we realized a beam splitter design and generated different OAM beams with one design of a compact plasmonic structure, which will be of great importance in the future integration optics.

## 5.3 Polarization Reconfiguration and Polarization Router with Plasmonic Structures

As an important characteristic of light, polarization plays an important role in a wide range of applications, such as imaging, display, microscopy, and especially in today's information processing. Compared with the traditional optical devices, plasmonic devices provide a more compact and effective approach to modulate the optical polarization due to their high confinement of optical field. For instance, the plasmonic polarizers [33–37], polarization rotators and converters [38–42]. Recently, SPP-induced spin Hall Effect of light, which is related with the polarization and phase [43–46], has become a new research hotspot. Actually, the vector plasmonic nanostructures play an unique role in the conversion process between SPP and radiation field, where the polarization can be efficiently engineered during the conversion process [13, 47–50].

A couple of orthogonal polarization states are usually chosen as the basis vectors when apply the polarization of light to the information processing. For example, a pair of orthogonal linearly polarized lights, or circularly polarized lights with different spins. It means the corresponding polarization encoding is only in a two dimensional encoding system. The typical plasmonic polarizers are also limited to it. Increasing the dimensions of the polarization encoding processes will certainly improve the information capacity and processing ability. To keep pace with the ever increasing requirement of information processing, a full polarization generator is what people are in pursuit of.

In a common sense, this limitation would be overcome by a polarization generator to generate all polarization states simultaneously. As we all know, when two orthogonal polarized lights propagate along two mutually-perpendicular directions, a variety of polarization states can be formed in the intersection area. However, in free space two orthogonal lights do not interact with each other, so the polarization states from overlapping cannot be extracted. While in waveguide system, the orthogonal polarization states are usually accompany with other components, which will influence the purity of the polarizations, which can even change the distribution of the polarizations and reduce the extraction efficiency. In this regards, SPPs are quite different from the common waveguide modes. As reported by Zhang's group, only the longitudinal field (the component parallel to the surface) of SPPs will leak out to be detected, while the transverse field (the component perpendicular to the surface) will not in LRM system [10]. In fact, the situation is the same when SPPs are scattered by structures, in which only the longitudinal part of SPPs is scattered to far-field and the transverse part is still trapped on the surface, which provide us a clean system for polarization reconfiguration and effective extraction.

### 5.3.1 The Polarization Reconfiguration and Extraction on Metal Surface

The process of polarization reconfiguration is illustrated in Fig. 5.10 [51]. Two orthogonal propagating SPPs are launched by a polarized light incident onto an L-shaped slit on the metal surface with an initial phase determined by the polarization of the incident light ($\Delta\varphi_0 = \varphi_x - \varphi_y$). In the different positions of (x,y) on the metal surface, the two sets of SPP beams have different propagating lengths, giving rise to a phase difference of $\Delta\varphi = \Delta\varphi_0 + k_{SPP}(x - y)$ between them. Their transverse parts, which have the same polarization perpendicular to the metal surface, will interfere to form periodic fringes. While the longitudinal parts, which are parallel to the metal surface, are always orthogonal to each other. Due to the different phase differences at different positions, the two orthogonal longitudinal fields will lead to a series of polarization states on the metal surface. The distribution of the polarization states are illustrated in the inset in Fig. 5.10 with right hand circular polarized light as the incident light. The polarization states are the same with the incident light at the positions with equal propagation lengths or having a difference of multiple wavelengths (along diagonal) for the two components. The polarization states can be similarly obtained at other positions. Less of the transverse part of the SPPs is scattered to the space by structures on the metal surface, the majority part of the scattering field is their longitudinal part, giving rise to a purity scattering field with variety of reconfigured polarization states.

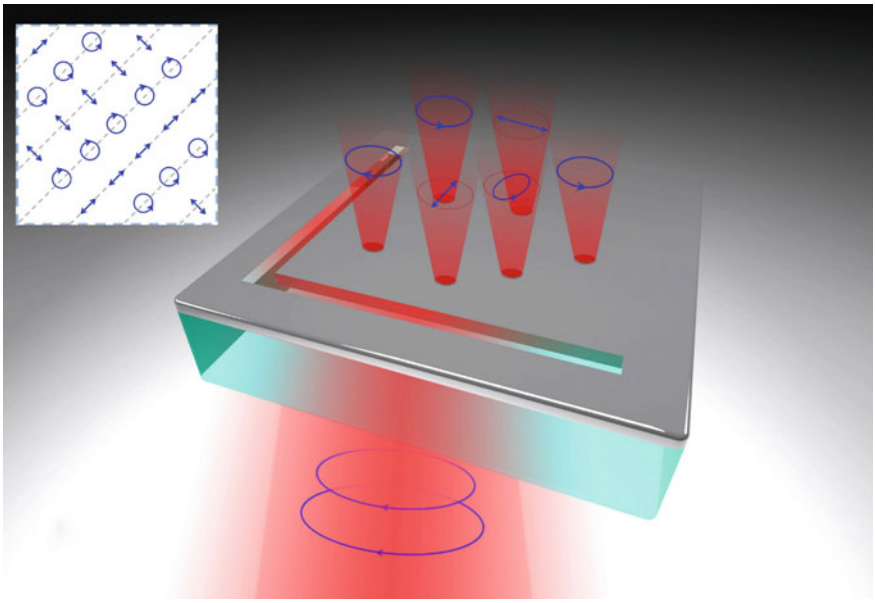

**Fig. 5.10** The schematic diagram of the reconfiguration of polarization states. The inset is the polarization states of in-plane SPP field distribution with a RCP light incident. Figure adapted with permission from Ref. [51], Macmillan Publishers Ltd.

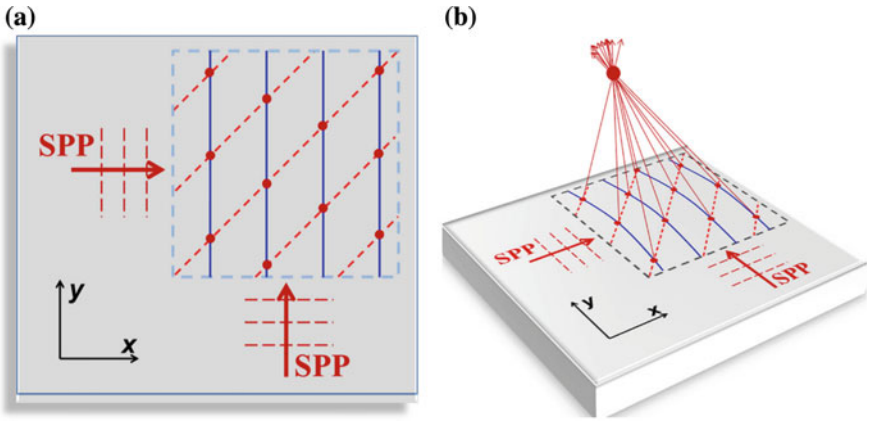


**Fig. 5.11** Design strategy for generating beams of plane wave (**a**) and focusing (**b**) with the same polarization states. Figure adapted with permission from Ref. [51], Macmillan Publishers Ltd.

Certain polarization states can be extracted from the metal surface by plasmonic structures to form special optical field with the polarizations. A certain polarization can be selected by polarization encoding devices so that to get the corresponding field profile. The phase design is another critical factor to achieve a certain optical field distribution. By considering the extraction of the polarization states and the phase requirement comprehensively, we propose a design strategy as schematically shown in Fig. 5.11. They are designs for generating plane wave and focusing with mono polarization states, respectively. The red dashed lines are a group of parallel lines with the same polarization states and intercept of $\delta = n\lambda_{SPP} + \delta_0$, where $n$ is an arbitrary integer, $\lambda_{SPP}$ is the SPP wavelength and $\delta_0$ is the initial intercept. The blue solid lines are the structures designed with previous mentioned phase modulation method to convert the SPPs propagating along x direction to a specific beam (for example, the periodic grating as shown in Fig. 5.11a is used to generate plane wave, while the curves in Fig. 5.11b are used to generate a focusing beam). The intersections of two sets of lines are just the positions of the designed structures. These intersections will have the same phase modulation on the other branch of SPP in y direction since they have the given phase difference $\Delta\varphi$ with SPP in x direction, whose contribution has been included in the reconfigured polarizations. The lights scattered by the nanostructures in these positions will have the same polarization states and simultaneously form the required beams.

### 5.3.2 *Experimental Realization of Reconfiguration and Extraction of the Polarization States*

Firstly, we experimentally tested the design scheme of reconfiguration and extraction of the polarization states. Figure 5.12a illustrates the optical

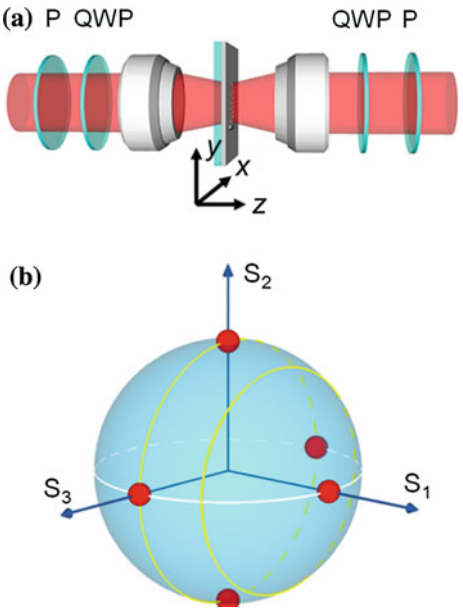


**Fig. 5.12** **a** Optical set up in the experiment. **b** Poincare sphere, where the bigger and smaller *yellow circles* represent the cases of $|\boldsymbol{E}_x|^2$: $|\boldsymbol{E}_y|^2 = 1:1$ and $|\boldsymbol{E}_x|^2$: $|\boldsymbol{E}_y|^2 = 1:3$, respectively. Figure adapted with permission from Ref. [51], Macmillan Publishers Ltd.

measurement system. A 633 nm He–Ne laser modulated by a polarizer and a quarter-wave plate is focused by an objective lens (4×) and incidents onto the orthogonal slits from the backside of the sample to generate SPPs. On the other side, the scattered light is collected by another objective lens (100×) and analyzed by the polarization analyzing system composed of a quarter-wave plate and a polarizer and images with a CCD camera.

Below we will firstly deduce the excitation and detection status of the optical set up. Here, $\theta_1$ and $\theta_2$ are the angles between the axis of the polarizers and the x-axis (horizontal). $\alpha$ and $\beta$ are the angles between the fast axis of the two quarter-wave plates and the x-axis, respectively. We set one of the coupling slits in the sample along the x-axis. The non-polarized incident He–Ne laser is linearly polarized by the polarizer with the field of:

$$A_0 = \begin{pmatrix} E_{H0} \\ E_{V0} \end{pmatrix} = \begin{pmatrix} \cos(\theta_1) \\ \sin(\theta_1) \end{pmatrix} \mathrm{E}_0 \tag{5.4}$$

where $E_{H0}$ and $E_{V0}$ are the horizontal and vertical components, respectively. This polarized light is then modulated to $\boldsymbol{A}_1 = \boldsymbol{G}_1 \cdot \boldsymbol{A}_0$ by a quarter-wave plate, with the transformation matrix written as:

$$\boldsymbol{G}_1 = \begin{pmatrix} \cos^2\alpha + i\sin^2\alpha & (1-i)\sin\alpha\cos\alpha \\ (1-i)\sin\alpha\cos\alpha & \sin^2\alpha + i\cos^2\alpha \end{pmatrix} \tag{5.5}$$

In this way, we can get an incident light with certain polarization state. Its horizontal and vertical components will be coupled by the two slits into SPPs propagating along x and y directions, respectively. With respect to the slits, the SPPs at the position of (x, y) have propagation phase of $k_{SPP}x$ and $k_{SPP}y$, respectively. Thus, the SPP field at this point is $A_2 = G_2 \cdot A_1$, with the transformation matrix written as:

$$\boldsymbol{G}_2 = \begin{pmatrix} e^{ik_{SPP}x} & 0 \\ 0 & e^{ik_{SPP}y} \end{pmatrix} = e^{i(k_{SPP}x + k_{SPP}y)/2} \begin{pmatrix} e^{i\Delta\varphi_s/2} & 0 \\ 0 & e^{-i\Delta\varphi_s/2} \end{pmatrix} \tag{5.6}$$

Here, $k_{SPP}$ is the SPP wave vector and $\Delta\varphi_s = k_{SPP}(x - y)$ is the phase difference of the two orthogonal propagating SPPs. Due to this phase difference, various of new polarization states are formed near the metal surface, which can be scattered out by the nanostructures on the metal surface with the polarization states unchanged. The scattered light is then modulated by another quarter-wave plate to $\boldsymbol{A}_3 = \boldsymbol{G}_3 \cdot \boldsymbol{A}_2$, with the transformation matrix written as:

$$\boldsymbol{G}_3 = \begin{pmatrix} \cos^2\beta + i\sin^2\beta & (1-i)\sin\beta\cos\beta \\ (1-i)\sin\beta\cos\beta & \sin^2\beta + i\cos^2\beta \end{pmatrix} \tag{5.7}$$

And finally the light will be selected by the second polarizer with the transformation matrix as:

$$\boldsymbol{G}_4 = \begin{pmatrix} \cos\theta_2 & 0 \\ 0 & \sin\theta_2 \end{pmatrix} \tag{5.8}$$

Before the final selection, the incident light is modulated by the optical set up into:

$$A_3 = G_3 \cdot G_2 \cdot G_1 \cdot A_0 = e^{i(kx+ky)/2} E_0 \begin{pmatrix} A_{3H} \\ A_{3V} \end{pmatrix} \tag{5.9}$$

where

$$\begin{aligned} \boldsymbol{A}_{3H} = a + ib = {} & \cos(\Delta\varphi_s/2)\cos(\alpha-\beta)\cos(\theta_1-\alpha-\beta) \\ & + \sin(\Delta\varphi_s/2)\sin(\alpha+\beta)\sin(\theta_1-\alpha-\beta) \\ & + i(\sin(\Delta\varphi_s/2)\cos(\alpha+\beta)\cos(\theta_1-\alpha+\beta) - \cos(\Delta\varphi_s/2)\sin(\alpha-\beta)\sin(\theta_1-\alpha+\beta)) \end{aligned}$$

$$\begin{aligned} \boldsymbol{A}_{3V} = c + id = {} & -\cos(\Delta\varphi_s/2)\cos(\alpha-\beta)\sin(\theta_1-\alpha-\beta) \\ & + \sin(\Delta\varphi_s/2)\sin(\alpha+\beta)\cos(\theta_1-\alpha-\beta) \\ & + i(\sin(\Delta\varphi_s/2)\cos(\alpha+\beta)\sin(\theta_1-\alpha+\beta) + \cos(\Delta\varphi_s/2)\sin(\alpha-\beta)\cos(\theta_1-\alpha+\beta)) \end{aligned}$$

To get a pure polarization state through the second polarizer, the incident light must be linearly polarized. Thus we have

$$b/a = \pm d/c \tag{5.10}$$

or

$$a = c = 0 \quad \text{or} \quad b = d = 0 \tag{5.11}$$

Generally there is no simple solution for Eq. 5.10. However, it can be simplified at the case of α or β equals ±π/4. When α = π/4, $\alpha - \beta$ equals $\pi/2 - (\alpha + \beta)$, we have

$$\boldsymbol{A}_{3H} = \sin(\alpha+\beta)\cos(\Delta\varphi_s/2+\alpha+\beta-\theta_1) + i\cos(\alpha+\beta)\sin(\Delta\varphi_s/2+\alpha-\beta-\theta_1) \tag{5.12}$$

$$\boldsymbol{A}_{3V} = \sin(\alpha+\beta)\sin(\Delta\varphi_s/2+\alpha+\beta-\theta_1) + i\cos(\alpha+\beta)\sin(\Delta\varphi_s/2+\alpha-\beta-\theta_1) \tag{5.13}$$

Then the solution for Eq. 5.10 is $\beta = \pm\pi/4$, or $\Delta\varphi_s/2 - \theta_1 + \alpha = n\pi/2 + \pi/4$, which will be discussed as below, respectively.

(a) If $\beta = \pi/4$, the total electric field after passing through the second polarizer is:

$$\boldsymbol{A}_4 = \boldsymbol{G}_4 \cdot \boldsymbol{A}_3 = \boldsymbol{A}_{3H}\cos(\theta_2) + \boldsymbol{A}_{3V}\sin(\theta_2) = \sin(\theta_1+\theta_2-\Delta\varphi_s/2) \tag{5.14}$$

Thus the intensity of the scattering light from the position of (x, y) on the sample after passing through the whole optical path is proportional to $\sin^2(\theta_1+\theta_2-\Delta\varphi_s/2)$.

(b) If $\beta = -\pi/4$, the total change of the electric field is:

$$\begin{aligned}\boldsymbol{A}_4 &= i(\sin(\Delta\varphi_s/2+\alpha-\beta-\theta_1)\cos(\theta_2) + \cos(\Delta\varphi_s/2+\alpha-\beta-\theta_1)\sin(\theta_2)) \\ &= i\cos(\theta_1-\theta_2-\Delta\varphi_s/2)\end{aligned} \tag{5.15}$$

The intensity of the corresponding scattering light is proportional to $\cos^2(\theta_1-\theta_2-\Delta\varphi_s/2)$.

(c) If $\Delta\varphi_s/2 - \theta_1 + \alpha = n\pi/2 + \pi/4$, in which if $n = 2m$($m$ is integer), we have:

$$\boldsymbol{A}_4 = \pm\cos(\theta_2-\pi/4-\beta)(\sin(\alpha+\beta) + i\cos(\alpha+\beta)) \tag{5.16}$$

If $n = 2m + 1$, we have:

$$\boldsymbol{A}_4 = \pm \sin(\theta_2 - \pi/4 - \beta)(\sin(\alpha + \beta) + i\cos(\alpha + \beta)) \tag{5.17}$$

So the corresponding intensity is proportional to $\cos^2(\theta_2 - \pi/4 - \beta)$ or $\sin^2(\theta_2 - \pi/4 - \beta)$. However this result has no relation with $\Delta\varphi_s$, thus it is useless for the polarization reconfiguration. The transformation process in other situations can be derived similarly and the results are shown in Table 5.1.

The above table provides us the set up for polarization detection and the corresponding detection results. It is easy to figure out that once a certain detection set up is determined, the intensity of the scattered polarized light from the position (x, y) can be manipulated through the angle changing of the incident and exit polarizers.

In polarization optics, the Poincaré sphere is usually used to describe the polarization states. Any polarization state can be represented as a point on the surface of the sphere. Here we can also use the Poincaré sphere to discuss various kinds of polarization states in our study. The three separate Stokes components of the Poincaré sphere are defined as below (as shown in Fig. 5.12b):

$$\begin{aligned} S_1 &= \left|\boldsymbol{E}_y\right|^2 - \left|\boldsymbol{E}_x\right|^2, \\ S_2 &= 2\left|\boldsymbol{E}_x\right|\left|\boldsymbol{E}_y\right|\sin\delta, \\ S_3 &= 2\left|\boldsymbol{E}_x\right|\left|\boldsymbol{E}_y\right|\cos\delta. \end{aligned}$$

We can get all the corresponding polarization states of any points on the Poincaré sphere by our polarization reconfiguration method. Any polarization state is determined by the relative amplitude and phase of its two orthogonal components. We can tune the relative amplitude of the two sets of SPPs by the polarization state of the incident light and tune their relative phase by the position of the scattering structures. In this way, we can achieve various kinds of polarization states. When the amplitudes of the components in x and y directions of the incident light are equal $\left(\left|\boldsymbol{E}_x\right|^2 : \left|\boldsymbol{E}_y\right|^2 = 1 : 1\right)$, all the polarization states on the yellow great circle of the Poincaré sphere shown in Fig. 5.12b can be achieved by tuning the

**Table 5.1** The intensity under different polarization conditions

| Incidence | Analyzing | Intensity |
|---|---|---|
| $\alpha = \pi/4$ | $\beta = \pi/4$ | $\sin^2(\theta_1 + \theta_2 - \Delta\varphi_s/2)$ |
| $\alpha = \pi/4$ | $\beta = -\pi/4$ | $\cos^2(\theta_1 - \theta_2 - \Delta\varphi_s/2)$ |
| $\alpha = -\pi/4$ | $\beta = \pi/4$ | $\cos^2(\theta_1 - \theta_2 + \Delta\varphi_s/2)$ |
| $\alpha = -\pi/4$ | $\beta = -\pi/4$ | $\sin^2(\theta_1 + \theta_2 + \Delta\varphi_s/2)$ |
| $\theta_1 - \alpha = \pi/4$ | $\beta = \pi/4$ | $\cos^2(\theta_2 - \Delta\varphi_s/2)$ |
| $\theta_1 - \alpha = -\pi/4$ | $\beta = \pi/4$ | $\sin^2(\theta_2 - \Delta\varphi_s/2)$ |
| $\theta_1 - \alpha = \pi/4$ | $\beta = -\pi/4$ | $\sin^2(\theta_2 + \Delta\varphi_s/2)$ |
| $\theta_1 - \alpha = -\pi/4$ | $\beta = -\pi/4$ | $\cos^2(\theta_2 + \Delta\varphi_s/2)$ |

position (x, y) of the scattering structures. Similarly, all polarization states in the small circle in Fig. 5.12b with $|\boldsymbol{E}_x|^2$: $|\boldsymbol{E}_y|^2 = 1:3$ can be generated when the polarization of the incident light is 60° to the horizontal direction. Likewise, the polar point on S1 axis of the Poincaré sphere can be realized with a vertical polarized incidence.

Here we chose $\alpha = -\pi/4$, $\beta = \pi/4$ as an example to verify our proposal. From Table 5.1 we can see that the exit intensity of the polarization state at (x, y) is proportional to $\cos^2(\theta_1 - \theta_2 - \Delta\varphi_s/2)$. According to the design method proposed previously, we use a periodic array to produce a plane wave from the x-propagating SPPs. The sample was fabricated by FIB on a 200 nm-thick silver film. The L-shaped slits are 100 nm in width and penetrate through the silver film. The slit width is much smaller than the incident wavelength so that to couple more light into SPPs. All the nanoholes are 150 nm in diameter and 80 nm in depth. The similar experimental parameters are used in the following part of this chapter. Figure 5.13a is the SEM image of the sample, where the nanoholes along x direction have a period of 500 nm and an initial intercept is $\delta_0 = b - a = \lambda_{SPP}/2$. Figure 5.13b and

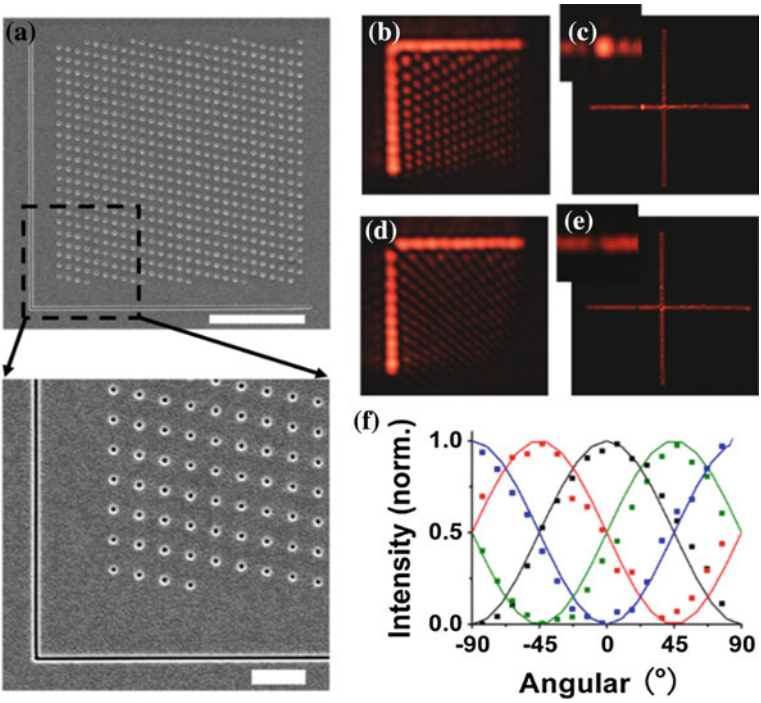


**Fig. 5.13** Experimental demonstration of polarization reconfiguration. **a** The SEM image of the sample. **b**, **d** The results in the real space and **c**, **e** the images in the corresponding reciprocal space with the polarization states selected or not, respectively. **f** The integral intensity of scattering spot in reciprocal space with different conditions. Figure adapted with permission from Ref. [51], Macmillan Publishers Ltd.

d are the measured results in real space when the polarization analyzer selected the polarization of the structure or the orthogonal one, respectively. When the polarization state is selected, an array of bright spots are clearly shown in Fig. 5.13b, which are formed by the interference of the scattered lights from the nanoholes. While there are only line-shaped interference stripes along the diagonal when the polarization state is not selected. It is the interference result of the direct transmitted light from the coupled slits, which carries nothing of the related information from the structure. Meanwhile, we record the corresponding images in the reciprocal space as shown in Fig. 5.13c, e, where a bright spot is shown in Fig. 5.13c when the polarization state is selected and no spot appears otherwise in Fig. 5.13e. Furthermore, we measured the integral intensities of the spot at different polarization analyzing conditions as shown in Fig. 5.13f. The dot plots are the measured results at different angles of the polarizer when the initial intercepts were $\delta_0 = \lambda_{SPP}/2$, $\lambda_{SPP}/4$, 0, $-\lambda_{SPP}/4$, respectively (corresponding to the 4 red spots on the big circle in Fig. 5.12b), shown together with the corresponding theoretical results displayed in solid curves. The experimental results are well consistent with the theoretical results, indicating the validation of the polarization configuration in the optical system in Table 5.1. It verified the feasible of our polarization reconfiguration and the design method as well. As has been interpreted as polarization generator, any polarization state can be generated with respect to the location of the nanohole array in demand by continuously shift the scatterer array. Using this model and design method, we can achieve series of new manipulations and modulations of the spatial optical fields.

There are only two orthogonal eigenstates in the ordinary polarization modulations, so that the modulations are quite limited. However, as we can see from Table 5.1, our model is much different, which is not limited to the only two eigenstates. As long as two polarization states have a phase difference of $\pi$, they can be regarded as a couple of working states, thus realizing high contrast polarization modulation. Meanwhile, the corresponding modulation methods and combinations are much richer, providing us more room and possibilities to do optical field modulations.

### 5.3.3 *Active Modulation by Polarization Reconfiguration*

Here we performed the generations and modulations of several spatial beams based on this model. Firstly we realized polarization defined focusing beams, which is the most common and very useful operation in optics. We designed structures with the approach illustrated in Fig. 5.11b, in which the left two quadrants (II and III) were designed with the initial intercept of $\delta 0 = \lambda SPP/2$ targeting a focus at the position of (−7.5, 0, 40 μm) on the left side, while the right quadrants (I and IV) were designed for the right focus (7.5, 0, 40 μm) with $\delta 0 = 0$. To achieve a symmetric result, we used cross-shaped slits to generate SPPs and the scattering structures were uniformly distributed over the four quadrants. Figure 5.14a shows SEM image

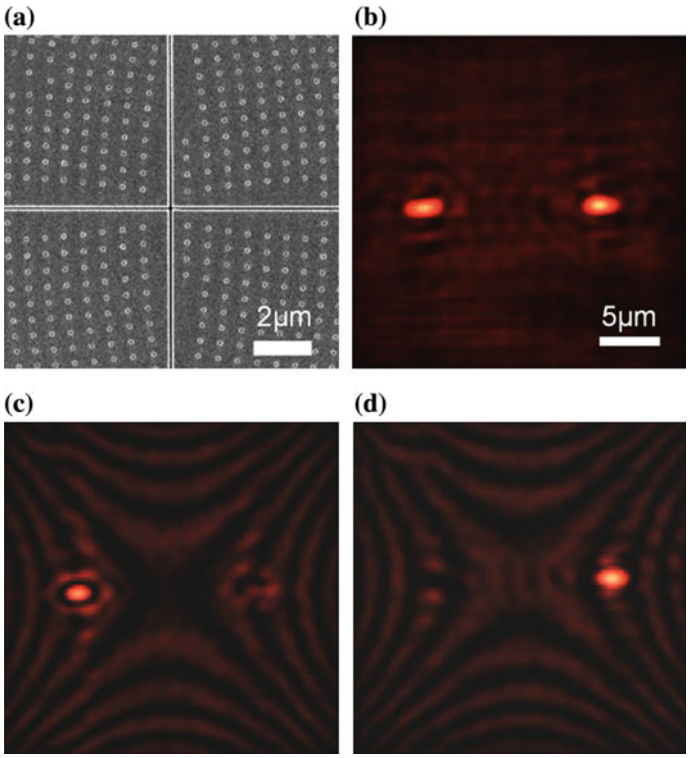


**Fig. 5.14** Polarization analysis on focusing beams. **a** SEM image at the center of the sample. **b** Focus image without polarization analysis. **c**, **d** Images when each of the polarization states is selected, respectively. Figure adapted with permission from Ref. [51], Macmillan Publishers Ltd.

of the center area of the sample fabricated by FIB. Figure 5.14b is the images recorded by CCD camera at the focal plane of 40 μm without polarization analyzing, where two bright focal spots are clearly observed. Figure 5.14c and d are the images when the polarization states of the left and right parts are selected by the analyzing, respectively. The focal spot corresponding to the selected polarization state is still quite bright, while the other spot totally darkens. When the opposite polarization state is selected, the situation would be reversed. The intercept of the hole array indeed determine the generated polarization states for a required diffraction beam. That means, $\delta 0 = 0$ corresponds to the initial state, $\delta 0 = \lambda SPP/2$ to the orthogonal one, and $\delta 0 = \lambda SPP/4$ (and $3\lambda SPP/4$) to the conversion from circular to linear polarizations. Therefore, taking good usage of the planar space, any kind of polarization state can be achieved, which gives rise to what we emphasized - polarization generator.

More importantly, this reconfigurable planar design with scatterer array is of capability for multiplexing, in principle, all kinds of polarization states in any required beam-forms can be achieved simultaneously. Here, to manifest this

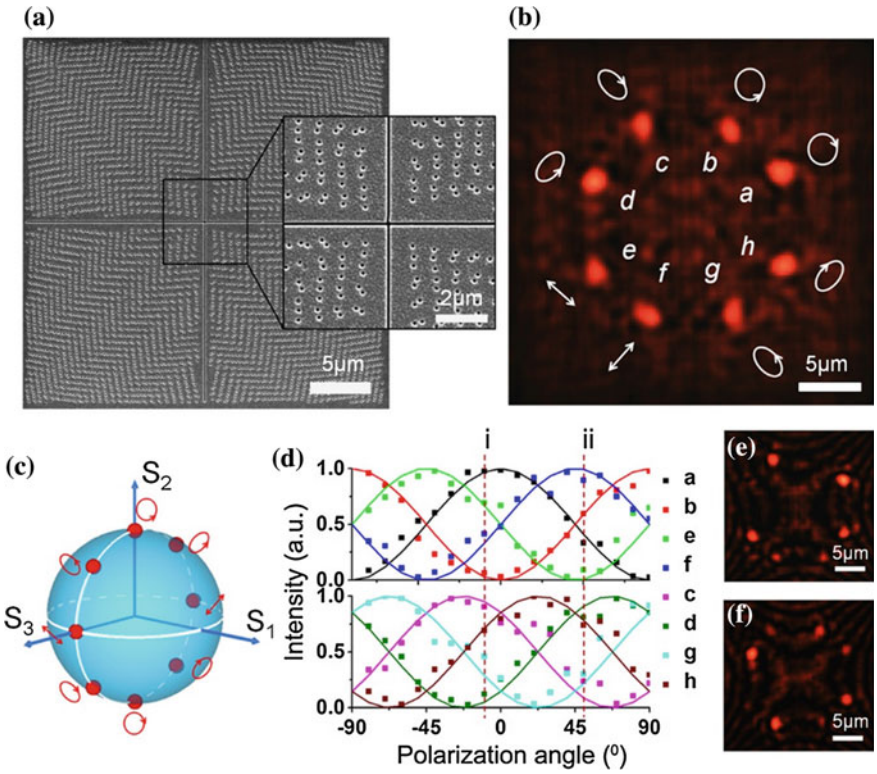


**Fig. 5.15** Simultaneous generation of eight-foci with different polarization states. **a** SEM image of the sample. **b** Focus image without polarization analysis, the white signs represent the polarization states of the corresponding foci. **c** The polarization states of the foci on the Poincaré sphere. **d** Integrated intensities of the foci at different polarization analysis conditions. **e**, **f** Two focus images corresponding to the *dashed lines* (i) and (ii) in panel (**d**). Figure adapted with permission from Ref. [51], Macmillan Publishers Ltd.

function we demonstrate an eight-focuses polarization generation that is fulfilled by composite nanohole arrays with the spatial multiplexing. The scattered light beams are designed to be focused to eight vertexes of a right octagon, with respect to eight different polarization states in the Poincaré sphere. The SEM image of the structure is shown in Fig. 5.15a, showing a composite nano-array. The scattering structures are composed of eight sets of nanohole arrays whose initial intercepts have an equal gap of $\lambda_{SPP}/8$. The scattered light beams are designed to be focused to the eight vertexes of a right octagon with the side length of about 8.3 μm. The focuses are separated into four couples with the corresponding structures laid in the four quadrants in sequence. In each quadrant, two sets of nanoarrays with the initial intercept difference of λSPP/2 are designed and fabricated according to two orthogonal polarization states, revealing a mixed feature of the two structures (see the zoom-in image in Fig. 5.15a).

In the experiments, we use RCP as the incident light as in previous experiment. In this situation, the amplitudes of the SPPs in the transverse and vertical directions are equal $\left(|\boldsymbol{E}_x|^2 : |\boldsymbol{E}_y|^2 = 1:1\right)$, with which we can obtain the eight polarization states corresponding to the eight red dots on the great circle of the Poincaré sphere shown in Fig. 5.15c. Figure 5.15b shows the images recorded without polarization analyzing, where the eight focuses are clearly shown in the focal plane (z = 40 μm) with similar intensities with the corresponding designed polarization states are sketched aside. To identify these polarization states, the integrated intensities of the foci with respect to different analyzing conditions are plotted in Fig. 5.15d, where different polarizer angles corresponds to different polarization states. The intensities shows good agreement with the theoretical predictions of $\cos^2(\theta 1 - \theta 2 + \Delta\varphi)$, where θ1 is fixed for the RCP incidence and $\Delta\varphi$ = kSPPδ0 corresponding for the eight different states. Figure 5.15e and f are the typical focusing results under polarization analyzing, corresponding to the dashed lines (i) and (ii) in Fig. 5.15d, respectively. The intensities of the focuses are clearly distinct, especially those orthogonal pairs, indicating the realization of eight polarization states.

Our approach has demonstrated the powerful ability in generating multiple routed beams with various polarizations. Compared with previous means in polarization control (polarization rotators, convertor, etc.), our strategy breaks function limitation by introducing an intermediate process between the light input and output—the orthogonal SPP interference as the reconfigurable polarization generator. In addition, this strategy is quite general and adaptable. The process of polarization reconfiguration and extraction does not conflict with the popular beam modulation methods such as coupling and resonance [27, 52], instead it can combine with them to provide us a new dimension of freedom in modulation.

In 2013, Capasso's group proposed a particular design of aperture array to launch unidirectional SPPs. Through this structure, different kinds of circular polarized incidences can be coupled to SPPs with different propagating directions. Therefore, it is quite appropriate to combine with our four-quadrant device to replace the slit couplers, as schematically shown in Fig. 5.16a, where SPPs will be launched propagating to the quadrants II and IV with an RCP incidence, while to the other two quadrants for a LCP case. These two kinds of SPPs will then be extracted of different polarization states respectively to form new beams through our designed structures, thereby realizing 2 × 2 polarization division multiplexing. Figure 5.16b shows the center of the sample fabricated by FIB, where the structures in quadrants I and III have initial intercepts of $\delta_0 = 0$ and $\delta_0 = \lambda_{SPP}/2$, respectively, to realize corresponding focusing with foci located at (3, 3, 40) and (−3, −3, 40). The structures in quadrants II and IV have the same kinds of initial intercepts to generate focusing at the positions of (−3, 3, 40) and (3, −3, 40). Figure 5.16c is the image of the sample surface under RCP incidence without polarization analysis, where quadrants I and III are not illuminated but quadrants II and IV are illuminated, indicating the unidirectional propagation of the SPPs. Figure 5.16d–g are the images under different circular polarization incidences and different polarization analysis, where four totally independent foci are clearly shown. Thus the combination of our model with

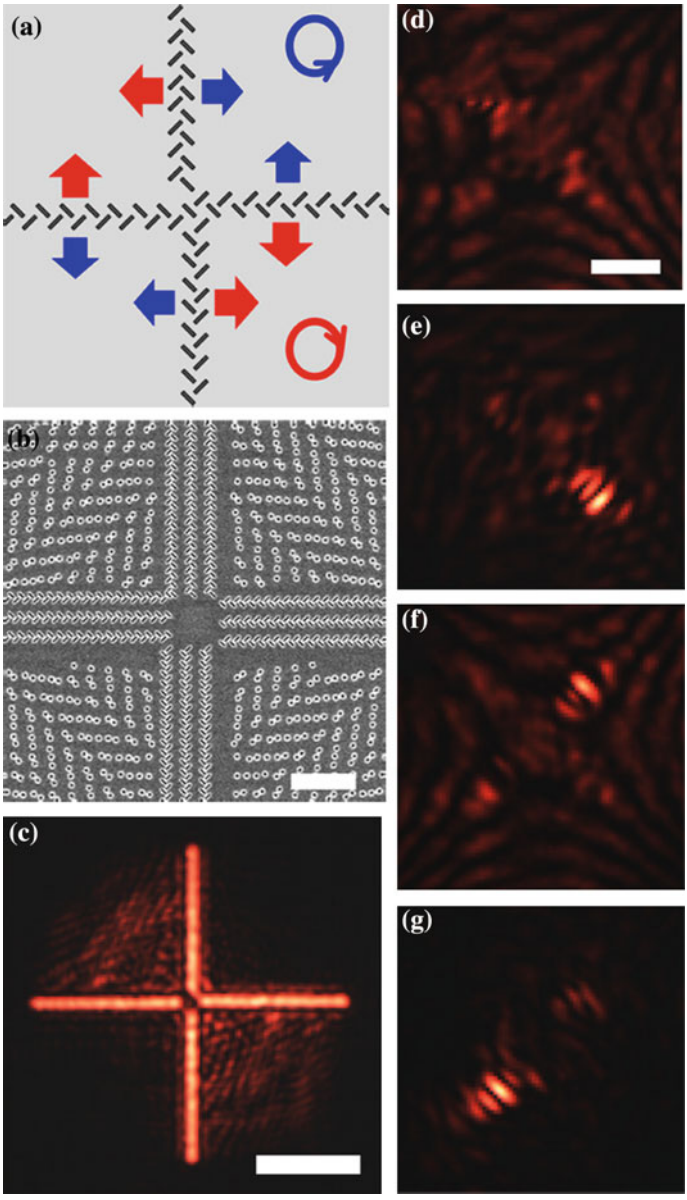


**Fig. 5.16** The realization of $2 \times 2$ polarization division multiplexer. Figure adapted with permission from Ref. [51], Macmillan Publishers Ltd.

the unidirectional coupling principle was well demonstrated. With that a $2 \times 2$ polarization division multiplexer was realized, indicating a new dimension of freedom in polarization modulation.

It is the same with the phase modulation method proposed in the previous chapter that this polarization reconfiguration and beaming method can not only be applied to the realization and modulation of simple light beams as plane wave and focusing, but can also be applied to other beams. It can even be combined with the holography design. We only need to find the intersections of these phase design structures with the lines which determine the polarization states. Here we demonstrated non-diffracting Airy beam with determined polarizations by this method. We designed phase structures to generate far-field Airy beam from the x-propagating SPPs. Figure 5.17c and d show the recorded images corresponding to the positions

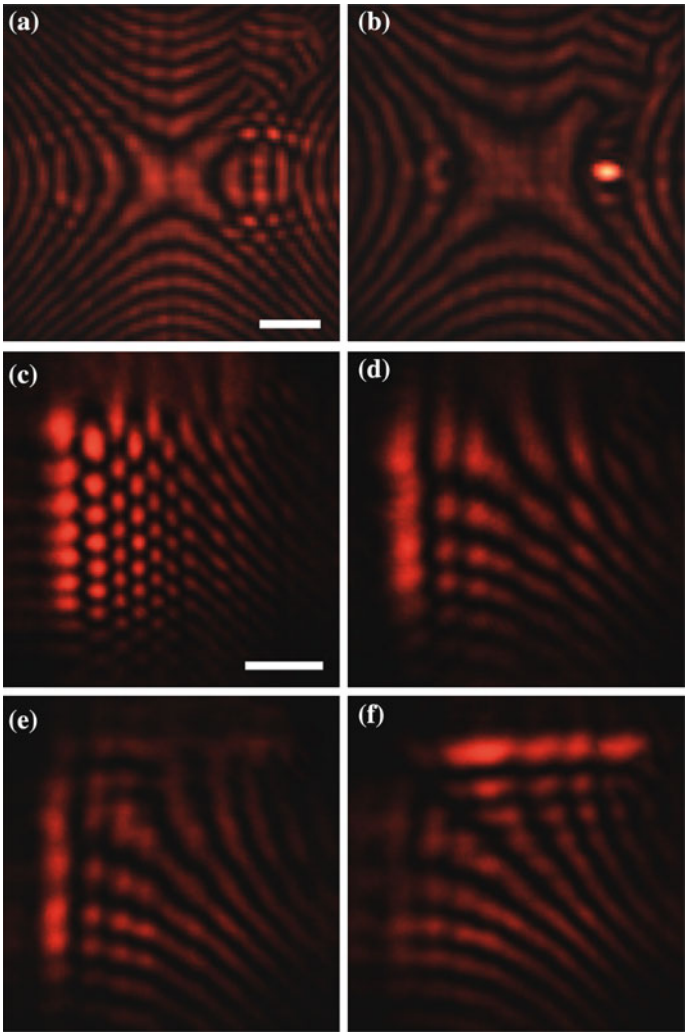


**Fig. 5.17** Polarization modulation of Airy beams. **a**, **b** Images of focusing beam at z = 20 and 40 μm. **c**, **d** Images of Airy beam at the same positions as the corresponding focusing beam. **e**, **f** The optical fields of Airy beam at z = 40 μm under two orthogonal polarization analysis

of z = 20 and 40 μm away from the metal surface, respectively. As we can see, during propagating, the width of the main lobe is almost the same and it moves to the left gradually. For comparison, we showed the focusing images with foci of $f$ = 40 μm at the same positions in Fig. 5.17a, b, where the variation of the optical field was apparently showed, indicating the non-diffracting property of the generated Airy beams. The polarization of the generated Airy beam can also be selected and modulated as the case of focusing beam. We designed a composite structure to generate Airy beams in horizontal and vertical directions with two orthogonal polarizations with initial intercepts of $\delta_0 = \lambda_{SPP}/4$ and $\delta_0 = -\lambda_{SPP}/4$, respectively. Figure 5.17e and f are the images at the position of z = 40 μm corresponding to the two states, respectively. When the intensity of the Airy beam at one state reaches the maximum, the other one is almost zero and vice versa, which indicates the general applicability of our polarization reconfiguration and beaming method in spatial beam modulations, including complex optical field such as Airy beams.

So far, we have proposed and demonstrated a plasmonic polarization generator that can reconfigure an incident polarization into various polarization states with desired beam forms with the longitudinal component of SPPs. The critical process is established by the interference of orthogonal in-plane field of two SPPs launched by two crossed slits. Including two orthogonal states, eight polarization states were generated and routed to eight focuses. This method is quite general and it is adaptable to other polarization coding or multiplexing strategies. Our strategy breaks the limitation of conventional means in simplex polarization control, and offers versatile and flexible opportunities in tailoring the polarization and phase of light all at once. Besides the revealed polarization generator, this approach is expected to promote the capability of people in full control of the light and even open a new avenue in designing new kinds integrated functional photonic devices.

## 5.4 Conclusion

In this chapter, we have extended the nonlinear phase modulation method to the modulation to the light in 3D free space, which shows the generality of the phase modulation method. Based on the phase modulation with plasmonic structures, a series of new phenomenon and applications are studied.

An OAM beam in free space is realized with compact plasmonic structure. Meanwhile, a phase modulation in the radial direction is proposed to integrated tune the properties of the realized OAM beam, such as non-diffraction, focusing or off-axial ejection, and so on. In addition, an integrated beam splitter is achieved as well, which can split a beam into multiple OAM beams with different topological numbers. The compact integrated OAM beam generation and modulation with plasmonic structures will have great impact to the research and applications of optical information.

A plasmonic polarization generator that can reconfigure an input polarization to all kinds of states is proposed based on the interference of the in-plane

(longitudinal) field of the SPPs that gives rise to versatile near-field polarization states on a metal surface, which was seldom considered in previous studies. With a well designed nanohole array, the in-plane field of SPPs with proper polarization states and phases can be selectively scattered out to form desired light beams, such as the plan wave, focusing or Airy beam, and so on. In addition, this method is capable of multiplexing, with which a manifestation of eight focusing beams with well routed polarizations are experimentally demonstrated. Meanwhile, the reconfigurable method provides a new adaptable freedom for the polarization control, which can coexistent with other polarization control mechanisms. Our design offers a new route to achieve the full control of optical polarizations and possibly boost the development of photonic information processing.

## References

1. Coullet P, Gil L, Rocca F (1989) Optical vortices. Opt Commun 73:403–408
2. Allen L, Beijersbergen MW, Spreeuw RJC, Woerdman JP (1992) Orbital angular-momentum of light and the transformation of Laguerre-Gaussian laser modes. Phys Rev A 45:8185–8189
3. Barnett SM, Allen L (1994) Orbital angular-momentum and nonparaxial light-beams. Opt Commun 110:670–678
4. He H, Friese M, Heckenberg N, Rubinsztein-Dunlop H (1995) Direct observation of transfer of angular momentum to absorptive particles from a laser beam with a phase singularity. Phys Rev Lett 75:826
5. Grier DG (2003) A revolution in optical manipulation. Nature 424:810–816
6. Beržanskis A, Matijošius A, Piskarskas A, Smilgevičius V, Stabinis A (1997) Conversion of topological charge of optical vortices in a parametric frequency converter. Opt Commun 140:273–276
7. Gibson G, Courtial J, Padgett M, Vasnetsov M, Pas'ko V, Barnett S, Franke-Arnold S (2004) Free-space information transfer using light beams carrying orbital angular momentum. Opt Express 12:5448–5456
8. Bouchal Z, Celechovský R (2004) Mixed vortex states of light as information carriers. New J Phys 6:131
9. Leach J, Padgett MJ, Barnett SM, Franke-Arnold S, Courtial J (2002) Measuring the orbital angular momentum of a single photon. Phys Rev Lett 88:257901–257901
10. Wang J, Zhao C, Zhang J (2010) Does the leakage radiation profile mirror the intensity profile of surface plasmon polaritons? Opt Lett 35:1944–1946
11. Lezec HJ, Degiron A, Devaux E, Linke R, Martin-Moreno L, Garcia-Vidal F, Ebbesen T (2002) Beaming light from a subwavelength aperture. Science 297:820–822
12. Kim S, Lim Y, Kim H, Park J, Lee B (2008) Optical beam focusing by a single subwavelength metal slit surrounded by chirped dielectric surface gratings. Appl Phys Lett 92:013103
13. Genevet P, Lin J, Kats MA, Capasso F (2012) Holographic detection of the orbital angular momentum of light with plasmonic photodiodes. Nature communications 3:1278
14. Chen Y-H, Huang L, Gan L, Li Z-Y (2012) Wavefront shaping of infrared light through a subwavelength hole. Light: Sci Appl 1:e26
15. Aouani H, Mahboub O, Bonod N, Devaux E, Popov E, Rigneault H, Ebbesen TW, Wenger J (2011) Bright unidirectional fluorescence emission of molecules in a nanoaperture with plasmonic corrugations. Nano Lett 11:637–644

16. Jun YC, Huang KCY, Brongersma ML (2011) Plasmonic beaming and active control over fluorescent emission. Nat Commun 2
17. Tang X, Li L, Li T, Wang Q, Zhang X, Zhu S, Zhu Y (2013) Converting surface plasmon to spatial Airy beam by graded grating on metal surface. Opt Lett 38:1733–1735
18. Yao AM, Padgett MJ (2011) Orbital angular momentum: origins, behavior and applications. Adv Opt Photonics 3:161–204
19. Siegman A (1986) Lasers. University Science, Mill Valley, 663pp (Chap. 13)
20. Čelechovský R, Bouchal Z (2007) Optical implementation of the vortex information channel. New J Phys 9:328
21. Wang J, Yang J-Y, Fazal IM, Ahmed N, Yan Y, Huang H, Ren Y, Yue Y, Dolinar S, Tur M (2012) Terabit free-space data transmission employing orbital angular momentum multiplexing. Nat Photonics 6:488–496
22. Bozinovic N, Yue Y, Ren Y, Tur M, Kristensen P, Huang H, Willner AE, Ramachandran S (2013) Terabit-scale orbital angular momentum mode division multiplexing in fibers. Science 340:1545–1548
23. Fickler R, Lapkiewicz R, Plick WN, Krenn M, Schaeff C, Ramelow S, Zeilinger A (2012) Quantum entanglement of high angular momenta. Science 338:640–643
24. Leach J, Jack B, Romero J, Jha AK, Yao AM, Franke-Arnold S, Ireland DG, Boyd RW, Barnett SM, Padgett MJ (2010) Quantum correlations in optical angle–orbital angular momentum variables. Science 329:662–665
25. Cai X, Wang J, Strain MJ, Johnson-Morris B, Zhu J, Sorel M, O'Brien JL, Thompson MG, Yu S (2012) Integrated compact optical vortex beam emitters. Science 338:363–366
26. Bloch NV, Shemer K, Shapira A, Shiloh R, Juwiler I, Arie A (2012) Twisting light by nonlinear photonic crystals. Phys Rev Lett 108:233902
27. Yu NF, Genevet P, Kats MA, Aieta F, Tetienne JP, Capasso F, Gaburro Z (2011) Light propagation with phase discontinuities: generalized laws of reflection and refraction. Science 334:333–337
28. Chen W, Abeysinghe DC, Nelson RL, Zhan Q (2010) Experimental confirmation of miniature spiral plasmonic lens as a circular polarization analyzer. Nano Lett 10:2075–2079
29. Rui G, Abeysinghe DC, Nelson RL, Zhan Q (2013) Demonstration of beam steering via dipole-coupled plasmonic spiral antenna. Sci Rep 3
30. Dolev I, Epstein I, Arie A (2012) Surface-plasmon holographic beam shaping. Phys Rev Lett 109:203903
31. Gorodetski Y, Drezet A, Genet C, Ebbesen TW (2013) Generating far-field orbital angular momenta from near-field optical chirality. arXiv:1302.0678
32. Chattrapiban N, Rogers EA, Cofield D, Hill WT III, Roy R (2003) Generation of nondiffracting Bessel beams by use of a spatial light modulator. Opt Lett 28:2183–2185
33. Koerkamp KK, Enoch S, Segerink F, Van Hulst N, Kuipers L (2004) Strong influence of hole shape on extraordinary transmission through periodic arrays of subwavelength holes. Phys Rev Lett 92:183901
34. Gordon R, Brolo A, McKinnon A, Rajora A, Leathem B, Kavanagh K (2004) Strong polarization in the optical transmission through elliptical nanohole arrays. Phys Rev Lett 92:037401
35. Yu N, Wang QJ, Pflügl C, Diehl L, Capasso F, Edamura T, Furuta S, Yamanishi M, Kan H (2009) Semiconductor lasers with integrated plasmonic polarizers. Appl Phys Lett 94:151101
36. Ellenbogen T, Seo K, Crozier KB (2012) Chromatic plasmonic polarizers for active visible color filtering and polarimetry. Nano Lett 12:1026–1031
37. Wang L, Li T, Guo R, Xia W, Xu X, Zhu S (2013) Active display and encoding by integrated plasmonic polarizer on light-emitting-diode. Scientific reports 3:2603
38. Zhang J, Zhu S, Chen S, Lo G-Q, Kwong D-L (2011) An ultracompact surface plasmon polariton-effect-based polarization rotator. Photonics Technol Lett IEEE 23:1606–1608
39. Li T, Wang S, Cao J, Liu H, Zhu S (2010) Cavity-involved plasmonic metamaterial for optical polarization conversion. Appl Phys Lett 97:261113

40. Xu J, Li T, Lu F, Wang S, Zhu S (2011) Manipulating optical polarization by stereo plasmonic structure. Opt Express 19:748–756
41. Zhao Y, Alù A (2011) Manipulating light polarization with ultrathin plasmonic metasurfaces. Phys Rev B 84:205428
42. Li T, Liu H, Wang S-M, Yin X-G, Wang F-M, Zhu S-N, Zhang X (2008) Manipulating optical rotation in extraordinary transmission by hybrid plasmonic excitations. Appl Phys Lett 93:021110
43. Shitrit N, Bretner I, Gorodetski Y, Kleiner V, Hasman E (2011) Optical spin Hall effects in plasmonic chains. Nano Lett 11:2038–2042
44. Shitrit N, Yulevich I, Maguid E, Ozeri D, Veksler D, Kleiner V, Hasman E (2013) Spin-optical metamaterial route to spin-controlled photonics. Science 340:724–726
45. Yin X, Ye Z, Rho J, Wang Y, Zhang X (2013) Photonic spin hall effect at metasurfaces. Science 339:1405–1407
46. Li G, Kang M, Chen S, Zhang S, Pun EY-B, Cheah KW, Li J (2013) Spin-enabled plasmonic metasurfaces for manipulating orbital angular momentum of light. Nano Lett 13:4148–4151
47. Gorodetski Y, Drezet A, Genet C, Ebbesen TW (2013) Generating far-field orbital angular momenta from near-field optical chirality. Phys Rev Lett 110:203906
48. Lin J, Mueller JB, Wang Q, Yuan G, Antoniou N, Yuan X-C, Capasso F (2013) Polarization-controlled tunable directional coupling of surface plasmon polaritons. Science 340:331–334
49. Rodríguez-Fortuño FJ, Marino G, Ginzburg P, O'Connor D, Martínez A, Wurtz GA, Zayats AV (2013) Near-field interference for the unidirectional excitation of electromagnetic guided modes. Science 340:328–330
50. Miroshnichenko AE, Kivshar YS (2013) Polarization traffic control for surface plasmons. Science 340:283–284
51. Li L, Li T, Tang XM, Wang SM, Wang QJ, Zhu SN (2015) Plasmonic polarization generator in well-routed beaming. Light-Sci Appl 4
52. Ni X, Emani NK, Kildishev AV, Boltasseva A, Shalaev VM (2012) Broadband light bending with plasmonic nanoantennas. Science 335:427–427

# Chapter 6
# Summary Outlook

Due to its unique property of extreme confinement of electromagnetic (EM) field on metal surface, there is a great potential application prospect for SPP to be used in photonics integration. Base on this property, this dissertation achieve some interesting progresses on the in-plane SPP modulation as well as the far field light modulation with plasmonic structure. The major results and conclusions are as follows.

1. We proposed and demonstrated an in-plane phase modulation method for propagating SPPs based on SPP diffraction. We extended the traditional diffraction principle of optics to 2 dimensional (2D) SPPs and studied the diffraction process of SPPs by non-periodic nanoarray. The diffraction principle of SPPs under non-perfectly-matched Bragg condition was discovered and experimentally proved, which can be used to modulate the phase of SPPs in 2D system.
2. With this phase modulation method, a plasmonic non-diffraction Airy beam was realized totally by in-plane diffraction processes. The revealed Airy beam exhibits the unique features, such as nondiffraction, self-bending and self-healing. In addition, a new group of collimated plasmon beams with controllable intensity distribution (e.g., "lossless" plasmon) were achieved with symmetric phase modulation. Furthermore, we extended this method to realize arbitrary non-monotonic beams. These revealed beams can be taken as non-confined waveguides, without suffering the loss from confining structures. This study gives a unique insight into the SPP beam formation and is expected to inspire more intriguing phenomena and potential applications in beam engineering and nanophotonic manipulations.
3. The broad band focusing of SPPs was realized by the phase modulation scheme as well and the bandwidth is about 100 nm in visible region. The design can be used as a SPP demultiplexer and the resolution is about 12 nm. We extended this phase tuning scheme to SPPs from point source and realized several kinds of beams as well, indicating the wide application of the phase modulation scheme.



L. Li, *Manipulation of Near Field Propagation and Far Field Radiation of Surface Plasmon Polariton*, Springer Theses,
DOI 10.1007/978-981-10-4663-6_6

4. The phase modulation scheme can also be applied to light modulation in 3D free space. A far field optical orbital angular momentum beam (OAM) was realized by plasmonic structures. The radical phase of the beam can also be integrally modulated together with the OAM beam generation, and we got nondiffraction, focusing or off-axis injecting OAM beams. The beam splitting process can be integrated with the generation as well and the according split beams can carry different OAM numbers, which would inspire further research and applications of OAM beam in information processing.
5. A scheme to reconfigure polarization states based on two orthogonal propagating SPPs were proposed. The light with the different polarization states will be scattered out of the metal surface by nanostructures and can be analyzed or manipulated by polarization systems. We experimentally verified this scheme and realized polarization controlled beams (such as directional beaming, airy beam, focusing, etc.) based on this scheme. Furthermore, by the multiplexing of the scatters, multiple desired polarization states in required beam-forms can be realized simultaneously. More importantly, the scheme provides a new dimension of polarization control, which can co-work with other polarization control systems (such as the coupling system, metasurface etc.). We have realized a $2 \times 2$ controlled beams, indicating its exciting ability to improve the information capacity.

In conclusion, this dissertation developed a serial of effective methods to modulate the phase and polarization of the SPP propagation, diffraction and radiation. Several modulation and demultiplexing of photonic information were successfully demonstrated with these methods, such as the steering of SPP beams, OAM beam generation, as well as the polarization reconfiguration. The modulation methods can not only be applied to plasmonic system, they can also be used to other wave systems. Besides the promotion of our understanding of SPPs, these modulation methods will also inspire the research and applications in other systems, such as microwave, acoustics, and so on.